IMPACT PERFORMANCE OF RECYCLED TIRE CHIP AND FIBER REINFORCED CEMENTITIOUS COMPOSITES FOR USE IN CONCRETE

by

VICTOR LOPEZ

(Under the Direction of Mi Geum Chorzepa)

ABSTRACT

The ultimate aim of this study was to maximize the energy dissipation capacity of rubberized fiber reinforced concrete (FRC) mixtures subjected to impact forces for the purpose of improving the impact resilience of GDOT safety barriers and other applications. The first part of this study involved small-scale testing of preliminary mixtures to optimize compressive strength, modulus of rupture, and impact resilience using a fixed percentage of tire chip replacement of the coarse aggregate and varying volume fractions of steel, polypropylene, and polyvinyl alcohol fibers. Rubberized FRC beams were then tested under static loads to maximize the static energy dissipation potential of steel fiber inclusion at varying tensile steel reinforcement ratios. The final part of this study involved performing scaled drop-weight impact tests and results confirmed that rubberized FRCs exhibit significantly improved energy dissipation capacity and impact resilience, particularly with 1.0% steel fiber addition and 20% tire chip replacement.

INDEX WORDS: Cementitious Composites, Fiber Reinforced Concrete (FRC), Rubberized Concrete, Energy Dissipation Capacity, Impact, Recycled Tire Chips, Steel Fibers, Polypropylene Fibers, Polyvinyl Alcohol Fiber

IMPACT PERFORMANCE OF RECYCLED TIRE CHIP AND FIBER REINFORCED

CEMENTITIOUS COMPOSITES FOR USE IN CONCRETE

by

VICTOR LOPEZ

B.S., The University of Georgia, 2017

A Thesis Submitted to the Graduate Faculty of The University of Georgia in Partial Fulfillment

of the Requirements for the Degree

MASTER OF SCIENCE

ATHENS, GEORGIA

2018

IMPACT PERFORMANCE OF RECYCLED TIRE CHIP AND FIBER REINFORCED CEMENTITIOUS COMPOSITES FOR USE IN CONCRETE

by

VICTOR LOPEZ

Major Professor: Mi G. Chorzepa

Committee: Stephan A. Durham

S. Sonny Kim

Electronic Version Approved:

Suzanne Barbour
Dean of the Graduate School
The University of Georgia
August 2018

DEDICATION

I dedicate this thesis to my parents, Virginia and Juan Lopez, and my brother Daniel Lopez. Without the sacrifices that my parents had to make when immigrating to this country, I would not be in the position I am today. My family has taught me the value of hard work and perseverance, which has been reflected in this thesis.

ACKNOWLEDGEMENTS

I would like to acknowledge all those that helped with the completion of this study. First and foremost I would like to thank Dr. Mi Geum Chorzepa for her unconditional support and belief in me. I would also like to thank my committee members Dr. Stephan Durham and Dr. S. Sonny Kim for their guidance and contributions throughout this process. Furthermore, on behalf of the University of Georgia, I would like to acknowledge the Georgia Department of Transportation for their financial support and involvement over the past year. A special thanks is extended to Tofail Ahmed, Grace Darling, Steven Tate, Davis Wing, Chris Johnson, Hiwa Hamid, Sean (Seungyeon) Seol, and Robert Chorzepa for their contributions to this project.

TABLE OF CONTENTS

LIST OF TABLES

LIST OF FIGURES

1. INTRODUCTION

1.1 Background

There has been an increasing demand for the use of cementitious composites that aid in the impact resilience of reinforced concrete structures. Standard concrete mixtures do not exhibit the necessary properties to effectively dissipate energy caused by intense dynamic loading. As a result, several recent studies have been conducted to observe the impact response of reinforced concrete structures (e.g., Masud 2015, Li. et al. 2005, Fujikake et al. 2009, Saatci et al. 2009). These studies have shown that standard concrete members are susceptible to localized failure responses when subjected to impact loads, resulting in target fracture and section loss instead of exhibiting significant deformation. Specifically, this issue has been observed several times in high-speed highway related accidents. Concrete safety barriers are installed along highway systems to prevent vehicles from traversing to the opposing lane of traffic and to reduce overall destruction. However, standard concrete safety barriers are often too stiff, causing vehicles to ricochet off the surface and back into traffic rather than absorbing the impact. The results include possible fatalities and severe destruction of vehicles and safety barriers. A way to mitigate this outcome is to develop engineered cementitious composites (ECC) that not only possess adequate compressive and flexural strength, but also exhibit substantial ductility and energy dissipation capacity.

Over the last few decades, research has been conducted that incorporates supplementary fiber reinforcement within concrete mixtures (e.g., Masud 2015, Noaman et al. 2017, Afroughsabet et al. 2015). Fibers such as steel, polypropylene (PP), and polyvinyl alcohol (PVA) have all been proven to improve ductility under static and dynamic loading (Masud, 2015). These fibers come in various geometries and, depending on the application, are used to bridge both macrocracks and microcracks.

Similarly, recycled rubber tire chip aggregates have also been observed to improve ductility and impact resilience (Stallings, 2017). Each year, an estimated 1 billion tires are decommissioned, with over 50% of these tires stockpiled into landfills (Thomas, et. al. 2015). This number is expected to rise to 1200 million tiles yearly by 2030. As a result, increasing work has been done to include recycled tire rubber aggregates in concrete related applications.

1.2 Study Objectives

This study ultimately aims to develop an optimized hybrid concrete mixture that incorporates fiber reinforcement and recycled tire rubber aggregates for use in concrete safety barriers and other applications. Although plenty research has been done on concrete members that study fiber and recycled rubber aggregates individually, little research has been conducted on the effects of combining these constituents in scaled concrete structures subjected to impact forces. This study is part of a two-phase study that extends the work conducted by Stallings (2017) in which preliminary mixtures were optimized to incorporate recycled tire chips to maximize the toughness (i.e. energy dissipation capacity) of standard concrete subjected to small-scaled impact forces. In Phase-I, various quantities and particle sizes of rubber aggregates were observed using various chemical and mechanical surface treatment methods to improve the bond between these rubber particles and the cement paste. The minimum performance level of the fresh and hardened concrete properties were to adhere to GDOT specifications.

The goal of this study is to use the optimized rubberized concrete mixture determined by Stallings (2017) and incorporate fiber reinforcement to improve upon the diminished mechanical strength properties of the rubberized concrete that result from rubber particle inclusion. Steel, polypropylene, and PVA fibers will be observed in conjunction with tire chips to design an optimized concrete mixture design. This optimized mixture design will ultimately be used to batch scaled concrete beams that will be subject to static and impact loads to maximize total energy dissipation capacity. The results from this study will ultimately be used to create a mixture design to test scaled GDOT safety barriers under impact loads in a laboratory setting.

2. LITERATURE REVIEW

2.1 Chapter Overview

This section serves to study the effects of rubber tire chips and fiber reinforcement for use in concrete applications. These studies serve to foster a better understanding of how these materials affect the mechanical properties of concrete as well as develop expectations for overall concrete performance. Topics emphasized include effects on fresh and hardened concrete properties, and energy dissipation potential.

2.2 Effects of Rubber in Concrete

2.2.1 Slump

Existing literature suggests that rubber tire chips tend to decrease slump, especially at higher aggregate replacement percentages. Holmes et al. (2014) and Su et al. (2014) observed not only a decrease in slump at higher rubber proportions, but also a decrease in slump due to reduction of particle size. On the contrary, Khatib and Bayomy (1999) determined that mixtures consisting of fine crumb rubber exhibited more workability than those consisting of coarse tire chips or a hybrid between tire chips and crumb rubber. In the same study, it was also found that slump decreased with increasing total rubber volume fraction, especially at 40% and greater at which point workability was very poor and slump measured zero. In mixtures where tire chips replaced coarse aggregates, slump increased with increasing volume fraction of tire chips up to 15%, but decreased beyond 15% (Pacheco-Trogal et al. 2012). Similar to the fine and coarse aggregates, tire chips have their own absorption capacity, which also cause rubberized concrete to exhibit lower slumps (Su et al. 2015). However, Raghvan et al. (1998) concluded that adding rubber shreds either maintained or slightly improved workability compared to the control in mortar mixtures.

2.2.2 Unit Weight

Standard normal weight concrete is widely considered to be about 150 lb/ft^3 (2400 kg/m^3). The inclusion of tire particles as a replacement of aggregate unsurprisingly reduces unit weight due to the lower density of rubber. In one study, it was observed that mixtures containing a 50% replacement by volume of coarse and fine aggregate experienced a decrease in unit weight of 5.8% and 6.0%, respectively. At 75%, unit weight decreased even further by 8.8% and 8.3%, respectively (Aiello, et al., 2010). Research done by Topcu (1995) reinforced these results when studying the unit weight properties of rubber inclusion in cement paste and mortar. A 12.6% reduction in unit weight was found in mixtures consisting of a 45% coarse and fine rubber aggregate replacement by volume. Similarly, Sukontasukkul and Tiamlom (2012) found that the unit weight of rubberized mixtures decreases with increasing quantity of crumb rubber replacement of fine aggregate as well as with decreasing rubber particle size. However, Pacheco-Trogal et al. (2012) observed a reduction in unit weight of 45% with coarse aggregate replacement and only a 34% reduction with fine aggregate replacement. The combination of replacing both coarse and fine aggregates produced a reduction of 33%. At replacement levels lower than 10-20% volume fraction of rubber, it was determined that unit weight loss was negligible (Khatib and Bayomy, 1999). Pelisser et al. (2011) also found that the density of concrete with recycled rubber inclusion decreased by 13% when compared to the control. However, when silica fume was added to this same rubberized mixture, only a 9% reduction in unit weight was observed due to the densification of the concrete matrix as a result of the small particle size of the silica fume. In another study, it was found that rubberized pervious concrete possessed densities 2-11% lesser than the control mixture (Gesoglu et al., 2014).

2.2.3 Air Content

Air content in concrete is linked to other concrete properties such as durability, unit weight, and compressive strength. Therefore it is crucial to understand how tire chip inclusion impacts air content. Fedroff et al. (1996) found that the air content in rubberized mixtures was greater compared to the control, even without the presence of an air-entraining admixture. Khatib and Bayomy (1999) also experienced an increase in air content with rubberized mixtures. In this same study, it was found that air content was even greater in mixtures containing crumb rubber compared to mixtures with tire chips at the same replacement level. It is believed that this increase in air content may be a result of the non-polar nature of rubber particles. Because rubber in concrete has the tendency to repel water, air may consequently become trapped on the rough surface of the rubber particles (Siddique et al., 2004).

2.2.4 Temperature

Concrete placement temperature is vital to the cement hydration process. Ideally, it is recommended to place concrete at temperatures between 50° and 60 °F (10-16 °C), but should typically not exceed 85 °F (29 °C) (Kardos and Durham, 2015). Temperatures exceeding the recommended range will lead to a rapid acceleration in cement hydration, resulting in an increased rate of water evaporation from the concrete. This consequentially leads to the development of internal stresses and cracking from plastic shrinkage.

Factors such as humidity and wind velocity also have an effect on safe concrete batching practices. Figure 2-1 is a chart provided by ACI 308 that takes into account all these factors. Issues with hot weather concrete are early cracking, especially on the surface exposed to direct sunlight, rapid evaporation of water, and accelerated cement hydration process.

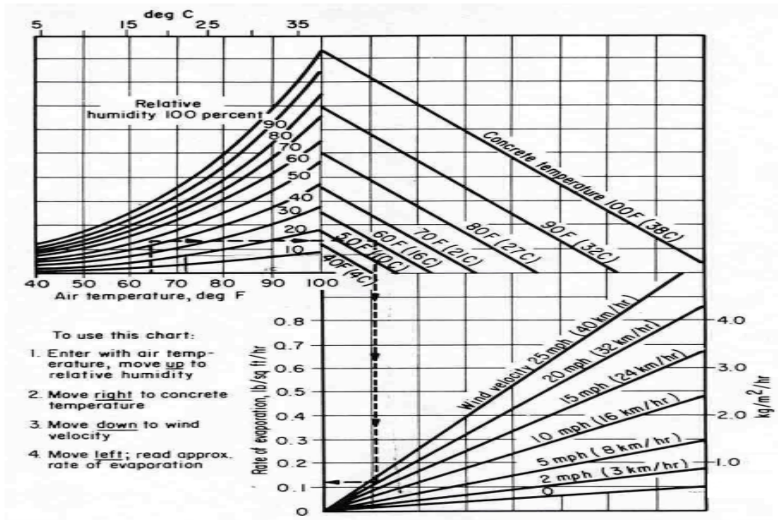

Figure 2-1. ACI 308 – Nomograph Used to Estimate Maximum Potential Evaporation Rate of the Environment (Menzel 1954; NRMCA 1960).

2.2.5 Compressive Strength

Several studies have proven that concrete compressive strength decreases with rubber inclusion. In one study, a group rubberized mixtures with a 25%, 50%, and 75% coarse aggregate replacement were compared to another group with a 15%, 30%, 50%, and 75% fine aggregate replacement. It was found that the mixtures with coarse aggregate replacement exhibited a compressive strength decay of 47.8%, 54.4%, and 61.9%, respectively, compared to the control. Less significantly, mixtures with fine aggregate replacement experienced a compressive strength decay of 11.6%, 24.7%, 28.3% and 37.1%, respectively, compared to the control. These results are shown in Figure 2-1. It was ultimately deemed that the replacement of coarse aggregate with rubber reduced compressive strength more than the replacement of fine aggregate (Aiello et al., 2010).

No.	Compressive strength[a] (MPa)	COV (%)	St. dev. (MPa)	Decrease (%)
C1	45.80	5.20	±2.38	–
RA1	23.90	12.29	±2.93	47.8
RB1	20.87	12.79	±2.67	54.4
RC1	17.42	12.89	±2.25	61.9

No.	Compressive strength[a] (MPa)	COV (%)	St. dev. (MPa)	Decrease (%)
C2	27.11	5.78	±1.57	–
RA2	23.97	1.90	±0.46	11.6
RB2	20.41	1.97	±0.40	24.7
RC2	19.45	6.48	±1.26	28.3
RD2	17.06	3.93	±0.67	37.1

Figure 2-2. Effect of Increasing Rubber Content Replacement of Coarse (Top) and Fine (Bottom) Aggregate on Compressive Strength (Aiello et al., 2010).

In support of these findings, Eldin and Senouci (1993) found an 85% decay in compressive strength and a 50% decay in splitting tensile strength when coarse aggregates were entirely replaced by tire chips. A 65% decay in compressive strength and a 50% decay in splitting tensile strength was found when fine aggregates were entirely replaced by crumb rubber. Khatib and Bayomy (1999) and Topcu (1995) also found a greater negative impact on compressive strength when replacing coarse aggregates with tire chips compared to replacing fine aggregates with crumb rubber. However, Ali et al. (1993) and Futtuhi and Clark (1996) experienced the opposite.

Ganjian et al. (2009) describes various reasons for this decrease in compressive strength with rubber inclusion. Due to the significantly smoother surface of the rubber particles relative to natural aggregates, the cement paste surrounding these rubber particles would be softer than with non-rubber particles. This softer paste is much more susceptible to rapid crack development under compressive and tensile stresses. Also as a result of the smoother surface of the rubber particles, the bond between the rubber and cement is weaker. Without adequate friction between the rubber particles and the cement paste relative to the natural aggregates, an uneven distribution of stresses would be experienced throughout the concrete matrix. Furthermore, compressive strength is dependent on the individual physical and mechanical properties of each constituent used in the concrete mixture. Replacing any of these constituents with rubber, specifically the aggregates, will ultimately lead to a decrease in compressive strength. Finally, a less uniform mixture is often experienced with rubber inclusion. This occurs due to the relatively lower specific gravity of rubber compared to the other constituents, causing the rubber to rise to the surface when vibrating. This inadvertently leads to an uneven distribution of stresses between the top and bottom surfaces of the concrete matrix.

2.2.5.1 Surface Treatments

The bond between rubber particles and the cement paste in concrete is heavily linked to compressive strength. Naik and Singh (1991) have found that using surface treatments, either chemical or mechanical, to roughen the surface of the rubber particles may improve bonding within the concrete matrix, leading to increased compressive strength. These surface treatments include washing rubber particles with water to remove contaminates and using acid, plasma pretreatments, and using various coupling agents to create microscopic etchings on the surface. A common form of acid treatment is submerging the rubber particles in a sodium hydroxide (NaOH) solution for a set period of time, and then rinsing them with water. In one study, his method proved to be very effective when tire chips were submerged and continuously stirred in NaOH for 20 minutes before mixing in concrete. After using a Scanning Electron Microscope (SEM), the interfacial surface between the rubber particles and cement paste was found to have improved adhesion when NaOH was used. This resulted in improved bonding between the tire chips and cement paste, which caused compressive strength, flexural strength, and fracture energy to improve when tire chips were included as an addition rather than replacement of aggregates by volume (Segre and Joekes, 2000).

Rostami et al. (1993) compared various methods of pretreatments that included using water, water and carbon tetrachloride solvent, and water and a latex admixture cleaner. By using these methods, a 16% increase in compressive strength was found in concrete containing prewashed rubber aggregates and a 57% increase when rubber aggregates were treated with carbon tetrachloride (Siddique et al. 2004).

In another study, Stallings and Durham (2017) compared the effectiveness between mechanical surface roughening, NaOH, and silane coupling agent to treat the surface of the rubber particles. To induce mechanical abrasion on the rubber surface, recycled tire chips were mixed with the coarse and fine aggregates for ten minutes prior to the inclusion of other constituents. The friction between the natural aggregates and tire chips led to a roughened rubber surface, increasing the surface area for the rubber to bond to the cement paste. For NaOH surface treatment, the tire chips were submerged in a bath of NaOH for 20 minutes and then rinsed with water before being dried to room temperature. Tire chips in silane coupling agent were treated in the same manner; however, they were oven dried in a standard laboratory oven post-treatment. Stallings and Durham (2017) used these treatments on mixtures containing 10% and 20% tire chip replacement of the coarse aggregate and found that NaOH treatments produced a 17% and 16% increase in compressive strength, respectively, and an 11% and -13% increase, respectively, with silane coupling agent compared to mechanical roughening surface treatment.

2.2.6 Flexural Strength

Similar to compressive strength, flexural strength has also been found to decrease with the inclusion of rubber. At a 50% and 75% replacement of coarse aggregate, rubberized mixtures experienced reduced flexural strength of about 28% compared to the control. At these same replacement levels of fine aggregate, flexural strength reduction was 5.8% and 7.3%, respectively, compared to the control. Although a reduction in flexural strength was observed, the post-cracking behavior of the rubberized mixtures consisting of coarse aggregate replacement showed increased residual strength after cracking. However, this observation was not as prevalent with fine aggregate replacement (Aiello et al. 2010). These finding are supported by Toutanji (1996) where an 18.5% and 26% reduction flexural strength was experienced in mixtures consisting of a 50% and 75% rubber replacement of the total natural aggregates. For these same mixtures, Toutanji (1996) also observed an increase in post-cracking residual strength. In another study, Ganjian et al. (2009) found a 37% reduction in flexural strength when replacing coarse aggregates with tire chips and a 29% reduction when cement was replaced with powdered rubber. This decrease in flexural strength was more attributed to the lack of good bonding between the rubber and cement paste than with reduction of tensile strength. Concrete already possesses very low tensile strength relative to its compressive strength and thus, further reduction in tensile strength from rubber inclusion will have little effect on flexural strength capacity. Evidence of poor bonding was seen in this study post-flexural testing when it was observed that the tire chips could easily be separated from the concrete. This was more prevalent with tire chip than with powdered rubber.

Kardos and Durham (2015) observed that in rubberized mixtures containing crumb rubber, an increase in residual strength was found with rubber inclusion when compared to the control in modulus of rupture (MOR) testing. At ultimate load, the control specimen failed suddenly and without warning, whereas the rubberized mixture sustained approximately one-quarter of the ultimate load for a prolonged period of time.

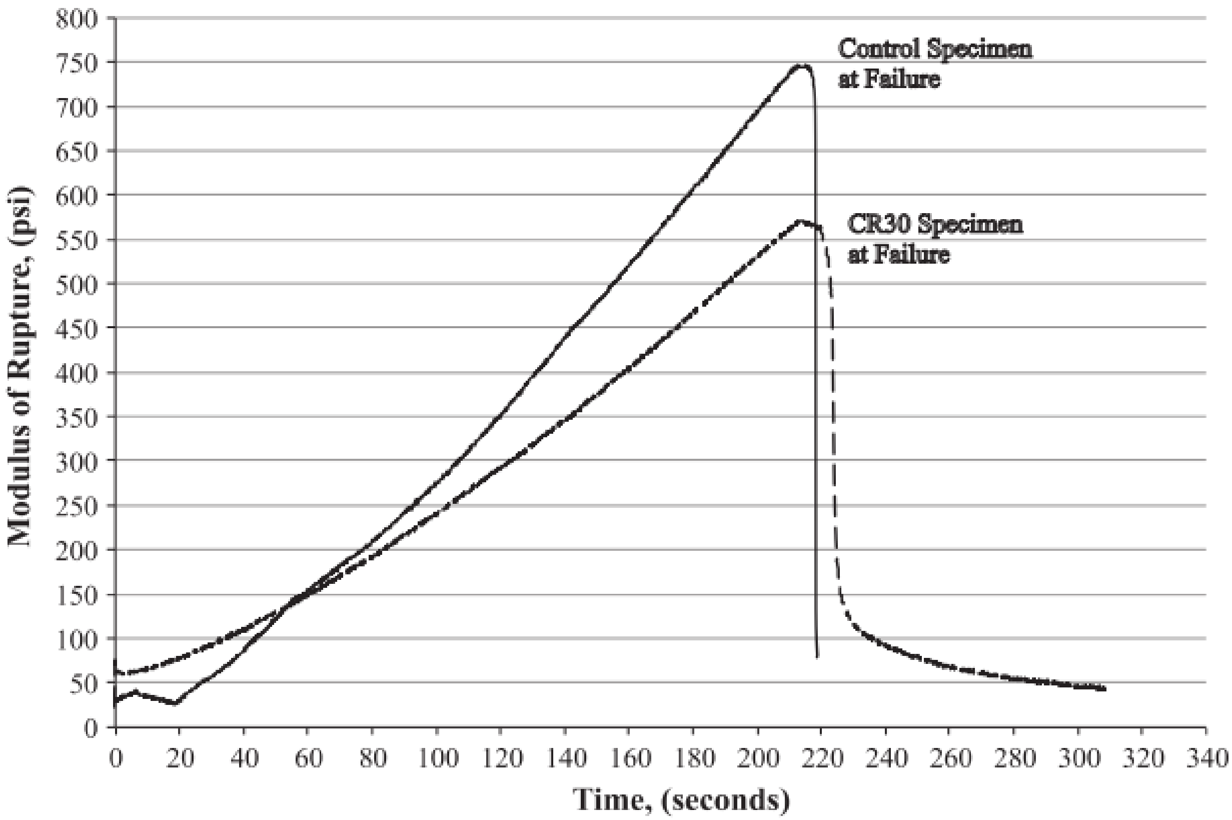

Figure 2-3. Comparison of Modulus of Rupture Behavior Post-Failure between Control Mixture and 30% Crumb Rubber (Kardos et al., 2015).

2.2.7 Energy Dissipation

Due to the nature and properties of rubber, the inclusion of rubber particles in concrete has been studied for potential improvements in energy dissipation capacity. The use of rubber in concrete beams demonstrated improved ductility by increasing energy absorption capacity of standard concrete (Ismail et al., 2016). However, by reducing total stiffness, rubber tire chips and crumb rubber have an adverse effect on mechanical properties. Goulias and Ali (1997) observed a decrease in dynamic modulus of elasticity and rigidity with increasing rubber contents. Essentially, at higher rubber contents, concrete becomes less stiff and more ductile. In another study, Tantala et al. (1996) noticed in increase in toughness, or the area under the load-deflection curve, in rubberized mixtures consisting of 5% and 10% buff rubber (2-6mm) content. However, the 10% rubber mixture possessed less toughness than the 5% due to lower compressive strength (Siddique et al., 2004)

Raghvan et al. (1998) investigated mortar mixtures consisting of rubber shreds consisting of rubber shreds (5.5 mm x 1.2 mm and 10.8 mm x 1.8mm) and granular (2 mm in diameter) and found that these specimens were able to carry residual load after the peak load. Larger particle sizes of rubber caused specimens to remain in one piece, whereas smaller sizes of rubber caused the specimen to split into two pieces. Similarly, Biel and Lee (1993) investigated rubberized mixtures with 30%, 45%, and 60% rubber volume fractions of the fine aggregate and saw gradual diagonal shear failure development, as opposed to the control, which fractured into several components. Khatib and Bayomy (1999) also found that at a 60% rubber volume fraction of the total aggregate, specimens demonstrated permanent elastic deformations. A more ductile failure response of rubberized concrete was also experienced by Edin and Senouci (1993).

In one study, it was observed that the fracture energy of concrete was improved by 35% at a 15% replacement ratio of fine aggregate by crumb rubber. After this 15% replacement ratio, fracture energy slightly decreased, because although the maximum displacement increased, the maximum load capacity decreased (Gesoglu et al. 2014). Taha et al. (2008) recommended limiting the content of crumb rubber aggregates by up to 10% volume of the fine and coarse aggregate to optimize fracture energy and decrease the reduction in flexural strength. In another study, Guo et al. (2014), determined that the optimum crumb rubber content was between 4-8% by volume. Up to this optimum range, both fracture energy and toughness was shown to increase. However, for these properties Noaman et al. (2017) and Benzzouk et al. (2003) found the optimum replacement ratio of fine aggregate with crumb rubber to be 20%. Inversely, Aiello et al. (2010) found that post-cracking behavior was unaffected by fine aggregate replacement. It was noticed that coarse aggregate replacement produced greater residual strength after cracking and a significant increase in energy absorption capacity.

2.2.8 Applications

The use of recycled tires as a construction material extends to various applications. Earlier studies have shown the effectiveness of incorporating recycled tires in asphalt. Siddique et al. (2004) summarized that rubberized asphalt produced increased skid resistance, reduced fatigue cracking, and a prolonged pavement life when compared to conventional asphalt (Kholsa et al. 1990; Ragvan et al. 1998;, Khatib and Bayomy, 1999; Fedroff et al. 1996). Furthermore, Fattuhi et al. (1996) suggested that rubberized concrete can be utilized in areas where vibration damping is required (i.e. railway stations), trench filling and pipe bedding, pile heads, and paving slabs, and resistance to impact is necessary (i.e. safety barriers, railway buffers, and bunkers). It was also suggested that rubberized concrete can be used in highway applications not solely related to impact. Topcu and Avcular (1997) hypothesized that rubberized concrete can be used as shock absorbers in sound barriers to dampen highway related noise, and in buildings to absorb seismic wave activity, though little research has been done to study these applications.

2.3 Effects of Fiber Reinforcement in Concrete

2.3.1 Steel Fibers

Afroughsabet et al. (2015) studied the effects of steel fiber inclusion in plain concrete at volume fractions of 0.25%, 0.5%, 0.75%, and 1.0%. It was found that mechanical properties such as compressive strength, splitting tensile strength, and flexural strength all improved as a result of increasing steel fiber volume fraction. At 28-days, it was observed that a 1.0% volume fraction improved these mechanical properties by 19%, 55%, and 61%, respectively, relative to the control.

Sahin, et al. (2011) conducted research on the influence of steel fiber tensile strengths on fracture energy of high-strength concrete. It was found that varying steel fiber volume fraction and steel fiber tensile strength had an insignificant effect compressive strength. It was noted that steel fiber inclusion has more of an effect on the ductility of compressive failure rather than compressive strength itself. Increasing steel fiber volume fraction and increasing steel tensile strength did nonetheless, have a considerable impact on splitting tensile strength and flexural strength. For steel fibers with a tensile strength of 1050 MPa and a steel volume fraction of 1.0%, an increase in flexural strength relative to plain concrete of 255%, 218%, and 218% was reported at water/cement ratios of 0.55, 0.45, and 0.35, respectively. Increasing the tensile strength of the fibers to 2000 MPa, an increase of 355%, 324%, and 293% in flexural strength was determined at w/cement ratios of 0.55, 0.45, and 0.35, respectively. From the flexural tests conducted, load-deflection plots were created to visually compare the effect of these parameters. For mixtures with a water/cement ratio of 0.35, these load-deflection plots are seen in Figure 2-4.

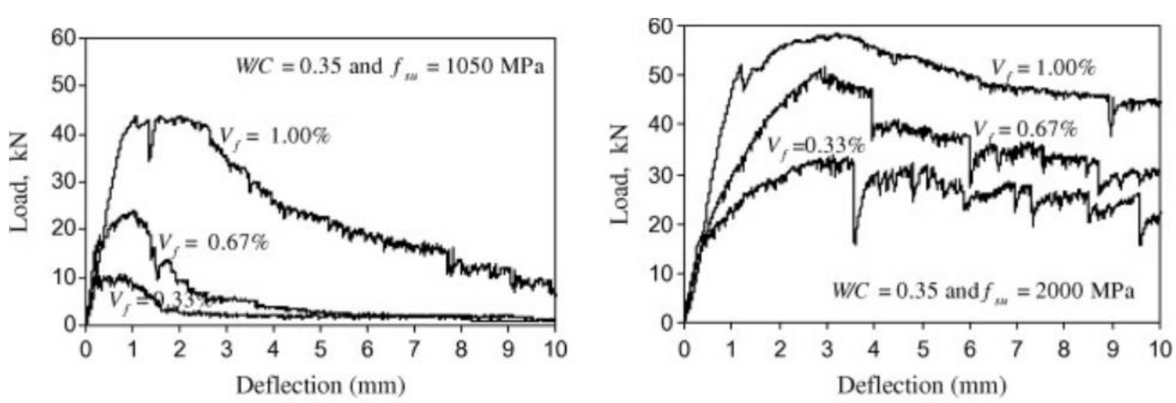

(a) f_{su} = 1050 MPa (b) f_{su} = 2000 MPa

Figure 2-4. Load-Deflection Plots Comparing Effects of Steel Fiber Volume Fraction and Steel Fiber Tensile Strength (Sahin et al. 2011).

Furthermore, the inclusion of hooked-end steel fibers with an aspect ratio of 80 increased fracture energy by 2.2 and 3.6 times than the control at volume fractions of 0.33% and 0.67%, respectively (Sahin et al., 2011). These findings were supported by another study that found an increase in fracture energy by nearly a magnitude of 3 when steel fibers were added from 0.5% to 1.0% volume fraction (Mo et al., 2014). In another study, Noaman et al. (2017) reported an increase in fracture energy of 152% with the addition of 0.5% volume fraction of hooked-end steel fibers in plain concrete.

2.3.2 Polypropylene Fibers

Polypropylene fibers are often used in concrete because of their proven effectiveness in increasing toughness, enhanced shrinkage cracking resistance, and lower cost compared to steel fibers (Alhozaimy et al. 1995 and Banthia et al. 2006). In a study conducted by Afroughsabet et al. (2015), the mechanical properties of concrete containing polypropylene fibers (12mm in length) were compared to plain concrete at fiber volume fractions of 0.15%,0.30%, 0.45%. Mechanical properties such as compressive strength, splitting tensile strength, and flexural strength improved with increasing fiber volume fraction. At 0.45% fiber volume of polypropylene, these mechanical properties improved relative to the control by 13%, 20%, and 13%, respectively.

Although not as effective as steel fibers, polypropylene fibers are also used because of their relatively low melting point. With concrete exposed to extreme heat, it could be more desirable to incorporate fibers that will disintegrate and form channels to relieve pressure buildup and releases gases such as water vapor and CO_2 (Treacy, et al. 1996).

2.3.3 Steel-Polypropylene Fibers

Afroughsabet et al. (2015) found that steel fibers alone were much more effective at increasing compressive and flexural strength than polypropylene fibers. This is due to the higher strength and elastic modulus of steel fibers compared to polypropylene fibers, which allows steel fibers to bridge macrocracks more effectively. In this same study, Afroughsabet et al. (2015) proportioned polypropylene fibers at volume fractions of 0.15%, 0.30%, and 0.45% with steel fiber volume fractions of 0.85%, 0.70%, and 0.55%, respectively, equaling a total of 1.0% volume fraction. From these hybrid fiber-reinforced mixtures, it was observed that the inclusion of polypropylene fibers reduced compressive strength, splitting tensile strength, and flexural strength with increasing volumes of polypropylene. Compared to the control, the best performing hybrid fiber-reinforced mixture produced an increase of 18%, 51%, and 54% in compressive strength, splitting tensile strength, and flexural strength, respectively. These increases in mechanical properties are comparable, but still less than solely using steel fibers. The effects of varying volume fractions of steel and polypropylene on flexural strength can be seen in Figure 2-5.

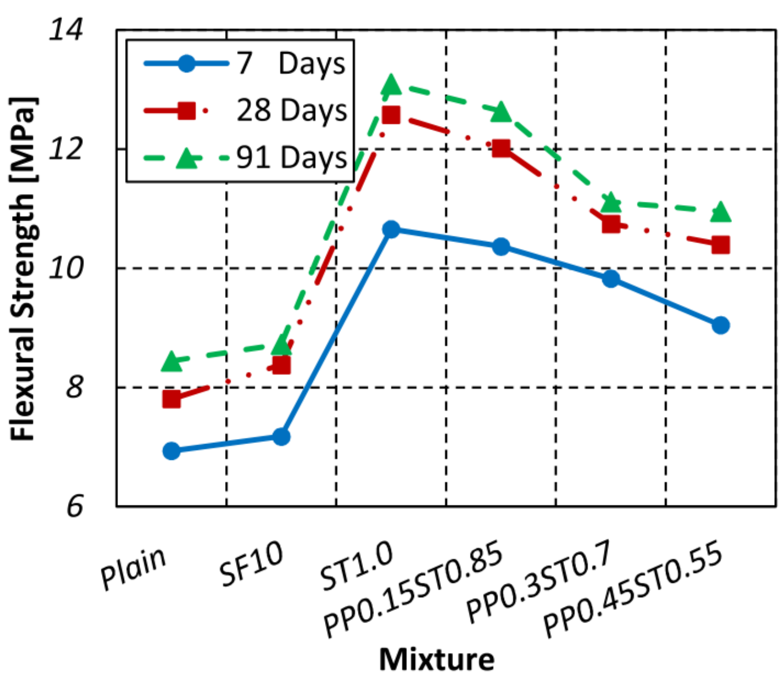

Figure 2-5. Flexural Strengths of Fiber-Reinforced Mixtures Containing Steel and Polypropylene Fibers (Afroughsabet et al., 2015).

In Figure 2-5, the hybrid-mixtures of steel and polypropylene fibers are compared to steel at 1.0% volume fraction (ST1.0), a mixture with 10% silica fume (SF10), and plain concrete.

2.3.4 Polyvinyl Alcohol Fibers

Yang et al. (2012) conducted a study that involved using engineering cementitious composites (ECC) for the purpose of impact forces. In this study, three mixtures (A, B, and C) were tested under small scaled impact tests at water/cement ratios of 0.26. Mixture A, the control, consisted of a 2% volume fraction of polyvinyl alcohol (PVA) fibers and fly ash. Similarly, mixture B also contained a 2% volume fraction of PVA fibers, but twice the quantity of fly ash. Finally, mixture B replaced the hydrophilic PVA fiber with a hydrophobic high modulus polyethylene (PE) spectra fiber, eliminating the interfacial chemical bond, and also contained fly ash (Yang at al., 2012). It was reported that mixture B experienced on microscopic cracking on the distal side after a 12 kg weight was dropped from a height of 0.5 m on the ECC square shaped panel. For comparison, a specimen with 0.5% steel reinforcement of similar size was tested and experienced brittle failure around the point of contact. Furthermore, beam specimens measuring 305 mm length x 76 mm height x 51 mm depth were tested by dropping a 50 kg impact ram from the same height. In these tests, standard concrete and ECC beams were compared under unreinforced and reinforced conditions. It was found that the ECC beams exhibited significantly improved performance in terms of load capacity and displacement. These load-displacement results can be seen in Figure 2-6.

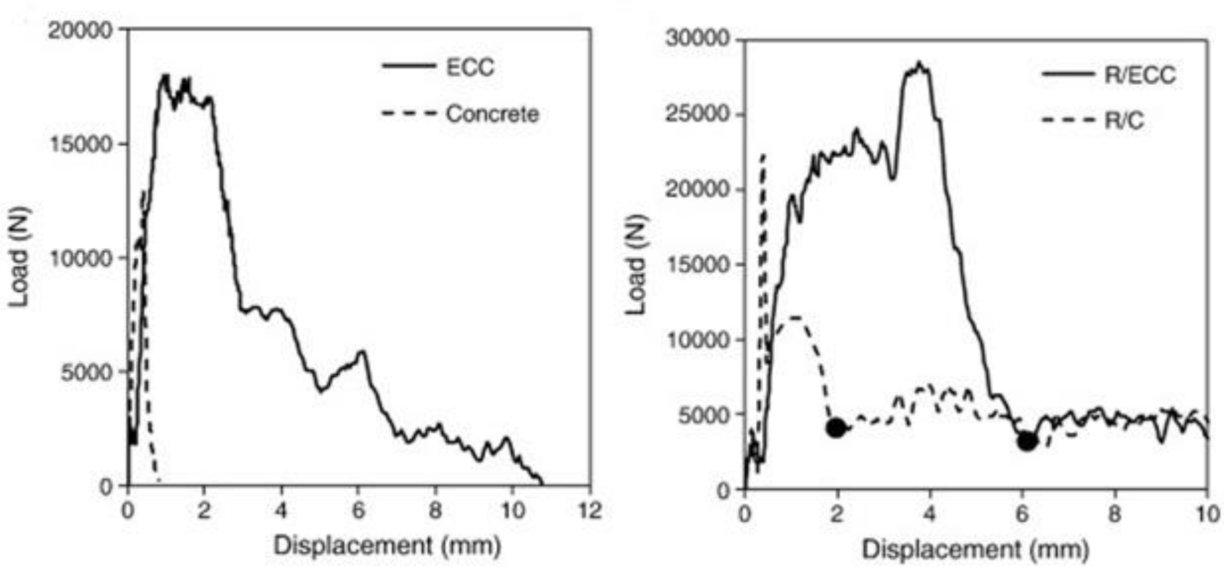

Figure 2-6. Load-Displacement Results Comparing Unreinforced (Left) and Reinforced (Right) Concrete and ECC beams (Yang et al., 2012).

It has also been shown that at 2.5% fiber volume fractions, PVA and PE fibers exhibit lower flexural strengths, but higher deflection capacity than steel fibers (Ahmed et al., 2007). This was due to the steel possessing a higher modulus of elasticity and greater stiffness than the PVA and PE fibers, resulting in greater flexural strength but less deflection. Ahmed at al. (2007) also showed that the combination of steel and PVA produced greater flexural capacity, but lower deflection compared to the combination of steel and PVA at the same volume fractions.

2.4 Rubberized FRC Beams

Relative to the amount of research that has been conducted on the effects of including recycled tire aggregates and fiber reinforcement in concrete independently, little research has been done to observe the hybrid effects of rubberized fiber reinforced concrete (FRC). It has been shown that tire chips from shredded tires with steel wires appear to show even better ductility in normal concrete than those without steel wires. (Zheng et al. 2008). In this same study, the damping ratio, or the measure of a material’s ability to reduce vibrations, of the concrete significantly improved with tire chip with steel wire inclusion when a volume fraction of coarse aggregate is replaced with tire chips, up to 30%. Essentially, the damping properties of rubberized concrete was more sensitive to vibration response amplitude than conventional concrete (Zheng et al. 2008).

In another study, Noaman et al. (2017) studied the fracture characteristics of plain and rubberized steel fiber reinforced concrete. It was found that the compressive strengths of plain concrete (PC) and steel fiber reinforced concrete (SFC) decreased with the inclusion crumb rubber at 5%, 10%, 10%, 15%, 20%, and 25% volume fractions at very similar rates, however compressive strengths for the SFC mixtures with crumb rubber inclusion (SFRRC) were on average higher than plain concrete with crumb rubber inclusion (PRC). A similar trend was experienced when comparing tensile and flexural strength decay between the SFC and PC mixtures with crumb rubber inclusion. It was also found that the stress intensity factor decreased with crumb rubber inclusion for both the PC and SFC mixtures. Furthermore, it was observed that fracture energy, or the energy required to induce a crack on a unit area of a material, increased with increasing crumb rubber content, up to a 20% crumb rubber replacement of fine aggregate. At 20% crumb rubber volume fraction, fracture energy increased by 42% compared to PC. More significant was the increase in fracture energy of 152% with the addition of 0.5% by volume of hooked-end steel fibers compared to PC. Crumb rubber combined with steel fibers showed an increase in fracture energy of PC from 190% to 246% when rubber content was changed from 5% to 20% (Noaman et al. 2017). Finally, the load-displacement plots in Figure 2-7 show an increase in residual strength with increasing volume fraction of crumb rubber inclusion in PC, although load capacity decreases as a result. Similar effects were observed with crumb rubber inclusion in SFC, however the increase in residual strength was significantly more prominent as a result of steel fiber inclusion (Noaman et al. 2017). Steel fibers also increased the total load capacity and initial linear stiffness in rubberized mixtures at all replacement levels.

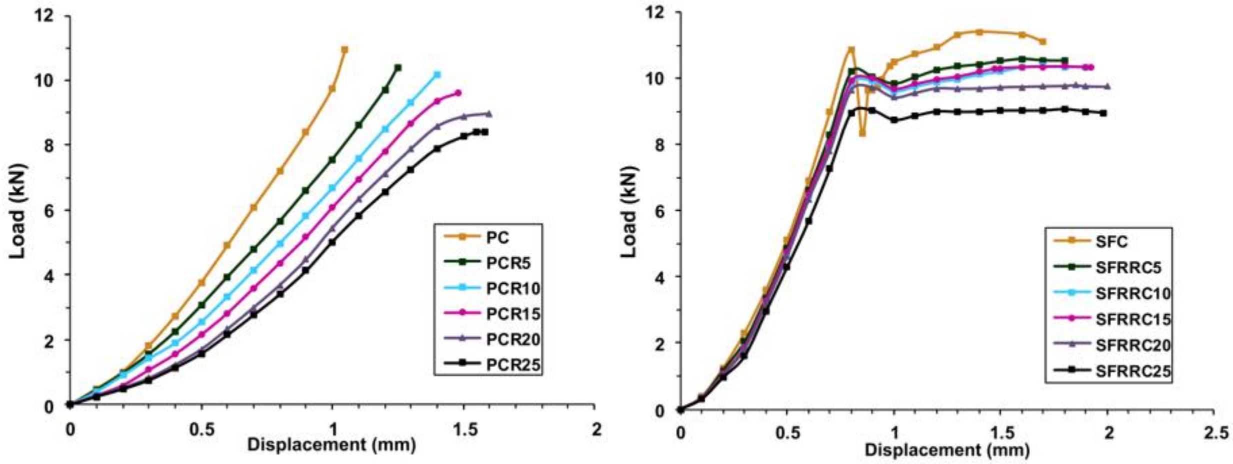

Figure 2-7. Load-Displacement Results Comparing Effect of Crumb Rubber (Left) and Steel Fiber (Right) (Noaman et al. 2017).

Based on the findings from Noaman et al. (2017), it was concluded that adding steel fibers to rubberized concrete significantly improves fracture energy and residual strength, while at the same time balancing the reduction of mechanical strength properties caused by rubber aggregate inclusion.

2.5 Impact Response of RC Beams

Fujikake et al. (2009) determined that reinforced concrete (RC) members typically experienced either localized or overall failure when subjected to impact forces, which can be seen in Figure 2-8. A local failure response is the result of the stress wave produced by the point of impact acting over a short period of time after impact. Conversely, an overall failure response is caused by the elastic-plastic deformation of a structural member over a long period of time after impact (Fujikake et al., 2009).

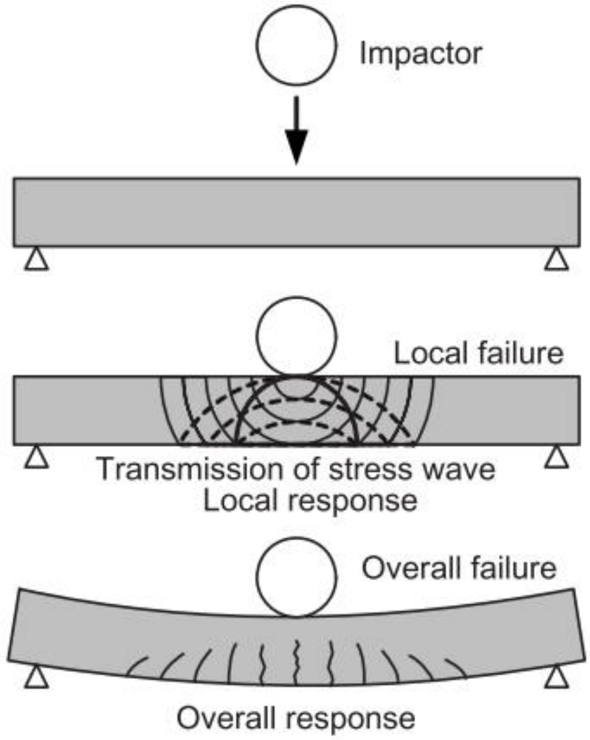

Figure 2-8. Impact Failure Response of RC Member (Fujikake et al., 2009).

Based on the results by Fujikake et al. (2009), conclusions were made regarding longitudinal steel and drop-weight. It was observed that RC beams with lower tension steel reinforcement ratios experienced only an overall flexural failure, whereas RC beams with higher tension steel reinforcement ratios experienced a combination of overall flexural failure and localized failure at the contact surface. Furthermore, increasing the reinforcement ratio of the compression steel led to increased resistance to localized failure responses of the RC beam. It was also noted that increasing the drop height of the weight resulted in increased maximum impact load, impulse, maximum mid-span deflection, duration of impact load, and time taken to reach maximum mid-span deflection (Fujikake et al., 2009). Increasing the drop height essentially increases the potential energy of the drop-weight, which in turn increases the kinetic energy produced at the point of impact.

Localized and overall failure responses to impact forces are summarized in greater detail by Li et al. (2005). Six missile impact effects, five of which are defined as local impact effects, are represented in Figure 2-9. The five local impact effects include penetration, cone cracking, spalling, scabbing, and perforation. Penetration is when a projectile imbeds itself into a target up to a certain length, which is known as the penetration depth. Cone cracking is defined as the development of cracks in a cone-like shape, possibly indicating punching shear failure. Spalling is the ejection of target material from the contact surface point of impact. Similarly, scabbing is the ejection of target material but from the distal surface. Perforation is the total passage of the projectile through the projectile (Li et al., 2005). As for the overall impact response, Li et al. (2005) defines it as the global bending, shear, and membrane responses as well as their induced failures throughout the target.

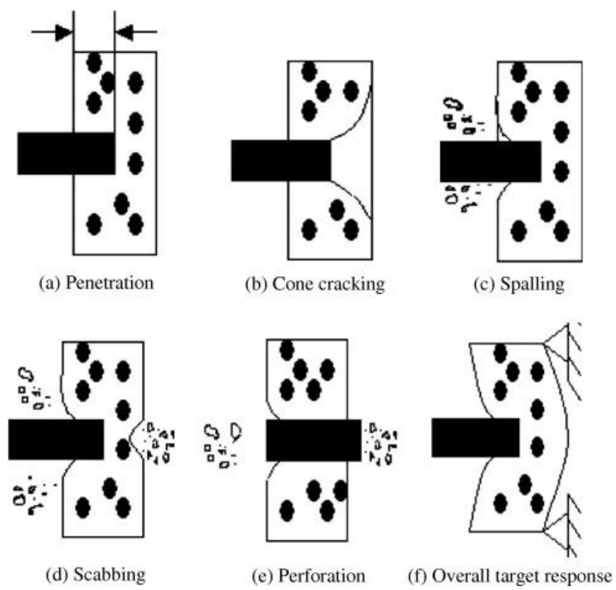

Figure 2-9. Missile Impact Effects on a Concrete Target (Li et al., 2005).

In another study, Saatci et al. (2009) reported that shear mechanisms must be considered to accurately predict the response of RC under impact loads. In this particular study, eight RC beams were tested under static and impact tests. For impact testing, two separate drop-weights weighing 465 lbs (211 kg) and 1323 (600 kg) were dropped from a height of 10.7 ft (3.26 m), resulting in a calculated impact velocity of 26.25 ft/s (8.0 m/s). For all specimens, significant diagonal cracking propagation was observed, regardless of shear reinforcement capacity. This resulted in the forming of a shear-plug under the point of impact. Furthermore, Saatci et al. (2009) found that the mass and geometric properties of a beam, and not just the cross-sectional properties, were key factors in initial impact response. Essentially, the impact forces at the initial stages were resisted by the inertia of each beam, before the forces reached the supports (Saatci et al., 2009). Similar diagonal shear failure cracks on RC beams subjected to impact loads were also reported by Chorzepa et al. (2015), Kishi et al.(2003), and May et al. (2005).

2.6 Predictive Equations for Impact Force and Displacement

Analytical models have been created to replicate and predict impact forces and deflections. Specifically, Tang et al. (2005) adopted a spring-mass model proposed by Abrate (1998) to model the behavior of fiber-reinforced polymer (FRP) concrete beams subjected to impact loads. This spring-mass model is used to predict impact forces and deflections for the purpose of this study.

2.6.1 Calculating Predicted Impact Force

Tang et al. (2005) developed this spring-mass model primarily to observe the impact behavior of a beam subjected to a drop-weight. This model represents two degrees of freedom. From force equilibrium of the free-body diagram, the equations of motion can be developed

$$m_1 \frac{d^2 y_1}{dt^2} + F = 0 \quad (\mathbf{1})$$

$$m_2 \frac{d^2 y_2}{dt^2} + K_{bs} y_2 + K_m y_2^3 - F = 0 \quad (2)$$

Where m_1 and m_2 are the masses of the drop-weight (impactor) and beam, respectively; y_1 and y_2 are the displacements of the drop-weight and the beam; F is the impact force of the drop-weight and the beam; and K_m is the membrane stiffness. The initial conditions are expressed at $t = 0$ (just before contact occurs)

$$\frac{dy_1}{dt}(0) = V; y_1(0) = y_2(0) = 0 \tag{3}$$

Where V is the initial velocity of the drop-weight the instant prior to impact. Assuming that the geometrical nonlinearity and the indentation are negligible, Tang et al. (2005) simplified the model to a single degree of freedom system with the equation of motion as

$$m_1 \frac{d^2y}{dt^2} + K_{bs}y = 0 \tag{4}$$

To simplify the equation even further, the effective mass of the structure is neglected. It is assumed that the drop-weight and structure move as one immediately after initial impact, meaning that $y_1 = y_2 = y$. Using the initial conditions at $t = 0$, the general solution of Eq. (4) is expressed as

$$y = \frac{V}{\omega} sin\omega t \tag{5}$$

Where $\omega^2 = K_{bs}/m_1$. Furthermore, because the impact force F is equal to the force in the linear spring K_{bs}, the impact force history can be expressed as

$$F = K_{bs}y = V(K_{bs}m_1)^{\frac{1}{2}} sin\omega t \tag{6}$$

Eq. (6) is derived based on the assumption that the beam stiffness remains constant during the impact (Tang et al., 2005). Realistically, the stiffness of a concrete beam decreases as the beam cracks. Eq. (6) is modified with a constant γ to incorporate the effects of reduced stiffness based on the test results. Eq. (6) is then expressed as

$$F = K_{bs}y = \frac{V(K_{bs}m_1)^{\frac{1}{2}}}{\gamma} sin\omega t \tag{7}$$

Where γ is determined from the test results. In this study, γ was calculated as the average ratio of the measured first impact force for the test beams and the impact force calculated from Eq. (6).

2.6.2 Calculating Predicted Deflection

Tang et al. (2005) also derived an equation to calculate the predicted displacement under impact loading. Using a flexural wave theory developed by Graff (1975), the governing equation of motion is expressed as

$$\frac{\partial^4 y}{\partial x^4} + \frac{1}{a^2}\frac{\partial^2 y}{\partial t^2} = \frac{1}{EI} q(x,t) \tag{8}$$

Where y is the displacement of the beam; x is the coordinate along the beam axis from the support; EI is the stiffness of the beam; a is equal to $EI/A\rho$ where A is the beam cross section and ρ is the density of the beam; and finally $q(x,t)$ is the impact force, which can be expressed as

$$q(x,t) = P\delta(x - x_o)\delta(t) \tag{9}$$

Where P is the magnitude of the impact force; x_o is the distance from the support to the load point; and $\delta(t)$ is a function relating impact force and time. The solution to Eq. (8) is represented as

$$y(x,t) = \frac{2P}{\rho Al}\sum_{n=1}^{\infty}\frac{sin\beta_n x_o sin\beta_n x sin\omega_n t}{\omega_n} \tag{10}$$

Where l is the length of the beam; $\beta_n = n\pi/l$; and $\omega_n = a{\beta_n}^2$. To simply even further to appropriate this equation for the purpose of the study, the special case of $x_o = l/2$, in which the impact load acts at mid-span, results in $\beta_n x_o = n\pi/2$. Therefore, Eq. (10) can be written as

$$y(x,t) = \frac{2P}{\rho Al}\sum_{n=1,3,5}^{\infty}\frac{(-1)^{\frac{n-1}{2}} sin\beta_n x sin\omega_n t}{\omega_n} \tag{11}$$

The value of P in Eq. (11) is equal to the value F that was calculated in Eq. (7) for predicted impact force. When calculating the maximum predicted deflection using Eq. (11), Tang et al. (2005) used a total of five terms, that is, n = 1, 3, 5, 7, and 9. It is important to note that Eq. (7) and (11) applicable to only the first impact because the linear stiffness, EI, was derived from test results and will change after the first impact (Tang et al., 2005).

3. PROBLEM STATEMENT

Based on the results from Phase-I, it was determined that the use of rubberized tire chips as a coarse aggregate replacement in concrete mixtures have the potential to increase material toughness by increasing energy dissipation capacity (Stallings, 2017). Small-scale static and dynamic tests were conducted to test the mechanical properties of rubberized concrete mixtures at varying tire chip and crumb rubber replacement levels up to 50% coarse aggregate replacement and 40% fine aggregate replacement, respectively. It was ultimately determined that, based on performance and environmental impact, a 20% tire chip replacement of the coarse aggregate was the most optimal. Although the majority of mechanical properties such as compressive strength, modulus of rupture, and tensile strength decreased as a result of tire chip inclusion, drop-hammer impact tests showed that the rubberized concrete mixtures exhibited an increase in energy dissipation when compared to the control mixture. Furthermore, static load-deflection plots derived from small-scaled flexural tests supported these results as the rubberized mixtures showed increased residual strength over a longer period of time compared to the control.

Phase-II aims at taking the optimized rubberized tire chip mixtures from Phase-I to construct scaled beams which will be subjected to static and impact testing. A performance-based evaluation needs to be implemented that utilizes practical testing procedures to model impact testing. Truck impact tests on barrier walls are not always entirely practical for measuring total energy dissipation of rubberized concrete mixtures, and as a result, a computer-simulated model will be used to achieve these results

Figure 3-1. Truck Impact Testing (Left: Angled Collision, Right: Head-on Collision).

As a supplement, rubberized concrete mixtures will also include fiber reinforcement consisting of steel, polypropylene (PP), and polyvinyl alcohol (PVA) either isolated or in combinations. Existing literature has established that these three fiber types used in ECCs improve the ductility of concrete along with increasing toughness. Further research is needed to develop an optimized rubberized fiber reinforced (FRC) mixture which incorporates both tire chips and fiber reinforcement, takes into consideration environmental and economic impact, and meets the requirements of GDOT Class A concrete (3,000 psi, 20.7 MPa) for use in safety barriers and other applications.

4. RESEARCH OBJECTIVES AND PLANS

4.1 Objectives

The primary objectives of this study are to:

1. Optimize the relationship between recycled tire chip aggregates and fiber reinforcement to maximize total energy dissipation and impact resilience
2. Minimize the negative effects of recycled tire chips on mechanical properties by utilizing fiber reinforcement
3. Study the performance of rubberized FRC beams under scaled static and impact tests
4. Study the effects of fiber volume fraction and tensile steel reinforcement ratio
5. Produce a workable mixture that meets GDOT Class A specifications

In order to complete the above objectives, this study will consist of three separate phases (Part I and Part II, and Part III). Part I focuses on producing small-scale preliminary mixtures to observe the relationship between tire chips and fiber reinforcement and their effects on mechanical properties (i.e. compression, modulus of rupture, drop-hammer impact resilience). After the completion of preliminary testing and data analysis, the optimized mixture from Part I will be further observed in Parts II and III. Scaled beams of dimensions 7’6” length x 10” height x 6” width (2286 mm x 152.4 mm x 254 mm) will then be cast and tested under static and impact loads to maximize total energy dissipation and ductility.

4.2 Materials

The primary constituents used for the mixtures in this study are Portland cement, virgin coarse and fine aggregates, recycled tire chip aggregates, steel fiber, polypropylene fiber (PP), and polyvinyl alcohol fiber (PVA).

4.2.1 Cementitious Materials

As per Section 830 from the GDOT Supplemental Specification manual, concrete used in the state of Georgia is to contain Portland cement ranging from Type I to Type III, depending on the application. In compliance with ASTM C150 *Standard Specification for Portland Cement*, a Type I/II cement was used for the purpose of this study. No other cementitious materials were observed. Table 4.1 lists the physical and chemical properties of the cement used in this study.

Table 4.1 - Chemical and Physical Properties of Type I/II Cement

Chemical and Physical Properties		**Test Results**	**ASTM C150 Specifications**
SiO_2	(%)	19.7	---
Al_2O_3	(%)	4.7	6.0 max
Fe_2O_3	(%)	3	6.0 max
CaO	(%)	63.3	---
MgO	(%)	3.1	6.0 max
SO_3	(%)	3.2	3.0 max
CO_2	(%)	1.7	---
Limestone	(%)	4	5.0 max
$CaCO_3$ in Limestone	(%)	98	70 min
C_3S	(%)	54	---
C_2S	(%)	15	---
C_3A	(%)	7	8 max
C_4AF	(%)	9	---
C_3S+4.75 C_3A	(%)	89	100 max
Loss of Ignition	(%)	2.7	3.0 max
Blaine Fineness	(cm^2/g)	387	260 - 430
Air Content of PC Mortar	(%)	8	12 max
Specific Gravity		3.16	---

4.2.2 Natural Aggregates

All coarse and fine aggregates used in this study adhere to ASTM C33, GDOT Section 800 (coarse aggregate), and GDOT Section 801 (fine aggregate). The coarse aggregate was obtained from Hanson Aggregates East and were locally sourced from Athens, Georgia. The coarse aggregate size is a graded #57 stone (NMAS 1" (25.4 mm)) and is categorized as granite gneiss/amphibolite. The fine aggregate was sourced from Redland Sand, Inc. located in Watkinsville, Georgia and is categorized as an alluvial sand.

Sieve analysis was conducted on these natural aggregates in compliance with ASTM Standard C136, *Test Method for Sieve Analysis of Fine and Coarse Aggregates*, and the results are seen in Figures 4-1 and 4-2 for the coarse and fine aggregate, respectively.

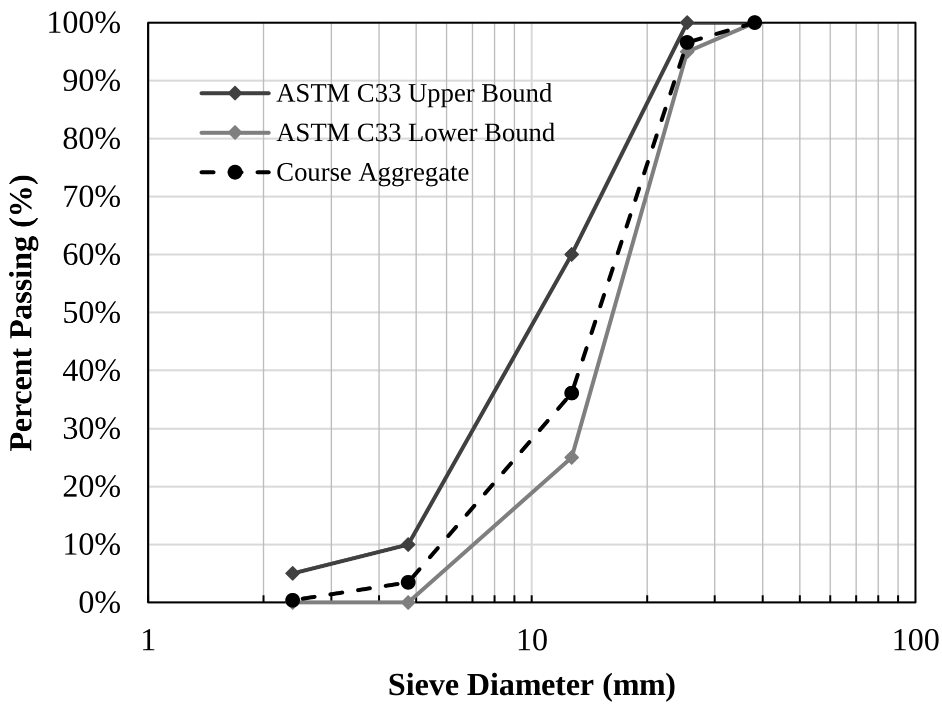

Figure 4-1. Sieve Analysis of Natural Coarse Aggregate in compliance with ASTM C136.

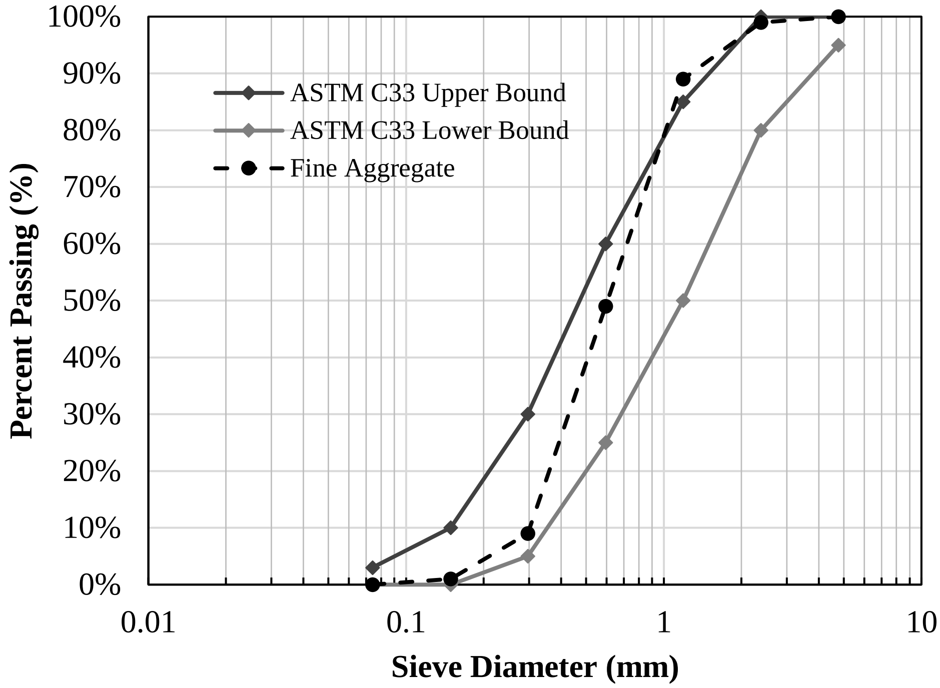

Figure 4-2. Sieve Analysis of Natural Fine Aggregate in compliance with ASTM C136.

4.2.3 Tire Chips

The tire chips used in this study were in compliance with ASTM D6270 *Standard Practice of Scrap Tires in Civil Engineering Applications.* Table 4.2 highlights specific terminology and defines their properties.

Table 4.2 - Definition of Terms Specific to ASTM D6270

Material	Minimum Size, in. (mm)	Maximum Size, in. (mm)
Rough Shred	1.96 x 1.96 x 1.96 (50 x 50 x 50)	30 x 1.96 x 3.94 762 x 50 x 100
Tire-Derived Aggregate (TDA)	0.47 (12)	12 (305)
Tire Chips	0.47 (12)	1.96 (50)
Granulated Rubber	< 0.017 (0.425)	0.47 (12)
Ground Rubber	< 0.017 (0.425)	0.079 (2)
Powdered Rubber	---	<0.017 (0.425)

For this particular study, only tire chips (0.47 to 1.96 in) were used to replace a percentage of the coarse aggregate. Although the size of the tire chips can exceed that of the coarse aggregate

(NMAS 1” (25.4 mm)), the sieve analysis of the tire chips, which was conducted in Phase-I (Stallings 2017), for the most part remains within the upper and lower bounds set by ASTM standards. The sieve analysis of the tire chips used in this study can be seen in Figure 4-3.

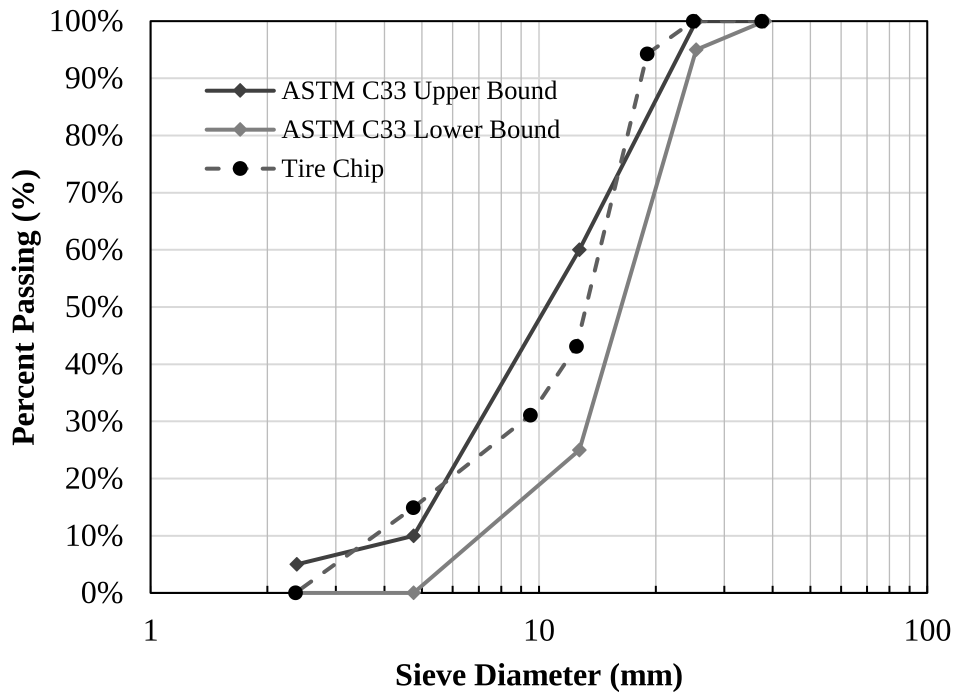

Figure 4-3. Sieve Analysis of Recycled Tire Chip in compliance with ASTM C136.

To directly compare the sieve analyses of the tire chips and the natural coarse aggregate, Figure 4-4 is provided. Although the particle sizes of the tire chips do not perfectly align with that of the coarse aggregate, they are similar enough to be used for the purpose of this study. For size comparison, Figure 4-5 shows the tire chips and coarse aggregates side by side.

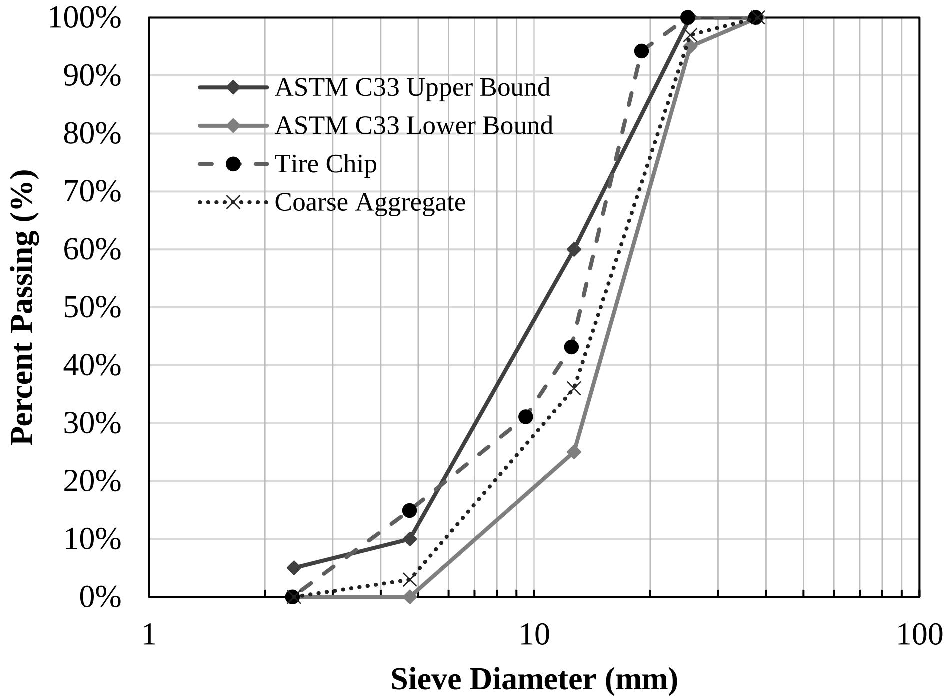

Figure 4-4. Sieve Analysis Comparison of Tire Chip and Coarse Aggregate in compliance with ASTM C136.

Figure 4-5. Tire Chip Size Comparison.

All rubberized mixtures in this study will contain a 20% volume fraction of the coarse aggregate. The results from Phase-I demonstrated that for the specific mixture design used, a 20% replacement of coarse aggregate exceeded the requirements of GDOT Class A concrete, demonstrated increased toughness up to 374% compared to the control, and proved to be the most cost effective option relative to the control (Stallings 2017).

4.2.4 Fiber Reinforcement

Three separate types of fiber were used in this study – steel, polypropylene (PP), and polyvinyl alcohol (PVA). Due to their lengths, steel (1.25 in.) and PP (2.25 in.) fibers were used specifically to bridge the macrocracks that develop in the concrete matrix under loading. Similarly, PVA (5/16 in.) fibers were used to bridge microcracks. Properties of each fiber can be seen in Table 4.3.

Table 4.3 - Properties of Fiber Reinforcement

Properties	Steel	Polypropylene	Polyvinyl Alcohol
Geometry	Hooked ends	Straight, Fibrillated	Straight, Monofilament
Tensile Strength, ksi (MPa)	195 (1345)	83-96 (570-660)	160-203 (1100-1400)
Young's Modulus, ksi (GPa)	30,458 (210)	290 (2)	6091 (42)
Specific Gravity	7.8	0.91	1.3
Length, in. (mm)	1.25 (30)	2.25 (54)	0.313 (8)
Diameter, in. (mm)	0.022 (0.55)	0.02 (0.5)	0.001 (0.038)

The steel, polypropylene, and polyvinyl alcohol fibers can be seen in Figures 4-6 through 4-8. A coin is placed alongside each fiber type to show relative size comparison.

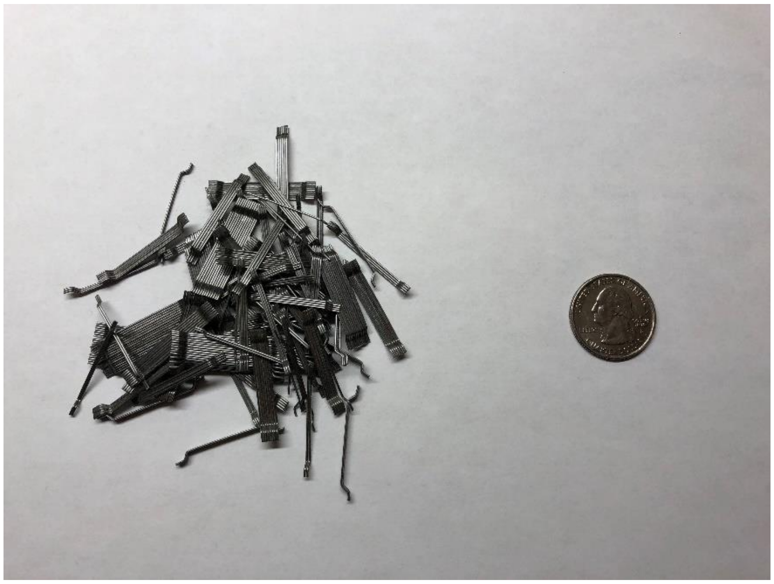

Figure 4-6. Steel Fiber Size Comparison

Figure 4-7. Polyvinyl Alcohol Fiber Size Comparison.

Figure 4-8. Polypropylene Fiber Size Comparison.

4.2.5 Chemical Admixtures

To ensure a quality mixture, chemical admixtures were utilized. Due to the nature of tire chips and fibers in reducing workability, a polycarboxlate-based high-range water-reducing (HRWRA) superplasticizer was used to increase slump. Typical recommended dosages for this specific admixture typically range from 2 to 15 fl. oz/cwt. As shown later, the quantity of HRWRA for the mixtures in this study ranged from 7 to 15 fl. oz/cwt and 5 fl. oz/cwt for Part I and Parts II and III, respectively. Quantities varied due to tire chip inclusion, type of fiber, and quantity of fiber.

Because the tire chips have a much lower specific gravity (1.12) than the coarse aggregate (2.65), the tire chips tended to float to the surface during the vibration process. As a result, a viscosity modifying agent (VMA) was used as a thickener to stagnate the tire chips and produce a more uniform mixture. The VMA was especially useful in mixtures that required higher dosages of HRWRA because it mitigated segregation of aggregates while at the same time providing a thixotropic reaction for highly fluid mixtures. Typical recommended dosages ranged from 5 to 8 fl. oz/cwt. Accordingly, the dosages used for this study ranged from 8 fl. oz/cwt and 5 to 6 fl. oz/cwt for Part I and Parts II and III, respectively. Similar to the HRWRA, the dosage varied as a result of quantity and type of material used.

To ensure the mixtures in this study adhered to GDOT Class A requirements for air content (2.5% to 6%), an air-entraining agent (AEA) was used. Air content is crucial to durability, especially in areas where freeze-thaw is prevalent. Typical dosages for the AEA used are within the range of 0.5 to 5 fl. oz/cwt. It was observed that 1.3 fl. oz/cwt was substantial in keeping the mixing within the acceptable range. The dosage remained constant for Parts I, II, and III as there was little variance in air content regardless of tire chip or fiber inclusion. All chemical admixtures used adhered to ASTM Standard C494, *Specification for Chemical Admixtures for Concrete*.

4.3 Methodology

All procedures in this study are in compliance with ASTM standards and ACI recommendations. Procedures used for batching, mixing, and curing were in compliance with ASTM C192 *Standard Practice for Making and Curing Concrete Test Specimens in the Laboratory.*

4.3.1 Batching Preparations

Prior to mixing, all materials were weighed out in 5 gallon buckets, which were color-coded for each specific material to avoid contamination, and were stored at room temperature (68 to 86˚F or 20 to 30˚C) 24 hours in advance with lids on to prevent moisture loss. The moisture content of the coarse and fine aggregates were measured shortly before the mixing process using a microwave oven, as per ASTM C566 *Standard Test Method for Total Evaporable Moisture Content of Aggregate by Drying*, ensuring the sample was well stirred and uniformly heated. After the moisture content of the aggregates was determined, the batch was re-proportioned accordingly to account for water content. Once all of the materials were prepared and shortly before mixing, the HRWRA, VMA, and AEA were measured and combined with the water used for mixing to disperse the admixtures uniformly.

Certain procedures were taken prior to mixing to maximize uniform distribution of fibers. The PP fibers used were initially in the form of twisted strands. To prevent clumping and provide a less varied comparison with the individual steel fibers, these strands were separated into individual strands. On the other hand, the steel fibers were submerged in the water used for mixing to saturate and weaken the adhesive bonding between the strands to ensure all fibers were separated. This preparation process was used for all parts of this study.

4.3.2 Preparation of the Molds

The types of molds used and preparation of molds are in compliance with ASTM C192 *Standard Practice for Making and Curing Concrete Test Specimens in the Laboratory* and ASTM C470 *Standard Specifications for Molds for Forming Concrete Test Cylinders Vertically*. Procedures for mold preparations differ between Part I and Parts II and III due to the difference in the scale of testing.

Plastic cylindrical molds were used for compression cylinders throughout this study. A small incision was created at the center of the base of the mold to assist with specimen releasing, which was done using an air compression apparatus. In Part I, similar procedures were taken with the drop-hammer impact disks. The flexural beam specimens were cast in a heavy gauge steel mold that disassembled to allow for specimen removal. It is important to note that every type of mold was greased with form oil for ease of release.

In Parts II and III, formwork used for scaled beam testing were constructed out of wood. To mitigate the absorptivity of the wood, the molds were thoroughly greased using concrete form oil. Several molds were constructed to replace any molds that were no longer useable.

4.3.3 Mixing Procedure

All mixing was done using a 12.5 ft³ capacity Workman *II* Multimixer, which can be found in Figure 4-9. After all of the materials were re-proportioned to account for moisture content and the molds were prepared, the materials were added to the mixer.

Figure 4-9. Workman *II* Multimixer.

Initially, all of the aggregates, including the tire chips, were placed into the rotating mixing drum. The mixer was then run for 7 to 8 minutes to induce mechanical abrasion of the tire chip surface. As observed in literature, surface roughening treatments have been effective at improving the bond between rubber particles and cement paste. Although chemical treatments tend to be very effective at inducing microscopic surface roughening, mechanical abrasion has shown to be adequate at achieving similar results (Stallings 2017).

The cement and water were then added incrementally. This was done to promote complete cement hydration while preventing clumps from developing. Chemical admixtures were added and stirred into the mixing water prior to mixing to maximize an even distribution of admixture to the water and cement. In between water and cement addition increments, the mixer was briefly paused and a scoop was used to relocate any un-hydrated material from the back of the mixer to the front. This process was repeated until all of the constituents (barring the fibers) were hydrated and properly mixed and during a period of 5 minutes.

Finally, after the batch was properly mixed, fibers were added incrementally. The reason for this practice was to prevent any clumping of fibers with the cement paste, which could potentially create a poor bond between the paste and the other constituents. This issue was more prevalent with PP and PVA fibers due to their own tendency to clump together. With the drum rotating, the fibers were slowly added by the handful and allowed to mix for an additional 2 minutes. The total allotted time for mixing was typically 15 minutes.

4.3.4 Fresh Concrete Properties

Each mixture was tested for slump, unit weight, air content, and temperature. It was imperative to perform proper quality control measures that were in compliance with testing standards. Table 4.4 represents each fresh property test with the appropriate ASTM and AASHTO standard used.

Table 4.4 – Fresh Concrete Properties Tested Under ASTM Standards

Fresh Property Test	Standard	Testing Day
Slump	ASTM C143 / AASHTO T119	Batching Day
Unit Weight	ASTM C138 / AASHTO T121	Batching Day
Air Content	ASTM C231 / AASHTO T152	Batching Day
Temperature	ASTM C1064 / AASHTO T309	Batching Day

Figure 4-10 shows the target fresh and hardened concrete properties required to fulfill GDOT Class A standards. As previously stated, chemical admixtures were used to reach these target values. Both English and metric units are reported.

English								
Class of Concrete	(2) Coarse Aggregate Size No.	(1 & 6) Minimum Cement Factor lbs/yd^3	Max Water/ Cement ratio lbs/lb	(5) Slump acceptance Limits (in) Lower-Upper		(3 & 7) Entrained Air Acceptance Limits (%) Lower-Upper		Minimum Compressive Strength at 28 days (psi)
"AAA"	67,68	675	.440	2	4	2.5	6.0	5000
"AA1"	67,68	675	.440	2	4	2.5	6.0	4500
"AA"	56,57,67	635	.445	2	4	3.5	7.0	3500
"A"	56,57,67	611	.490	2	4	2.5 (3)	6.0	3000
"B"	56,57,67	470	.660	2	4	0.0	6.0	2200
"CS"	56,57,67	280	1.400	-	3½	3.0	7.0	1000 (4)
	Graded Agg.*							

metric								
Class of Concrete	(2) Coarse Aggregate Size No.	(1 & 6) Mini mum Cement Factor kg/m^3	Max Water/ Cement ratio kg/kg	(5) Slump acceptance Limits (mm) Lower - Upper		(3 & 7) Entrained Air Acceptance Limits (%) Lower-Upper		Minimum Compressive Strength at 28 days (MPa)
"AAA"	67,68	400	.440	50	100	2.5	6.0	35
"AA1"	67,68	400	.440	50	100	2.5	6.0	30
"AA"	56,57,67	375	.445	50	100	3.5	7.0	25
"A"	56,57,67	360	.490	50	100	2.5 (3)	6.0	20
"B"	56,57,67	280	.660	50	100	0.0	6.0	15
"CS"	56,57,67	165	1.400		90	3.0	7.0	7 (4)
	Graded Agg.							

Figure 4-10. GDOT Fresh and Hardened Concrete Specifications (GDOT Supplemental Specification – Section 500).

4.3.5 Curing Concrete Specimens

Specimens were removed from their respective molds 24±8 hours after casting and set to cure for the proper amount of time prior to the testing date. For Part I mixtures, specimens were placed in curing tanks that were maintained at a constant 70˚F (21˚C). The curing tanks were filled with water saturated with calcium hydroxide. The curing tanks can be seen in Figure 4-11.

Figure 4-11. Temperature Regulated Curing Tanks.

For Part II and III mixtures, specimens were cured in burlap and maintained in a temperature-regulated environment. Due to the scaled beams exceeding the dimensional capacity of the curing tanks, the accompanying beam cylinders were also cured in burlap to maintain consistent curing conditions. Water was continuously added to the beams and covered in plastic to minimize evaporation. As a result, the relative humidity of the air surrounding the specimens was maintained at a near 100% for the duration of the curing process. The curing methods used in this study adhered to ASTM C511, *Specification for Mixing Rooms, Moist Cabinets, Moist Rooms*.

5. PART I – EXPERIMENTAL DESIGN AND RESULTS: DESIGN OF CEMENTITIOUS COMPOSITES

5.1 Preliminary Mixtures - Design

The initial phase of this project was ultimately to develop an optimized hybrid mixture consisting of fiber reinforcement and recycled tire chips before proceeding to scaled beam testing. Twelve preliminary mixtures were batched and tested, and of these twelve, eight were to be considered as mixture pairs. Of these eight, four contained a 20% coarse aggregate replacement of tire chips, while the other four did not. These mixture pairs were used to analyze the relationship between the tire chips and fiber reinforcement. The fibers used included steel, polypropylene (PP), and polyvinyl alcohol (PVA). All specimens were batched with the same w/cm ratio and cement content of 0.42 and 611 lb/yd^3 (362 kg/m^3), respectively.

5.1.1 Mixture Design

Each mixture design is summarized in Table 5.1. Numerations within the specimen name corresponds to the volume fraction of materials. For example, ST0.6-PV0.4-TC20 contains 0.6% steel fibers, 0.4% PVA fibers, and 20% tire chip replacement. The choice of fiber volume fractions and tire chip replacement contents in this study was based on previous studies conducted by Masud (2015) and Stallings and Durham (2017), respectively. A complete breakdown of the batch quantities can be seen in Appendix A.1.

Table 5.1 – Part-I Mixture Proportions by Volume

Mixture Designation	Fiber Reinforcement (Volume Fraction of Total Mixture) - % Addition			Tire Chip (Volume Fraction of C.A) - % Replacement
	% of Steel Fibers	% of Polypropylene Fibers	% of Polyvinyl Alcohol Fibers	% of Rubber Tire Chips
Control	0	0	0	0
ST1.0-PV0.0-TC0	1.0	0	0	0
PP1.0-PV0.0-TC0	0	1.0	0	0
ST0.5-PV0.5-TC0	0.5	0.5	0	0
PP0.6-PV0.4-TC0	0	0.6	0.4	0
ST1.0-PV0.0-TC20	1.0	0	0	20
PP1.0-PV0.0-TC20	0	1.0	0	20
ST0.6-PV0.4-TC20	0.6	0	0.4	20
PP0.6-PV0.4-TC20	0	0.6	0.4	20
ST0.0-PV0.0-TC20	0	0	0	20
ST0.5-PV0.0-TC20	0.5	0	0	20
ST0.75-PV0.0-TC20	0.75	0	0	20

5.1.2 Testing Mechanical Properties

These rubberized fiber reinforced concrete mixtures were tested for compressive strength, modulus of rupture (MOR), and drop-hammer impact resilience. The properties derived from these tests would be sufficient in predicting performance at a larger scale. Each test conducted, along with the corresponding standard, is seen in Table 5.2.

Table 5.2 – Mechanical Properties Tested Under ASTM and ACI Standards

Mechanical Property Test	Standard	Testing Day
Compression Test	ASTM C39	1, 7, 28 Days
Modulus of Rupture	ASTM C78	28 Days
Drop-Hammer Impact Test	ACI 544.2R	28 Days

5.1.2.1 Compression Test

To avoid any inconsistencies in the data, twelve 4 in. x 8 in. cylinders were batched per mixture. Four cylinders were tested on each testing day (1, 7, and 28) and the compressive strength was determined by averaging the three most consistent specimens, with exclusion of the outlier. Specimens were tested using a multipurpose testing apparatus under unconfined stress conditions in compliance with ASTM C39 *Standard Test Method for Compressive Strength of Cylindrical Concrete Specimens*.

5.1.2.2 Modulus of Rupture

Three 22 in. length x 6 in. width x 6 in. height prismatic beam specimens were produced per mixture. For testing purposes an 18 in span was considered. Specimens were subjected to the third point loading method found in ASTM C78 *Standard Test Method for Flexural Strength of Concrete (Using Simple Beam with Third-Point Loading)* as seen in Figure 5-1.

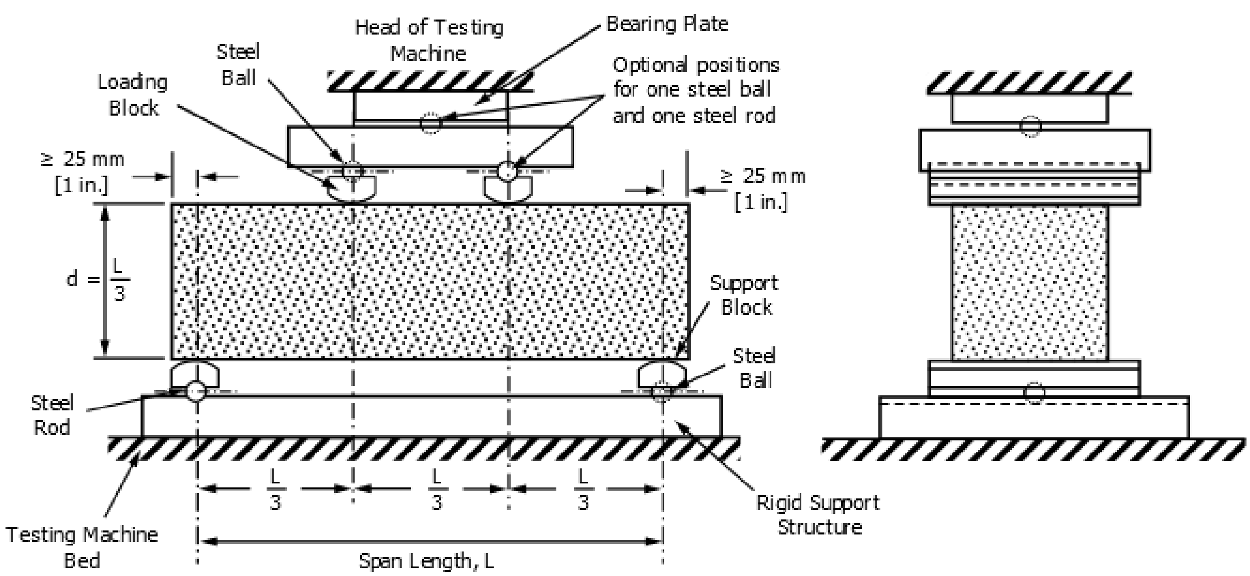

Figure 5-1. Side (Left) and End (Right) View Schematic of Flexural Testing Apparatus for Third-Point Loading Method (ASTM C78)

5.1.2.3 Drop-Hammer Impact Test

Determining the impact resilience of preliminary mixtures was crucial in ultimately deciding which mixture would be used for scaled beam testing. Three disks were cast per mixture with dimensions of 6 in. diameter x 2 in. height (152 mm x 51 mm). The testing method used was based on a recommended standard found in ACI 544.2R. The testing apparatus can be seen in Figure 5-2. The 10 lb (4.5 kg) drop-hammer used possessed a 2 in. (51mm) diameter face and a drop height of 18 in. (457 mm).

Figure 5-2. Drop-Hammer Apparatus: Top View (Left) and Isometric View (Middle); and 10 lb Drop Hammer (Right).

5.2 Fresh Concrete Properties

For quality control measures, each mixture was tested for its fresh properties upon batching. The goal was to meet specifications for GDOT Class A concrete, and as a result, admixture dosages were planned accordingly. Chemical admixtures were used in each mixture and their dosages depended on total batch size. A high-range water reducing admixture (HRWRA) was used because, based on previous testing and literature, both tire chips and fiber reinforcement tend to decrease workability. As a result, certain mixtures, especially those that contained PVA fibers, required higher HRWRA dosages in order to produce some workability given the mixture design. However, higher dosages of HRWRA sometimes caused a greater extent of segregation between the tire chips and cement paste. It was also clear that unless a viscosity modifying agent (VMA) was used, a significant number of tire chips would rise to the surface and result in a non-uniform mixture. An air entraining agent (AEA) was used to achieve an air content that was in line with specification. Fresh concrete property results for all Part-I mixtures are summarized in Table 5.3.

Table 5.3 – Fresh Concrete Property Results for Part-I Mixtures

Mixture Description	Slump, in (mm)	Temperature, F° (C°)	Unit Weight, lb/ft³ (kg/m³)	Air Content, %
Control	3.75	77	145.8	4.2
ST1.0-PV0.0-TC0	0	92.5	145.44	6.1
PP1.0-PV0.0-TC0	0	75	145.2	3.3
ST0.5-PV0.5-TC0	0	92.1	142.2	5.3
PP0.6-PV0.4-TC0	0	89.1	140.6	6.8
ST1.0-PV0.0-TC20	0.25	88.2	141.8	1.9
PP1.0-PV0.0-TC20	4	91.4	136	4.8
ST0.6-PV0.4-TC20	0	92.7	140.6	2.9
PP0.6-PV0.4-TC20	1	91	135.8	4.6
ST0.0-PV0.0-TC20	0.5	83.8	139	5.0
ST0.5-PV0.0-TC20	0.5	75.4	139.8	3.6
ST0.75-PV0.0-TC20	1.5	62.8	141.6	4.5

5.2.1 Slump

For any concrete application, workability is an important factor in achieving optimal compaction. Mixtures containing fiber reinforcement and tire chips required higher dosages of chemical admixture to achieve sufficient workability. The first half of these preliminary mixtures, those which did not contain tire chips, were tested for slump after the fibers had been added. It became clear that fibers were causing the slump test to be ineffective because they were hindering the flow of the batch, resulting in very low slump. The ACI guide (ACI 544.2R, 2009) indicates that the slump may not be a good indicator of workability for FRC. As a result, selected mixtures that contained tire chips were tested for slump prior to the inclusion of fibers and after the addition of tire chips. The results for slump are shown in Figure 5-3. Values for slump range from 0 to 4.5 in. (114 mm).

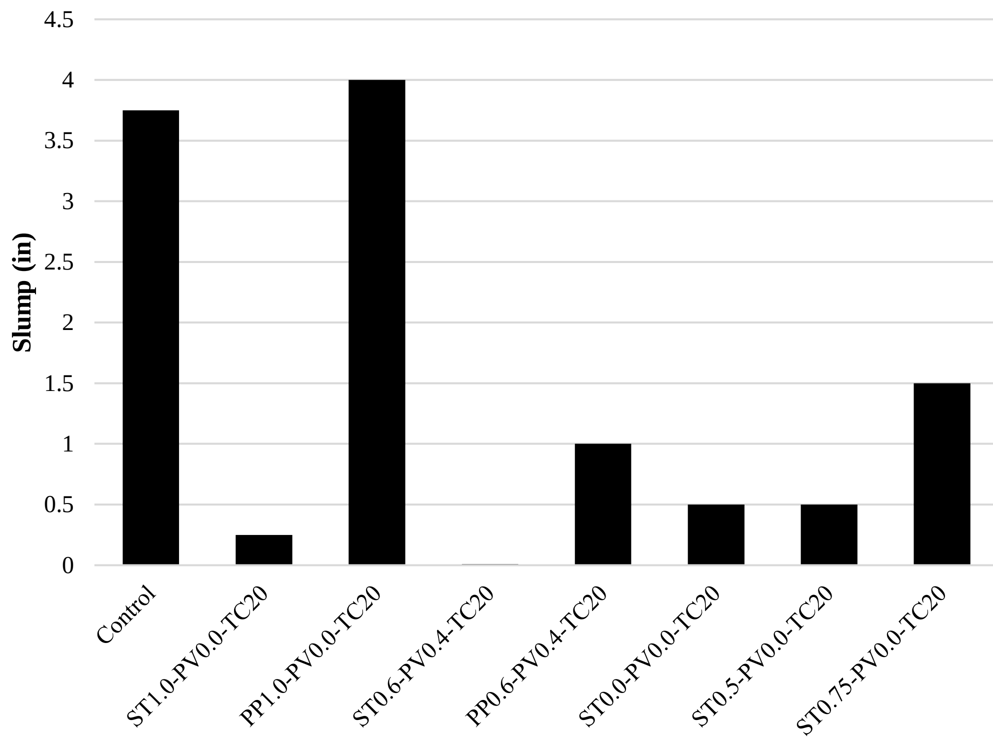

Figure 5-3. Slump Test Results for Selected Part I Mixtures.

Mixtures containing tire chips demonstrated somewhat sporadic slumps. Because the mixtures that did not contain tire chips were tested after the addition of fibers, only the control mixture can be used as a point of reference when comparing the effects of tire chips on slump. In this case, tire chips seemed to have a definite impact on slump. As seen in Table 5.4, the replacement of coarse aggregate with tire chips significantly decreased slump for the majority of mixtures.

Table 5.4 – Effect of Tire Chip Inclusion on Slump

Mixture Description	Slump, in (mm)	Percent Reduction Relative to Control, %
Control	3.75	0
ST0.0-PV0.0-TC20	0.5	86.7
ST1.0-PV0.0-TC20	0.25	93.3
PP1.0-PV0.0-TC20	4.0	-6.6
ST0.6-PV0.4-TC20	0.0	100
PP0.6-PV0.4-TC20	1.0	66.6
ST0.5-PV0.0-TC20	0.5	86.7
ST0.75-PV0.0-TC20	1.5	60

Ultimately, regardless of slump, the most workable rubberized FRC mixtures were those that contained solely steel fibers as opposed to PP and PVA. This was because clumping was experienced with both PP and PVA fibers. In the worst cases, the PVA fibers would absorb moisture from the cement paste and cause the paste to segregate from the aggregates. Based on the mixture design, it was deemed that the quantity of PVA fibers would have to reduced, potentially to 0.2% of the total 1% volume fraction, in order to be practical for cast in place applications. For these reasons, it was determined that the most practical mixture design to continue to the Part II phase of this study were those containing only steel fibers and tire chips.

5.2.2 Unit Weight

Because the tire chips used possess a lower specific gravity than the coarse aggregate, it was expected that the unit weight of mixtures containing tire chips would decrease total unit weight. The type of fiber used also had an impact on unit weight. Mixtures that contained steel fibers were typically denser than those that contained PP and PVA fibers. These observations can be seen in Figure 5-4.

The unit weights ranged from 135.8 lb/ft^3 (PP0.6-PV0.4-TC20) to 145.8 8 lb/ft^3 (Control). Taking into account all of the mixture pairs (equivalent mixtures with and without tire chips), there was an average 3.8% decrease in unit weight with tire chips inclusion. The difference in unit weight between the Control and ST0.0-PV0.0-TC20 was 4.6%. As a result, mixtures containing tire chips can be considered lighter than standard normal weight concrete.

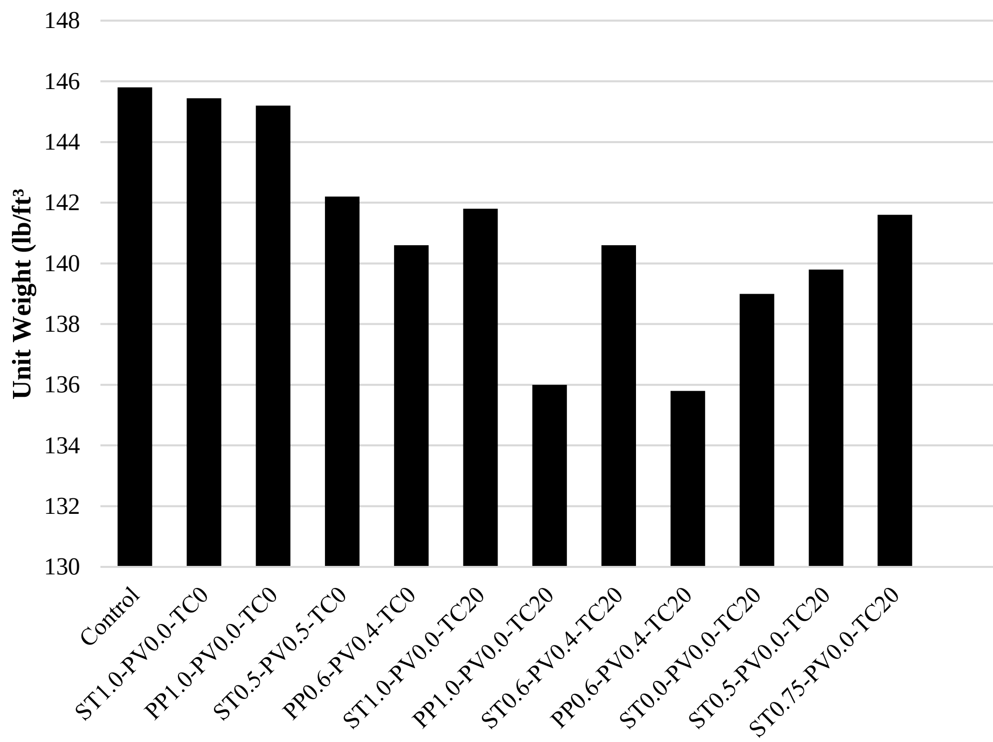

Figure 5-4. Unit Weight Results for Part I Mixtures.

5.2.3 Air Content

For the purpose of this study, the target entrained air content for GDOT Class A concrete is to be between 2.5% and 6.0%. The AEA used was dosed accordingly at 1.3 fl oz./cwt and this dosage was maintained throughout the course of this study. As seen in Figure 5-5, nine of the twelve mixtures were within the 2.5% to 6.0% range. While there appears to be no clear trend between air content and tire chip/fiber inclusion, it can be said that the mixtures containing tire chips and fibers seemed to have similar average air contents compared to the Control.

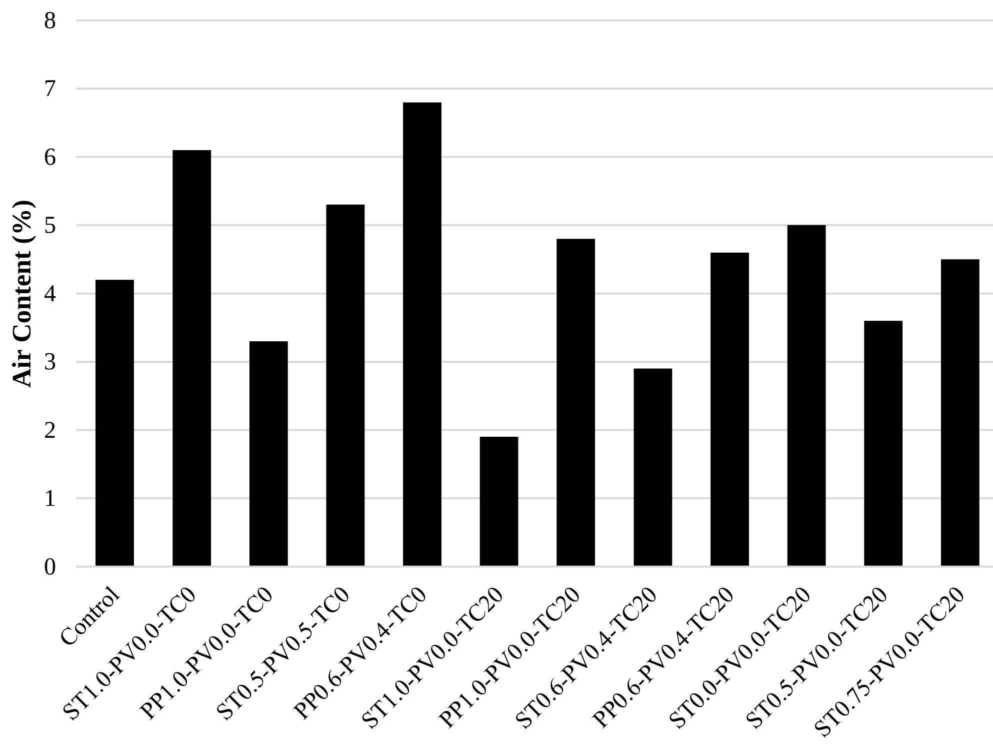

Figure 5-5. Air Content Results for Part I Mixtures.

5.2.4 Placement Temperature

Concrete batching temperature has been linked to performance in terms of strength and durability. It is widely accepted that the ideal ambient temperature range to batch concrete is between 50 and 85° F (10 to 32° C) for efficient cement hydration, and temperatures exceeding 90° F (32.2° C) should be avoided to prevent plastic shrinkage and loss of strength (Kardos et al., 2015).

Some mixtures batched in Part-I slightly exceeded to 85° F maximum limit. The concrete was batched outdoors in hot summer temperatures, leading to the concrete exceeding the recommended maximum. However, the hardened concrete was immediately placed indoors in a controlled environment at room temperature. As a result, during the hardening process, the concrete temperature was able, to a certain degree, stabilize to more acceptable temperatures. Temperatures for the Part I mixtures can be seen in Figure 5-6.

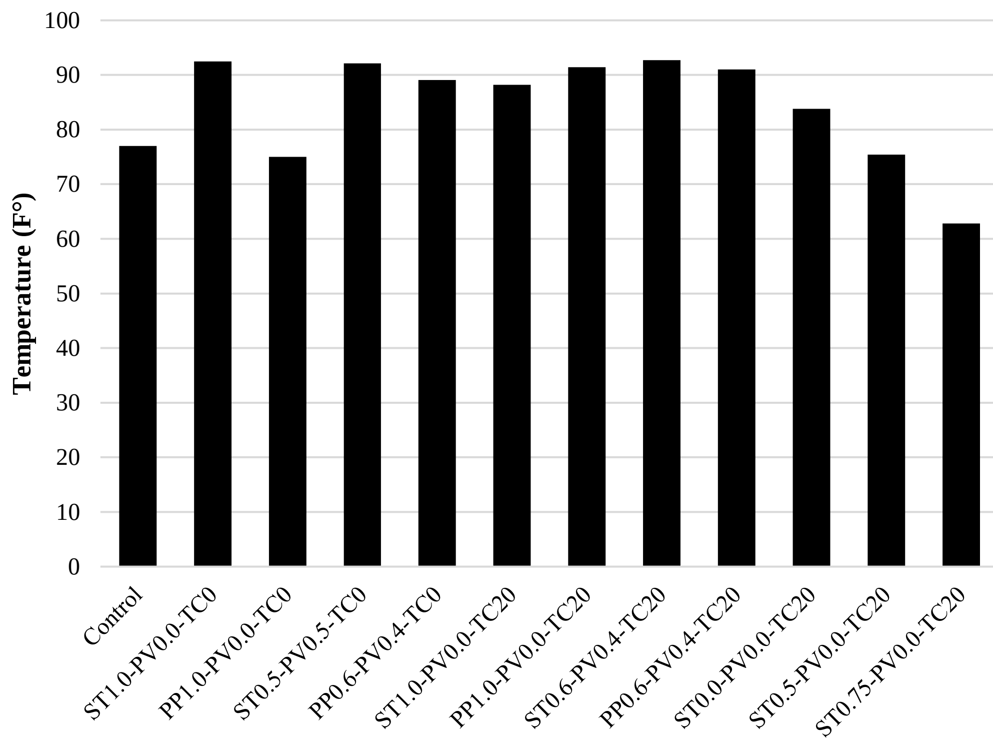

Figure 5-6. Temperature Results for Part I Mixtures.

5.3 Hardened Concrete Properties

5.3.1 Compressive Strength

All compression tests were performed in accordance with ASTM C39. Compressive strength minimums are as per Section 500 of the GDOT Supplemental Specification. Class AA, Class A, and Class B concrete must possess a minimum of 3,500 psi (25 MPa), 3000 psi (20 MPa), and 2,200 psi (15 MPa), respectively. For the purpose of this study, the concrete used adhered to the target requirements of Class A concrete used for Phase-I of this study (Stallings, 2017).

The results for compressive strength were in line with what was expected from literature. Every mixture, including those that contained tire chips, exceeded the minimum requirements for Class A concrete. Values for compressive strength at 28-days ranged from 3002 psi (20.7 MPa) to 8976 psi (61.9 MPa) and are represented in Table 5.5.

Table 5.5 – Average Compressive Strength of Part I Mixtures

	Average Compressive Strength, psi (MPa)		
Mixture Description	**1-Day**	**7-Day**	**28-Day**
Control	3755	5805	7128
ST1.0-PV0.0-TC0	4524	6870	8976
PP1.0-PV0.0-TC0	2700	4569	5843
ST0.5-PV0.5-TC0	2536	5509	7289
PP0.6-PV0.4-TC0	2159	4125	5351
ST1.0-PV0.0-TC20	1503	2736	3637
PP1.0-PV0.0-TC20	1454	2544	3002
ST0.6-PV0.4-TC20	2181	3716	3908
PP0.6-PV0.4-TC20	1723	3010	3290
ST0.5-PV0.0-TC20	1685	3159	3585
ST0.75-PV0.0-TC20	1324	2834	3759

It is apparent that the inclusion of tire chips significantly diminished the compressive strength of each mixture pair, up to 59%. Table 5.6 shows the overall compressive strength reduction of each mixture when tire chips were used. Despite this loss in strength, the fiber reinforcement prevented each mixture from falling below the minimum 3,000 psi (20 MPa).

Table 5.6 – Reduction of Compressive Strength with Tire Chip Inclusion

Mixture Description	Compressive Strength Reduction, %
ST1.0-PV0.0-TC0 / ST1.0-PV0.0-TC20	59.0
PP1.0-PV0.0-TC0 / PP1.0-PV0.0-TC20	48.6
ST0.5-PV0.5-TC0 / ST0.6-PV0.4-TC20	46.4
PP0.6-PV0.4-TC0 / PP0.6-PV0.4-TC20	38.5

Another item to note with the rubberized mixtures is the impedance of compressive strength development over the span of 28-days. The average compressive strength increase from 7-day to 28-day for mixtures that did not contain tire chips was 28.7%, whereas mixtures with tire chip inclusion increased by only 18.6%. The rate of strength development can be seen in Figure 5-7, noting that the mixtures including fiber reinforcement are denoted by the dashed lines. Alternatively, the total strength development per testing day can be seen in Figure 5-8.

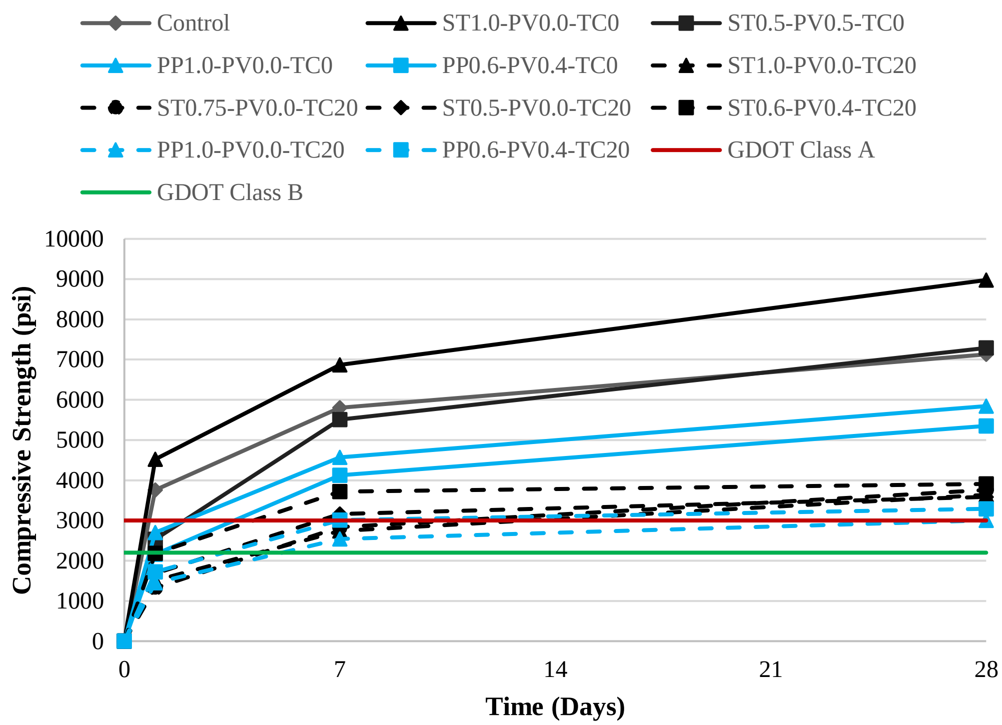

Figure 5-7. Average Compressive Strength of Part I Mixtures.

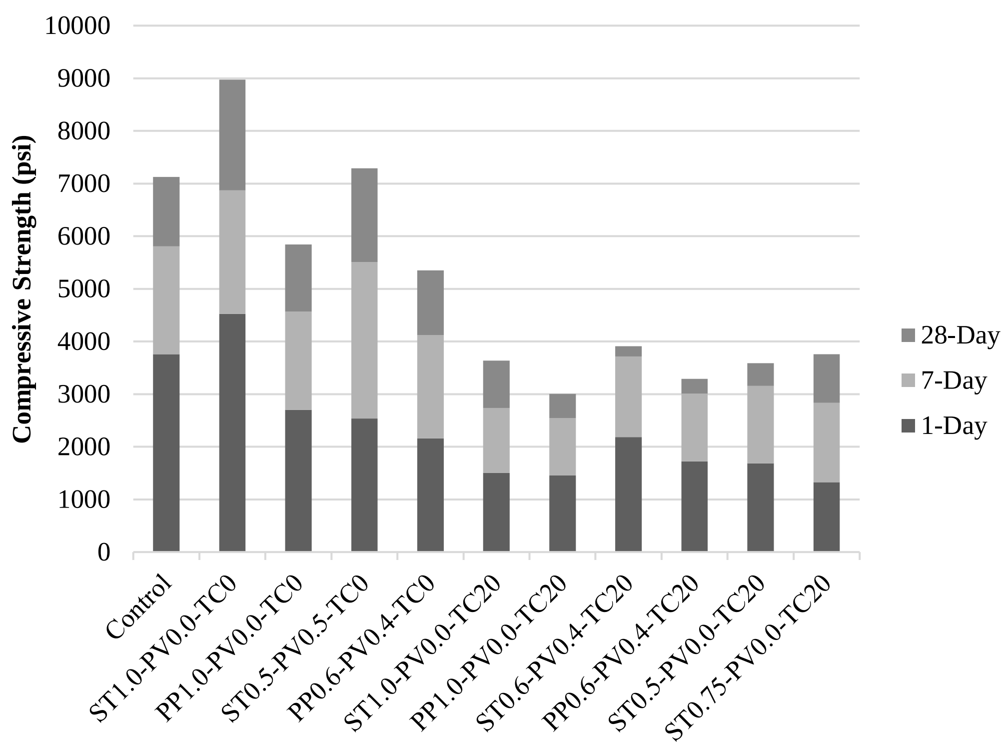

Figure 5-8. Total Compressive Strength Gain of Part I Mixtures.

Based on the compressive strength data, the inclusion of steel fibers increased compressive strength at a greater capacity than PP fibers. Furthermore, the inclusion of PVA fibers in conjunction with steel and PP fibers decreased compressive strength, although greater residual strength was observed. The PVA fibers were effective in bridging microcracks within the concrete matrix and extended the testing time before reaching ultimate failure. Figure 5-9 illustrates the comparison between failures of the Control and fiber/tire chip composite mixtures.

Figure 5-9. Comparison of Compression Cylinders at Failure: Control (Left) and Rubberized Steel Fiber Hybrid (Right)

5.3.2 Flexural Strength

The modulus of rupture (MOR) is a measure of a material's flexural strength. Although not a direct measure of tensile strength, MOR is considered to be positively correlated. Because there are currently no requirements for MOR in GDOT Class A specifications, the objective was to design mixtures that were either comparable or better performing than the Control. At the preliminary scale, MOR was an important characteristic that was heavily considered before transitioning to scaled beam testing.

Three prismatic beams with dimensions of 6 in. x 6in. x 22in. were formed per mixture and tested at a span of 18 in. under ASTM C78 specifications. Results ranged from 430 psi (3.0 MPa) to 1058 psi (7.3 MPa) and can be seen in Table 5.7.

Table 5.7 – Average Flexural Strength of Phase-I Mixtures

Mixture Description	Average 28-Day MOR, psi (MPa)
Control	666
ST1.0-PV0.0-TC0	1058
PP1.0-PV0.0-TC0	430
ST0.5-PV0.5-TC0	883
PP0.6-PV0.4-TC0	532
ST1.0-PV0.0-TC20	782
PP1.0-PV0.0-TC20	520
ST0.6-PV0.4-TC20	769
PP0.6-PV0.4-TC20	536
ST0.5-PV0.0-TC20	681
ST0.75-PV0.0-TC20	649

Unlike with compressive strength, tire chip inclusion did not distinctly reduce MOR in every case. Specimens that contained PP fibers either showed an increase in MOR or no change. The differences in MOR between mixture pairs can be seen in Table 5.8.

Table 5.8 – Reduction of MOR Strength with Tire Chip Inclusion

Mixture Description	MOR Strength Reduction, %
ST1.0-PV0.0-TC0 / ST1.0-PV0.0-TC20	26.1
PP1.0-PV0.0-TC0 / PP1.0-PV0.0-TC20	-20.9
ST0.5-PV0.5-TC0 / ST0.6-PV0.4-TC20	12.9
PP0.6-PV0.4-TC0 / PP0.6-PV0.4-TC20	-0.1

Although the hybrid effects of tire chips and fibers seemed to show no obvious trend in flexural strength, it was observed that these rubberized FRC mixtures exhibited significantly increased ductility. Similar to the observations made from the compression test, the testing duration to achieve ultimate failure significantly increased compared to the Control due to the increase in residual strength. While the PVA fibers bridged together the microcracks that developed, the larger steel and PP fibers bridged together the macrocracks. Meanwhile, the tire chips reduced the overall stiffness of each specimen and allowed for a more ductile response when experiencing load. The resultant specimens showed clear increase in the displacement at mid-span, although they reached ultimate failure load, and thus were held together by fibers and tire chips until the crack growth and separation in the crack plane was observed. The displacement and toughness of selected mixtures are measured in larger beam specimens and are documented in Chapter 6.

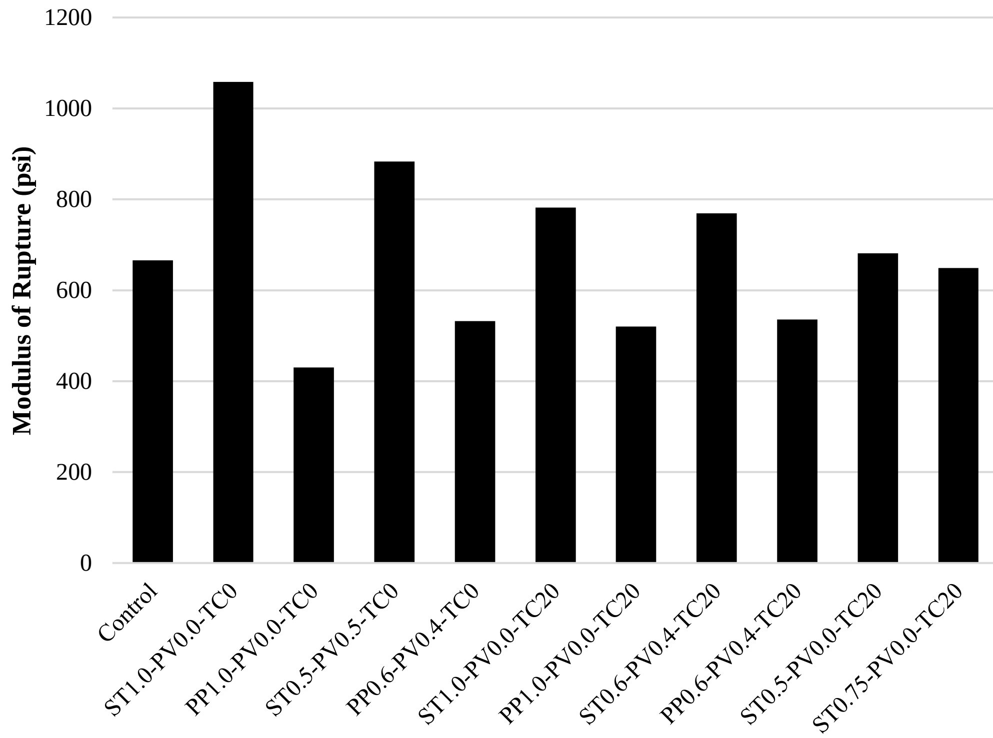

Figure 5-10. Average MOR Strength of Part I Mixtures.

Figure 5-11. Isometric Comparison of MOR Specimens at Failure: Control (Left) and Rubberized PP Fiber Hybrid (Right)

5.3.3 Drop-Hammer Impact Resilience

Although compressive and flexural strength were heavily considered, impact resilience became the deciding factor as to which mixtures would move on into the impact evaluation portion of the Part-II phase of this study. The goal of testing these small-scale specimens was to observe the effectiveness of different types of fibers with a 20% coarse aggregate replacement with tire chips by volume. Previous research has shown that tire chips have the capability of absorbing loads due to impact and dissipate the resulting energy to the rest of the structure (Ismail et al., 2016). This quality, coupled with the ability of fibers to bridge cracks, was used to develop an optimal concrete mixture that was superior to the Control under impact loading.

In accordance with ACI 544.2R, concrete disks, with dimensions of a 6 in. (152mm) diameter and 2 in. (51mm) height, were placed in a steel containment apparatus (see Figure 5-2). A 10 lb drop-hammer was then used to repeatedly apply a load on each specimen (about 1 drop every 2 seconds). Selected mixtures comparing the fracture responses between the Control and mixtures with 20% tire chip replacement can be seen in Figure 5-12. Even just tire chip inclusion alone was sufficient in reducing crack width and kept the specimen in one piece at ultimate failure.

Figure 5-12. Fractured Impact Disk Comparison: Top (Control), Bottom (20% Tire Chip)

The test was conducted taking points at 3 stages: initial crack, control failure, and ultimate failure. The initial crack was recorded as soon as the first sign of a crack was observed. From there, the hammer was dropped on the specimen until a second crack was seen. This crack is referred to as a ‘Control Failure’ and was used as a reference to observe how well the fibers and tire chips were able to dissipate energy before reaching ultimate failure. In most cases, the specimen was considered to achieve ultimate failure at 3 cracks that all met at the center of the specimen. In some rare cases, the specimen would reach ultimate failure by cracking straight down the middle, rather than at 3 points. It is important to note that while the control specimen achieved complete separation at ultimate failure, the rest of the specimens were still held together by tire chips and fibers. Results for the drop-hammer impact test can be seen in Table 5.9 and Figure 5-13. There was a 3525% increase in the number of drops need to reach ultimate failure from the Control to ST0.75-PV0.0-TC20, failing at 8 drops and 290 drops, respectively.

Table 5.9 – Average Drop Hammer Impact Results of Part I Mixtures

Mixture Description	Initial Crack	Control Failure	Ultimate Failure
Control	6	6	8
ST0.0-PV0.0-TC20	13	16	22
ST1.0-PV0.0-TC0	36	69	135
PP1.0-PV0.0-TC0	25	49	121
ST0.5-PV0.5-TC0	56	99	236
PP0.6-PV0.4-TC0	31	65	99
ST1.0-PV0.0-TC20	25	27	85
PP1.0-PV0.0-TC20	42	71	183
ST0.6-PV0.4-TC20	38	63	127
PP0.6-PV0.4-TC20	42	111	237
ST0.5-PV0.0-TC20	25	50	62
ST0.75-PV0.0-TC20	132	220	290

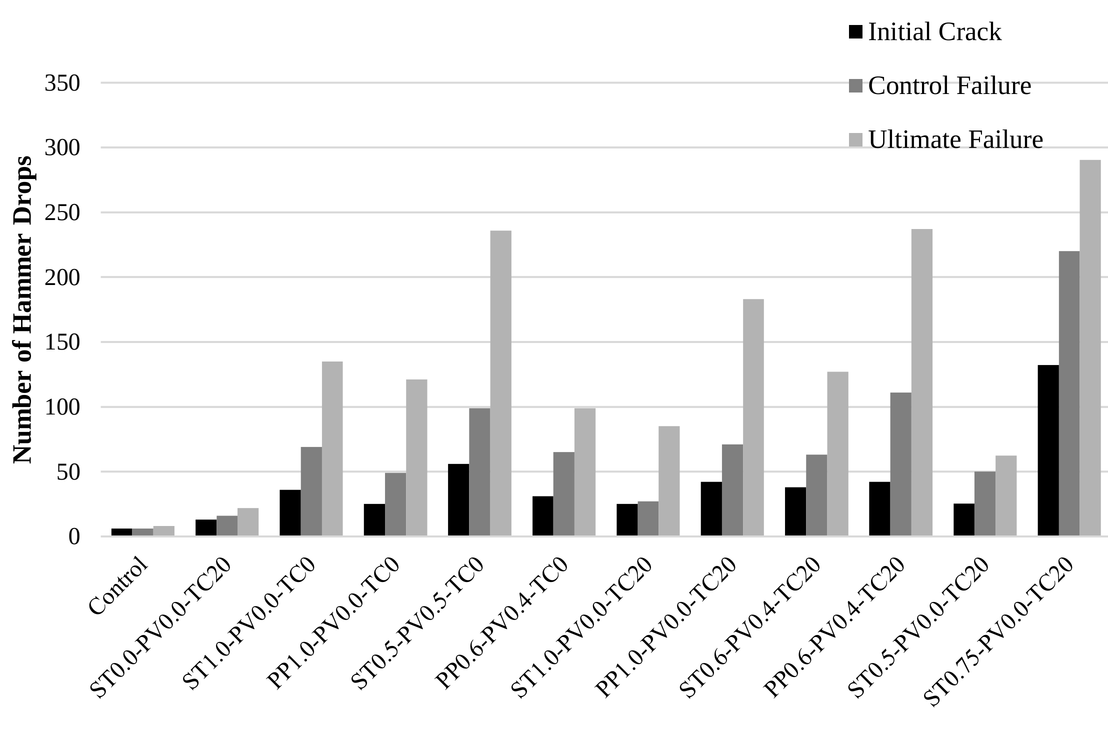

Figure 5-13. Average Drop-Hammer Impact Results of Part I Mixtures.

As observed in Figure 5-12, each mixture performed significantly better than the Control. The specimen that contained exclusively tire chips, ST0.0-PV0.0-TC20, required twice as many drops to reach ultimate failure compared to the Control. However, it was not until fibers were added that the significant improvement in impact resilience can be seen. The effectiveness of tire chip performance in relation to each mixture pair cannot be determined with certainty. While the mixtures containing steel and PVA exhibited a decrease in impact resistance, mixtures containing PP and PVA seemed to significantly benefit from them, although their inclusion do not provide sufficiently workable concrete. This data is highlighted in Table 5.10.

Table 5.10 – Increase of Drop-Hammer Impact Resilience with Tire Chip Inclusion

Mixture Description	Increase of Impact Resistance, %
ST1.0-PV0.0-TC0 / ST1.0-PV0.0-TC20	-37.7
PP1.0-PV0.0-TC0 / PP1.0-PV0.0-TC20	51.2
ST0.5-PV0.5-TC0 / ST0.6-PV0.4-TC20	-46.2
PP0.6-PV0.4-TC0 / PP0.6-PV0.4-TC20	139.4

5.4 Analysis of Steel Fiber Volume Fraction on Mechanical Properties

A further analysis was conducted on mixtures specifically containing steel fibers. Based on the data collected, it was clear that mixtures containing steel fibers exhibited increased performance in compressive strength, flexural strength, and drop-hammer impact resilience. Although PP and PVA fibers provided some promising data, the workability of these mixtures were seriously taken into consideration. Mixtures containing steel fibers were significantly more workable, which is an absolute necessity for cast-in-place operations.

In the presence of tire chips, the optimum steel fiber volume fraction may differ from normal concrete mixtures. All of the hybrid mixtures containing steel fibers and tire chips have been isolated in Figures 5-14 through 5-17 in order to establish a more clear comparison between varying volume fractions of steel fiber (V_{sf}) in the presence of tire chips.

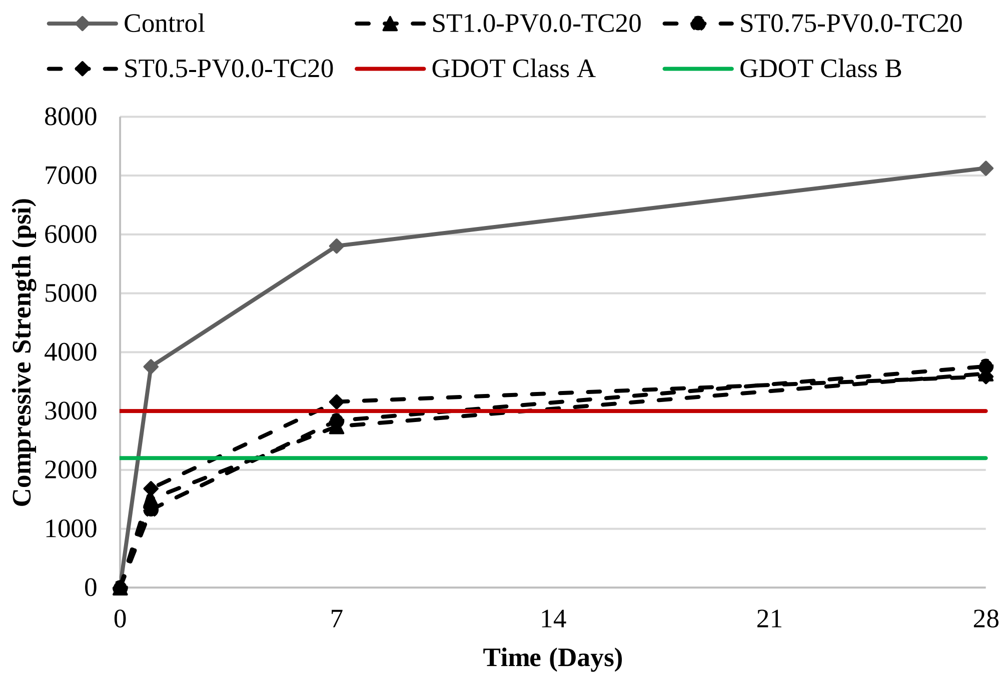

Figure 5-14. Average Compressive Strength Observing Varying V_{sf}.

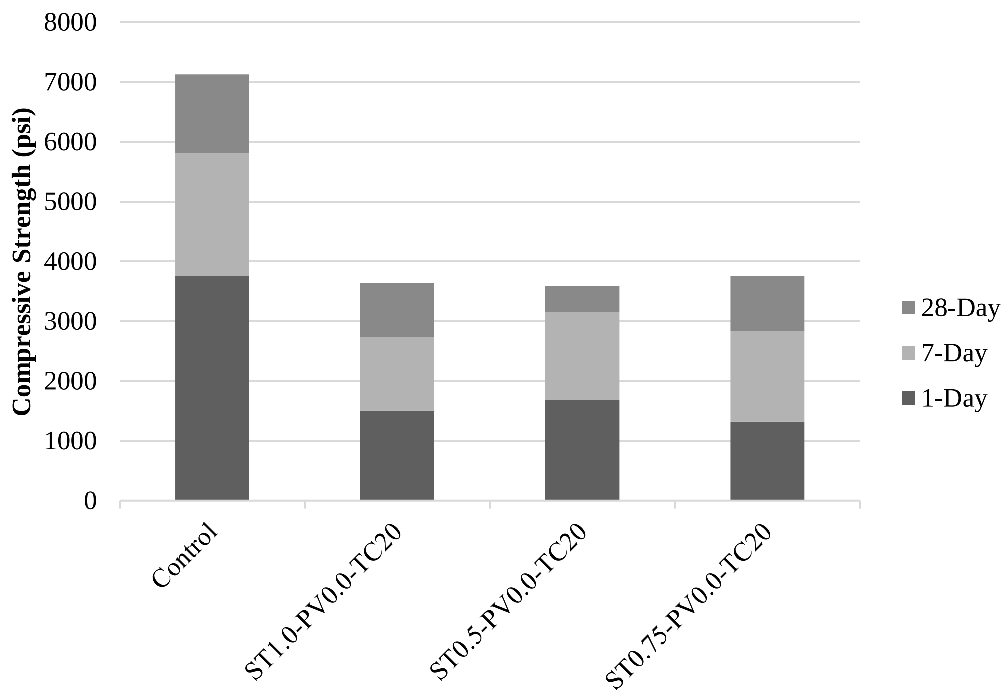

Figure 5-15. Total Compressive Strength Gain Observing Varying V_{sf}.

In terms of compressive strength and rate of strength development, the three steel/tire chip mixtures all demonstrated similar results. Based on the results from Figures 5-14 and 5-15, steel fiber volume fraction has insignificant effect on compressive strength ranging from 0.5% to 1.0%. All three specimens exceeded the required 3,000 psi (20MPa) minimum at 28 days.

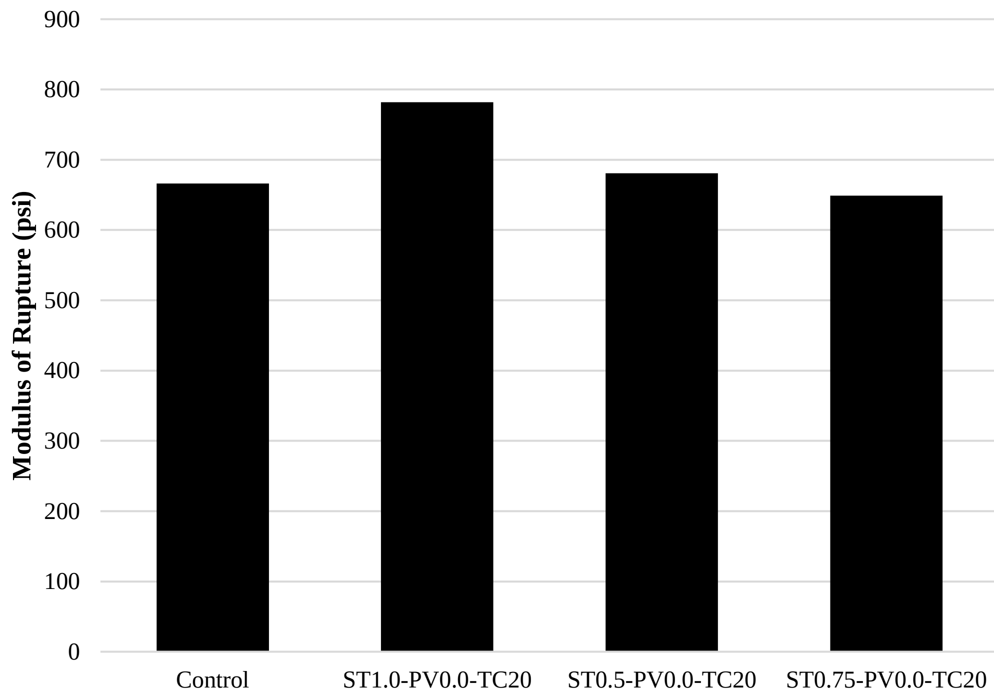

Figure 5-16. Average MOR Strength Observing Varying V_{sf}.

From Figure 5-16, steel fiber volume fraction appears to have some effect on MOR. However, the correlation is unclear based on this data. As expected, the MOR of STC0.75-PV0.0-TC20 would fall in between STC1.0-PV0.0-TC20 and STC0.5-PV0.0-TC20. Instead, STC0.75-PV0.0-TC20 fell even below the Control specimen, which was unexpected considering specimens containing steel fibers were the only specimens able to exceed the MOR of the Control. Regardless of this fact, steel fibers are good at counteracting the diminishing effects on strength resulting from tire chips.

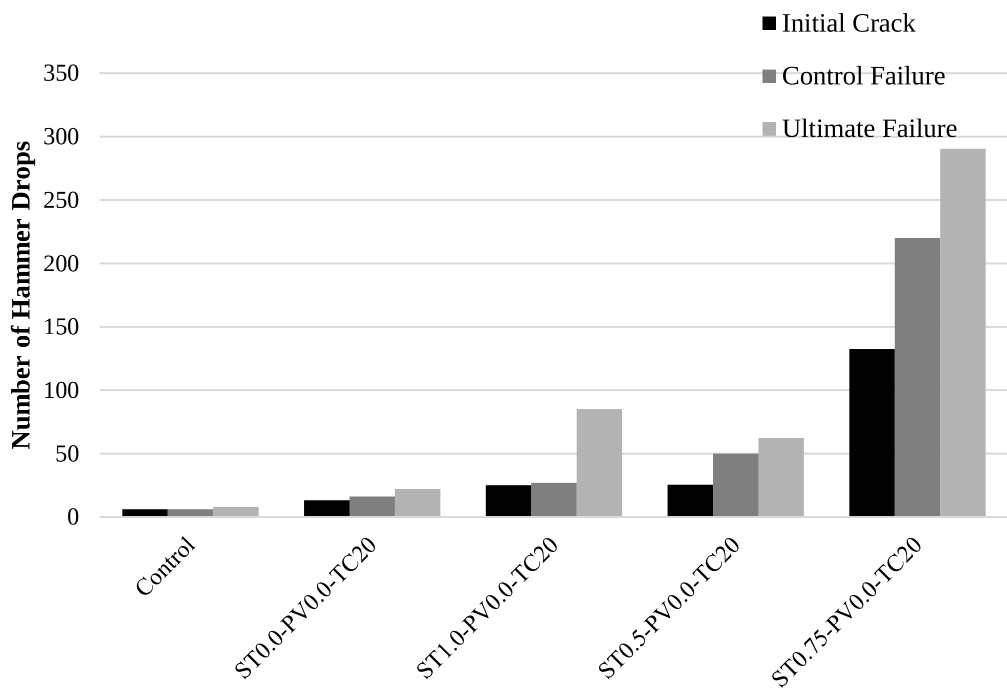

Figure 5-17. Average Drop-Hammer Impact Results Observing Varying V_{sf}.

Finally, Figure 5-17 shows the isolated results for the drop-hammer test of specimens ranging from steel fiber volume fractions of 0.5% to 1.0% along with the Control and 20% tire chip mixtures for comparison. Unlike the results from the compression and MOR tests, there appears to be a correlation with steel fiber volume fraction and impact resistance. Based on previous research, it was initially expected that the mixture containing 1.0% steel would outperform the mixtures with less steel (Masud, 2017). However, 0.75% steel appears to be the optimum percentage when combined with tire chips. The results from ST0.5-PV0.0-TC20 are reasonable because there is not enough steel fibers to produce adequate reinforcement. Inversely, ST1.0-PV0.0-TC20 appears to contain too much steel, causing the fibers to clump and producing an inadequate distribution and thus a poor bond between the steel fibers, concrete, and tire chips in the concrete matrix.

It is interesting to note, however, the difference between the control failure and ultimate failure of these mixtures. While ST0.5-PV0.0-TC20 and ST0.75-PV0.0-TC20 exhibited a constant trend from one failure to another, ST1.0-PV0.0-TC20 was able to redistribute the load after the control failure and resist failure several drops later. This is reasonable due to the increased amount of steel fibers.

5.5 Summary of Preliminary Test Results

The preliminary design of the optimized cementitious composites led to moving forward with hybrid mixtures consisting varying fiber volume fractions of steel fibers and tire chips. Although the tire chips significantly reduced mechanical strength properties, it was observed that steel fibers were able to counteract these effects at a greater capacity than PP and PVA fibers. Apart from increased mechanical performance, the workability of the mixture was significantly greater with steel fibers. However, based on further analysis of the steel fiber volume fraction, it was unclear whether 0.75% or 1.0% was optimal. Flexural strength was greater with 1.0%, however 0.75% showed significantly improved drop-hammer impact resilience. As a result, the scale effects of 0.75% and 1.0% steel fiber volume fraction will be studied in Parts II and III.

6. PART II – EXPERIMENTAL DESIGN AND RESULTS: PERFORMANCE EVALUATION OF STATIC BEAM TESTING

6.1 Static Load Testing – Design

6.1.1 Mixture Design

The mixture design for each mixture is found in Table 6.1. Based on the results from Part I, these mixtures were deemed the most optimal moving forward. Of the three fibers tested, steel was significantly more workable and as a result was paired with the previously determined optimal 20% tire chip coarse aggregate replacement. Because the results from the drop-hammer impact test showed a correlation between steel volume fraction and number of drops to reach ultimate failure, varying volume fractions were observed. A full mixture design matrix can be found in Appendix A.1.

Table 6.1 - Static Beam Specimen Mixture Proportions by Volume

Designation	w/cm	Cement Content, lb/yd³ (kg/m³)	% Steel Fiber (Volume Fraction)	% Tire Chip (Volume Fraction of C.A)	% Coarse Aggregate (Volume Fraction)	% Fine Aggregate (Volume Fraction)
Control	0.42	611 (362)	0	0	100	100
ST0.0-TC20	0.42	611 (362)	0	20	80	100
ST0.5-TC20	0.42	611 (362)	0.5	20	80	100
ST0.75-TC20	0.42	611 (362)	0.75	20	80	100
ST1.0-TC20	0.42	611 (362)	1.0	20	80	100

6.1.2 Static Test Setup

After the results from Part-I were reviewed, it was deemed that mixtures containing steel fibers and tire chips would be further analyzed in scaled beams of dimensions 7’ 6” length x 6” width x 10” height (2286 mm x 152.4 mm x 254mm) under static loading. In terms of steel reinforcement, rebar cages were initially constructed with 2 #3 longitudinal bars for the compression steel and 2 #4 bars for the tension steel. These bars were held together by #2 stirrups spaced every 4” on center to resist shear failure. The steel bars used in this study possessed a minimum yield strength of 60,000 psi (420 MPa) and a Young’s modulus of 29,000 ksi (200,000 MPa). After testing specimens with 2 #4 tension steel bars, other reinforcing ratios were observed for comparison. The geometry and orientation of the longitudinal bars can be seen in Figures 6-1 and 6-2. Each beam was tested at a clear span of 73 in. (1854 mm).

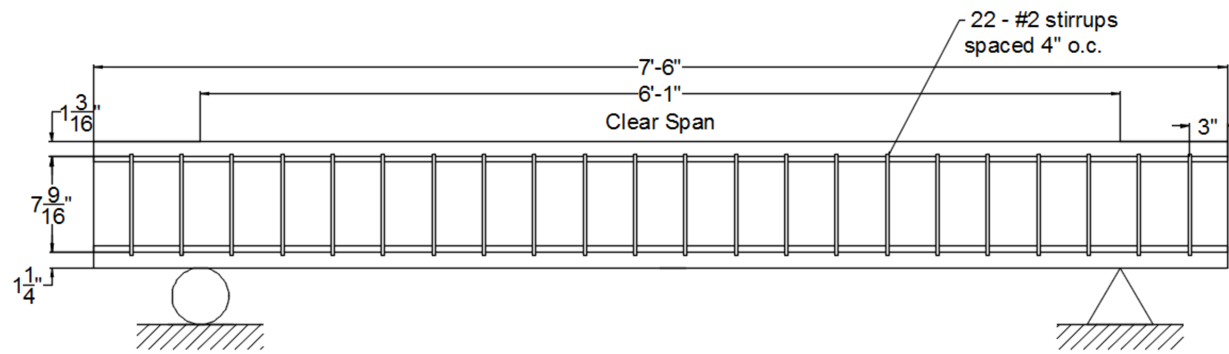

Figure 6-1. Longitudinal Section of RC Test Specimen.

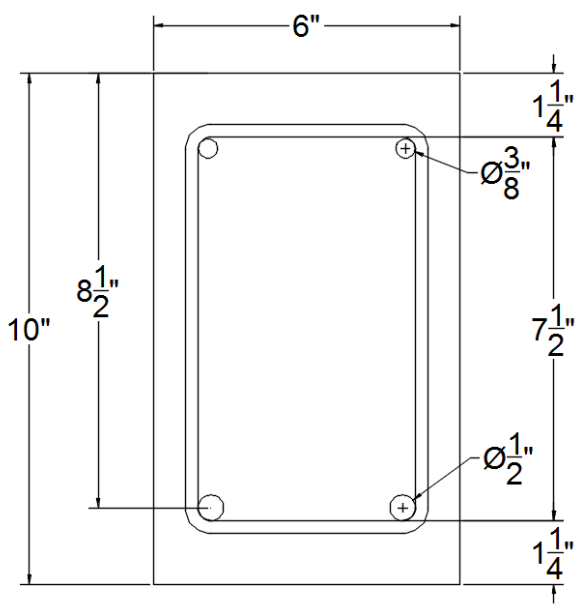

Figure 6-2. Cross Section of RC Test Specimen.

Static load testing was conducted using a 220 kip (978.6kN) capacity hydraulic actuator with the load being distributed by a 6 in. wide (152 mm) steel plate. Specimens were tested at mid-span under an increasing load at rate of 200 lbs (890 N) per second, taking note how the cracks developed over time. A load cell, which was placed at mid-span directly underneath the actuator arm, and a research grade NDI Optotrak Certus HD motion capture were used to measure applied load and displacement. The location of the motion capture sensors are seen in Figure 6-3. The load cell, motion capture camera, and actuator are pictured in Figures 6-4 and 6-5, respectively.

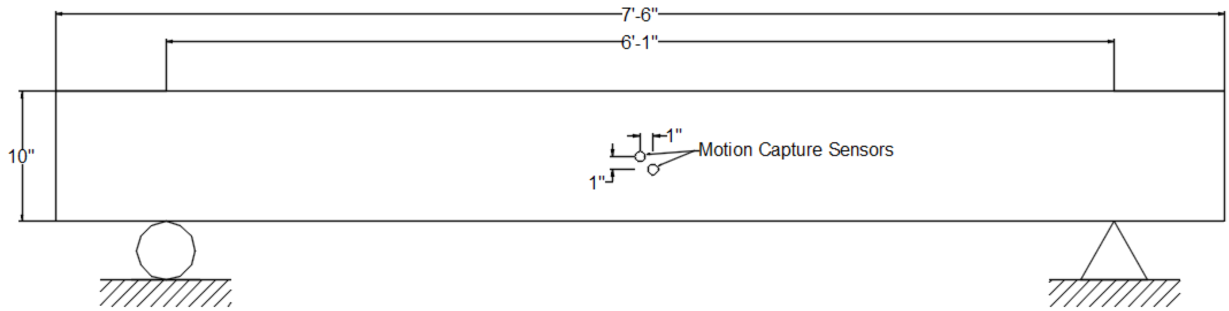

Figure 6-3. Location of Motion Capture Sensors

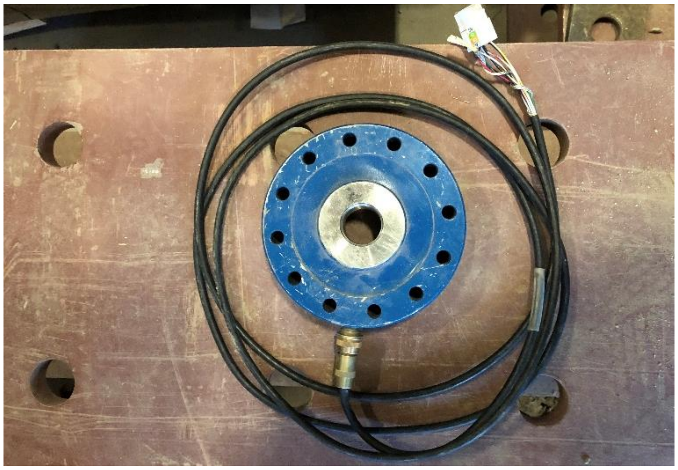

Figure 6-4. Load Cell Used for Static Testing.

Figure 6-5. Actuator Arm (Left) and Motion Capture Camera (Right)

A data acquisition system was used to process the data from the motion capture camera. The frequency was set to 20 Hz to match the rate of the load cell data acquisition. It was imperative to match these frequency to accurately develop load-deflection plots.

6.1.3 Steel Reinforcement Ratio

The fiber reinforced concrete (FRC) beams were tested at varying tensile steel reinforcement ratios. The purpose of this was to grasp a better understanding on how reinforcement ratio affects the total energy dissipation of the FRC beams. Specimens were tested with tension steel reinforcement values of 0.196%, 0.78%, and 1.17%. To achieve these reinforcement ratios, specimens were comprised of two #2, two #4, and three #4 tension steel bars, respectively.

6.1.4 Fresh Concrete Properties

Similar to Part I, fresh concrete properties were tested for the following specimens. Overall, there seemed to be less variance than mixtures in Part I, most likely due to the same type of fiber and tire chip content being used for each Part II mixtures. These fresh concrete properties are found in Table 6.2.

Table 6.2 - Fresh Concrete Properties for Static Beam Mixtures.

Mixture Description	Slump, in (mm)	Temperature, F° (C°)	Unit Weight, lb/ft³ (kg/m³)	Air Content, %
Control (ρ = 0.78%)	3.5	86	146.4	5.0
ST0.0-TC20 (ρ = 0.78%)	2.25	86	137.4	4.5
ST0.75-TC20 (ρ = 0.196%)	0.5	63.3	141.8	4.6
ST1.0-TC20 (ρ = 0.78%)	0.5	87	140.2	2.2
ST0.5-TC20 (ρ = 0.78%)	0.75	59.7	142.6	3.8
ST0.75-TC20 (ρ = 0.78%)	1	68	141.4	4.2
ST0.75-TC20 (ρ = 1.17%)	1.5	64.2	141.7	4.4
ST1.0-TC20 (ρ = 1.17%)	0.5	61.9	143.4	3.6

6.1.4.1 Slump

Similar to the specimens that were tested at the latter half of Part I, the slump was recorded prior to the addition of steel fibers. The slumps ranged from 0.5 in. (12.7 mm) to 3.5 in. (89 mm) as seen in Figure 6-6. As expected, the control mixture exhibited the greatest slump. Due to the larger scale of concrete that was produced (when compared to the Part I mixtures), the admixture dosages, specifically the HRWRA and VMA, had to be readjusted. It was found that using the same admixture dosages as were used in Part-I, the concrete experienced significant segregation, causing those initial trial mixtures to be scrapped. As a result, the dosages were reduced from 7 fl oz./cwt of HRWRA and 8 fl oz./cwt of VMA to 5 and 6 fl oz./cwt, respectively, per mixture.

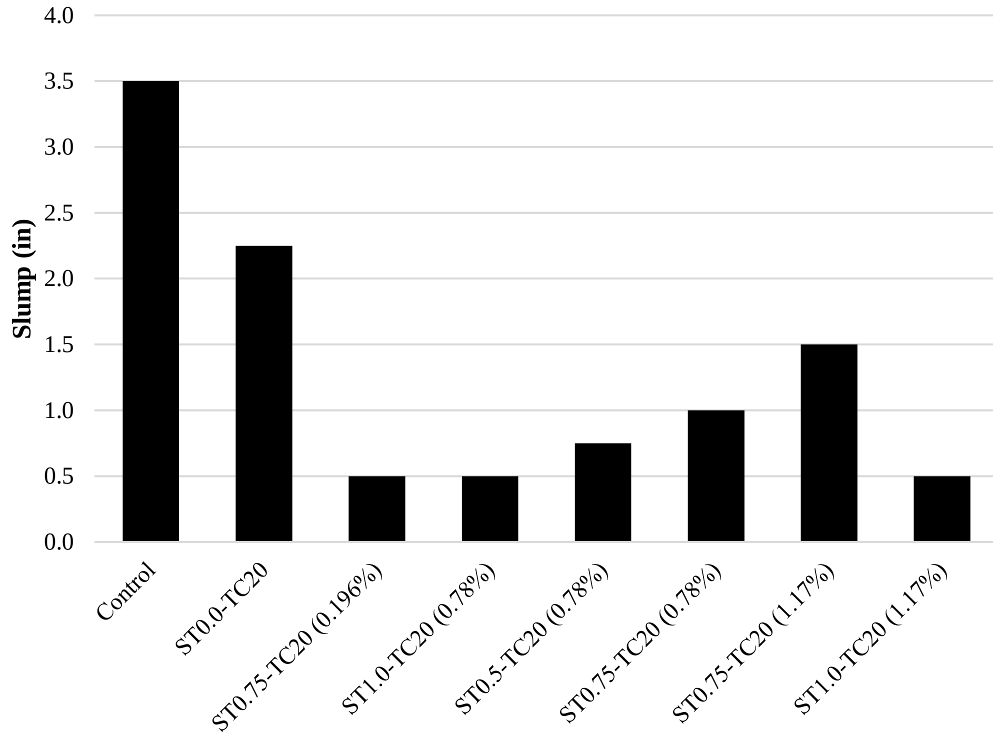

Figure 6-6. Slump Results for Static Beam Specimens.

6.1.4.2 Unit Weight

The resulting unit weights were mostly as expected, with the exception a couple of mixtures. While all mixtures with steel fiber inclusion exhibited very similar unit weights, ST1.0-TC20 (0.78%) appears too low and ST0.5-TC20 (0.78%) appears too high. Barring those two exceptions, the ST0.75-TC20 and the ST1.0-TC20 produced an average reduction in unit weight of 3.3% and 2.0%, respectively, when compared to the control mixture. Similarly, the mixture containing only tire chips, ST0.0-TC20, experienced a 6.1% reduction in unit weight. These results for unit weight are shown in Figure 6-7.

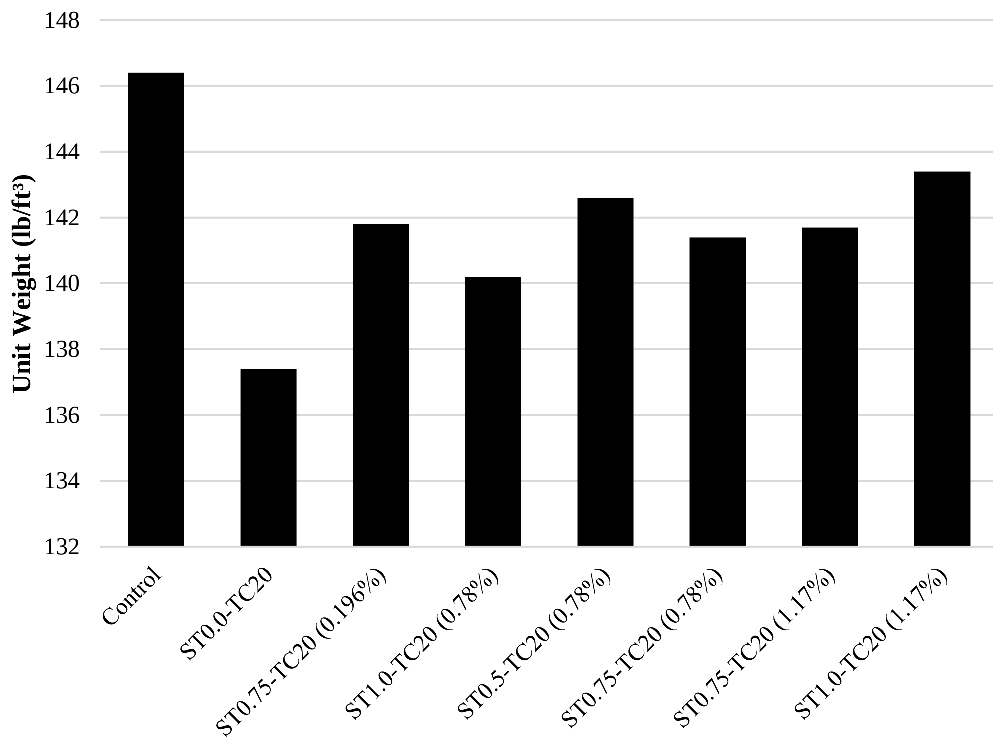

Figure 6-7. Unit Weight Results for Static Beam Specimens.

6.1.4.3 Air Content

The air content for each mixture was very stable across all mixtures, with only one exception. Excluding ST1.0-TC20 (0.78%), all mixtures met the required 2.5% to 6% parameters for GDOT Class A concrete. The air content for all Part II mixtures can be seen in Figure 6-8. The same dosage of AEA (1.3 fl oz./cwt) was used for all Part II mixtures as the Part I mixtures. This AEA dosage was the only dosage of any chemical admixture that was used to remain constant throughout the entire study.

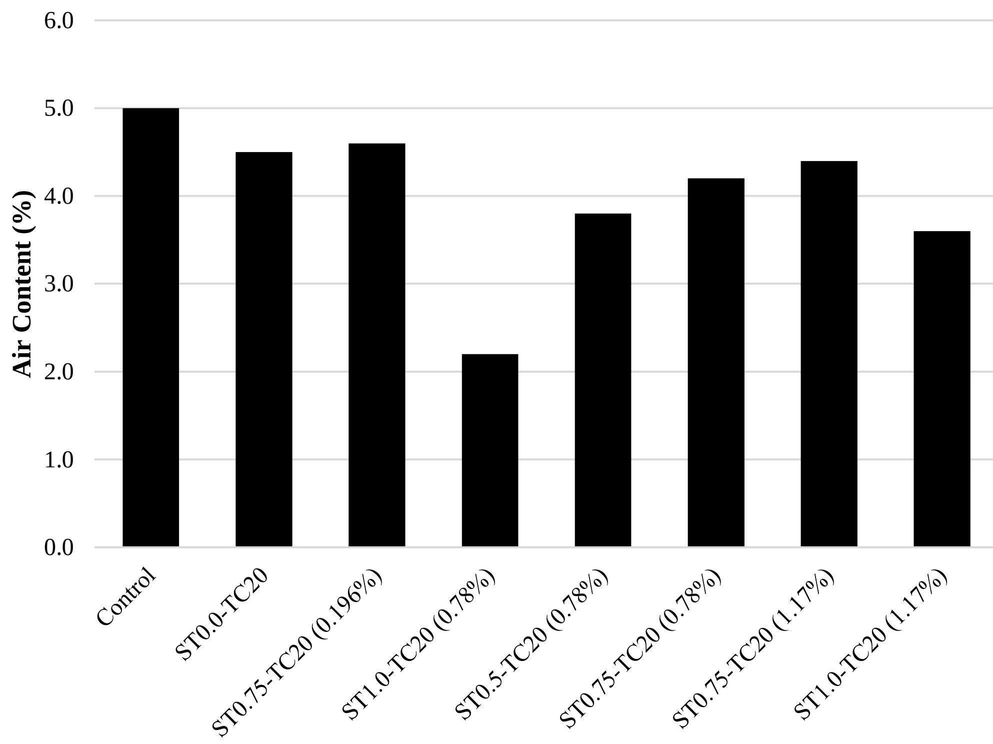

Figure 6-8. Air Content Results for Static Beam Specimens.

6.1.4.4 Placement Temperature

Unlike the specimens tested in Part I, the majority of specimens in Part II were batched within the ideal 50 to 85° F (10 to 18° C). There was a noticeable difference in concrete setting time between the mixtures that were batched in hotter temperatures than those batched in ideal temperatures. Concrete batched in ideal temperatures retained more moisture and remained workable for a longer period of time. Placement temperature for static beam specimens can be seen in Figure 6-9.

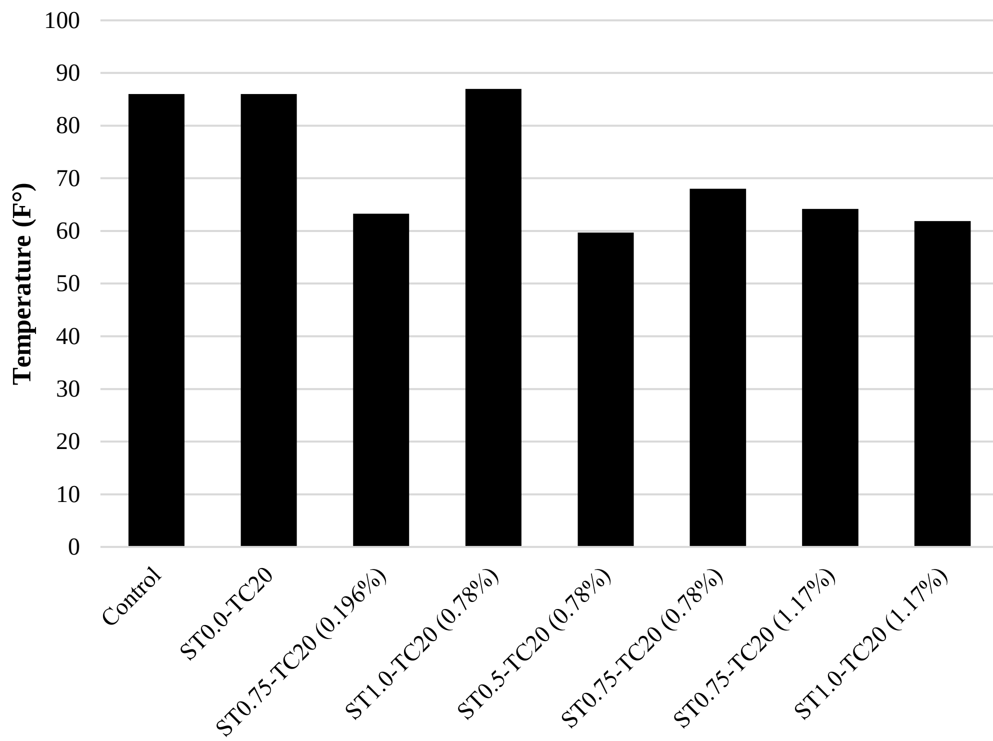

Figure 6-9. Placement Temperature Results for Static Beam Specimens.

6.1.5 Hardened Concrete Properties

6.1.5.1 Average 28-Day Compressive Strength of Cylinders

In order to produce a more accurate comparison between all Part II mixtures, cylinders (4 in. x 8 in.) were created from the same batch used to cast the FRC beams. Because the FRC beams were mixed in two separate batches, three cylinders were produced per batch, resulting in six cylinders. The compressive strength of all mixtures ranged from 3502 psi (24.1 MPa) to 5103 psi (35.2 MPa) as seen in Table 6.3.

Table 6.3 - Average 28-Day Compressive Strength of FRC Cylinders.

Mixture Description	Compressive Strength, psi (MPa)
Control (ρ = 0.78%)	5102 (35.2)
ST0.0-TC20 (ρ = 0.78%)	3596 (24.8)
ST0.75-TC20 (ρ = 0.196%)	4003 (27.6)
ST1.0-TC20 (ρ = 0.78%)	3511 (24.2)
ST0.5-TC20 (ρ = 0.78%)	4114 (28.4)
ST0.75-TC20 (ρ = 0.78%)	3878 (26.7)
ST0.75-TC20 (ρ = 1.17%)	4255 (29.3)
ST1.0-TC20 (ρ = 1.17%)	4290 (29.6)

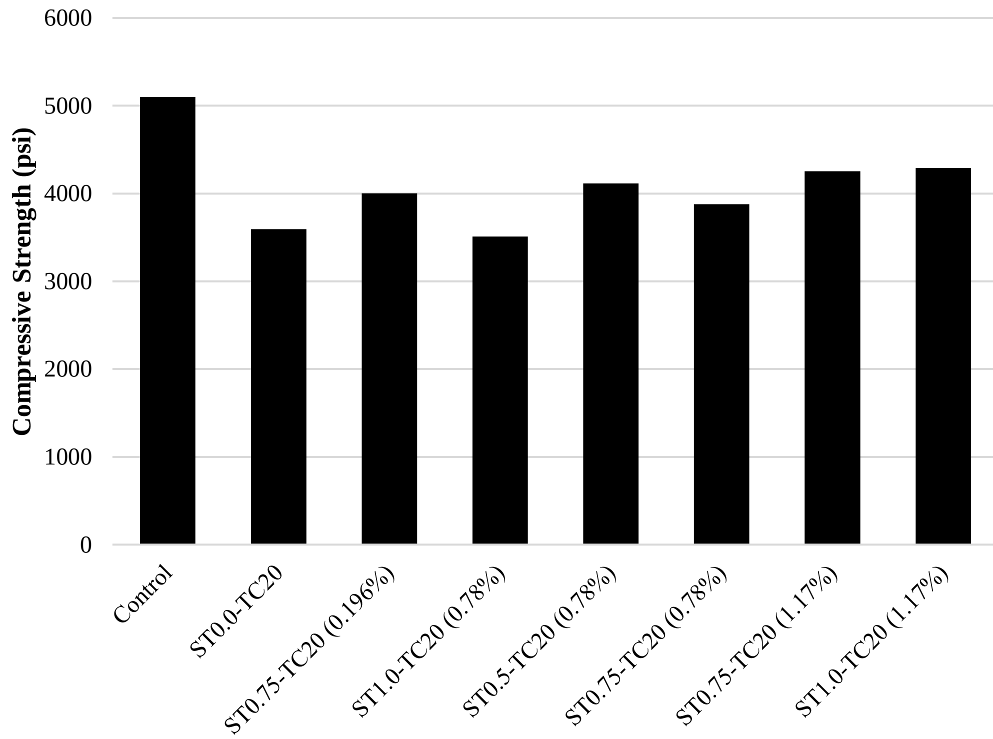

Figure 6-10. Average 28- Day Compressive Strength Results for Static Beam Specimens.

Compressive strength is an important characteristic of the FRC beams is primarily due to the failure mode of the beam itself. If the compressive strength of the concrete is low, the FRC beam will most likely experience crushing/compressive failure before the tension steel reaches ultimate tensile failure. This would mean that both the reinforcing tensile steel and steel fibers failed to achieve their maximum energy dissipation potential.

6.2 Static Load Testing – Experimental Results

6.2.1 Static Load-Deflection

The ultimate goal of this test was to determine the total energy dissipated by each FRC beam mixture. The toughness, or energy dissipation capacity, of each FRC beam was determined by integrating the function between load and mid-span deflection over the testing period from the initial to final deflection at failure. Eight FRC beams were tested under three-point bending to study the effects of fiber volume fraction, varying reinforcement ratios, and tire chips subjected to static loading conditions.

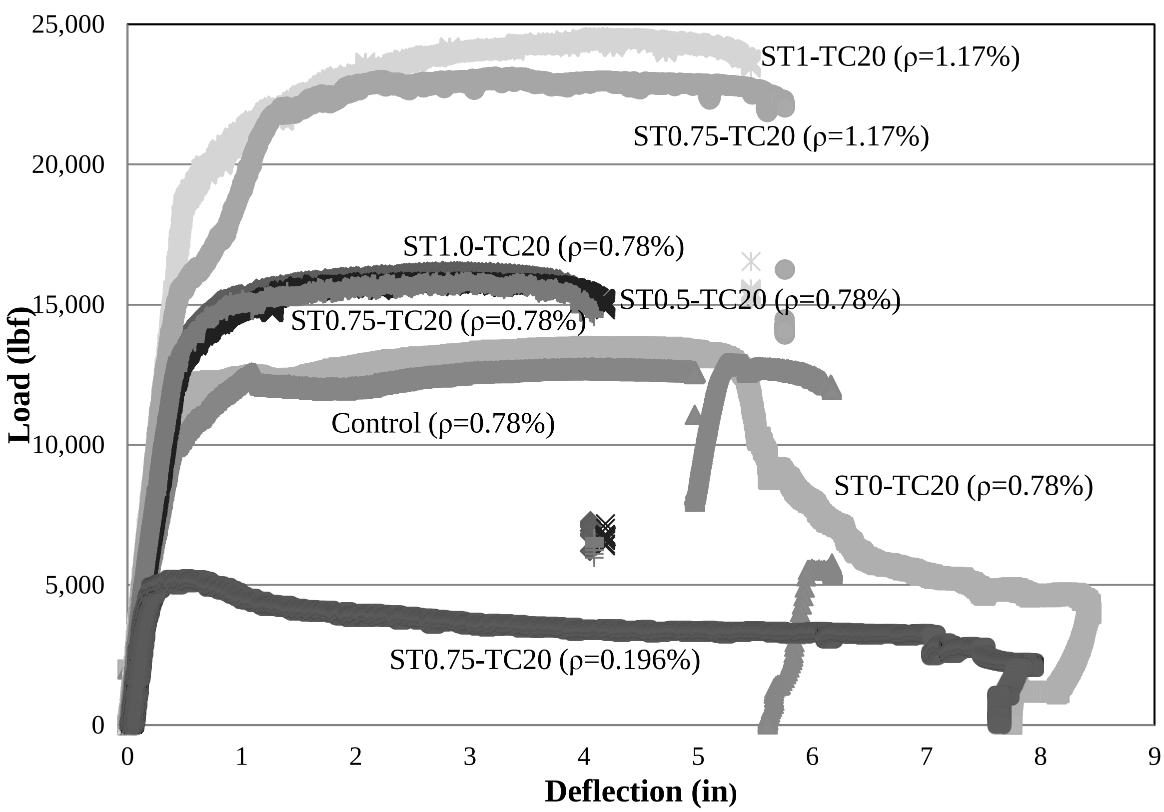

Figure 6-11. Load-Deflection Plot for Static Beam Specimens.

Except for ST0.75-TC20 (ρ=0.196%), the Control specimen withstood the least amount of load of any of the eight beams tested. Its load capacity, coupled with total deflection, resulted in the Control mixture exhibiting the lowest toughness at 57.7 kip-in (6821 KN-mm). By contrast, ST0.75-TC20 (1.17%) produced the largest static energy dissipation at 120.6 kip-in (13,627 KN-mm), a 109% increase. All toughness values are tabulated in Table 6.4. In this table, ρ is calculated by A_s/bd, where A_s is the area of flexural reinforcing steel, b is the beam width, and d is the depth measured from the top surface of the beam to the centroid of steel. The linear stiffness of each beam was also calculated. This value was taken as the initial slope of load-deflection curves for each specimen.

Table 6.4 - Total Static Energy Dissipation of FRC Beams.

Mixture Description	Toughness, kip-in (KN-mm)	Linear Stiffness, lb/in (N/m)
Control (ρ = 0.78%)	57.7 (6821)	38,159 (6,682,665)
ST0.0-TC20 (ρ = 0.78%)	64.7 (7307)	32,349 (5,665,178)
ST0.75-TC20 (ρ = 0.196%)	27.6 (3123)	32,937 (5,768,153)
ST1.0-TC20 (ρ = 0.78%)	59.2 (6693)	35,087 (6,144,675)
ST0.5-TC20 (ρ = 0.78%)	60.1 (6789)	32,700 (5,726,648)
ST0.75-TC20 (ρ = 0.78%)	58.6 (6626)	35,784 (6,266,739)
ST0.75-TC20 (ρ = 1.17%)	120.6 (13,627)	39,876 (6,983,358)
ST1.0-TC20 (ρ = 1.17%)	119.16 (13,463)	41,527 (7,272,492)

When comparing specimens within each reinforcement ratio group, tire chips alone (ST0.0-TC20 (ρ = 0.78%) increased toughness by 12.1%. Similarly, steel fibers and tire chips increased toughness by 1.6%, 2.6%, and 4.2% for mixtures ST0.75-TC20 (ρ = 0.78%), ST1.0-TC20 (ρ = 0.78%), and ST0.5-TC20 (ρ = 0.78%), respectively. When the reinforcement ratio was increased from 0.196% to 0.78% and 0.78% to 1.17%, the toughness doubled in both cases.

6.2.2 Static Test Observations

The failure modes for each specimen are found in Table 6.5. With the exception of ST0.0-TC20, every specimen failed in tension steel yielding and fracture.

Table 6.5 - Failure Modes of Static FRC Beams

Mixture Description	Failure Mode
Control (ρ = 0.78%)	Yielding/Fracture/Shear
ST0.0-TC20 (ρ = 0.78%)	Compression Failure
ST0.75-TC20 (ρ = 0.196%)	Compression and Flexural Failure
ST1.0-TC20 (ρ = 0.78%)	Yielding/Fracture
ST0.5-TC20 (ρ = 0.78%)	Yielding/Fracture
ST0.75-TC20 (ρ = 0.78%)	Yielding/ Fracture
ST0.75-TC20 (ρ = 1.17%)	Yielding/Fracture
ST1.0-TC20 (ρ = 1.17%)	Yielding/Fracture

A) Control (ρ = 0.78%)

B) ST0.0-TC20 (ρ = 0.78%)

C) ST0.75-TC20 (ρ = 0.196%)

D) ST1.0-TC20 (ρ = 0.78%)

E) ST0.5-TC20 (ρ = 0.78%)

F) ST0.75-TC20 (ρ = 0.78%)

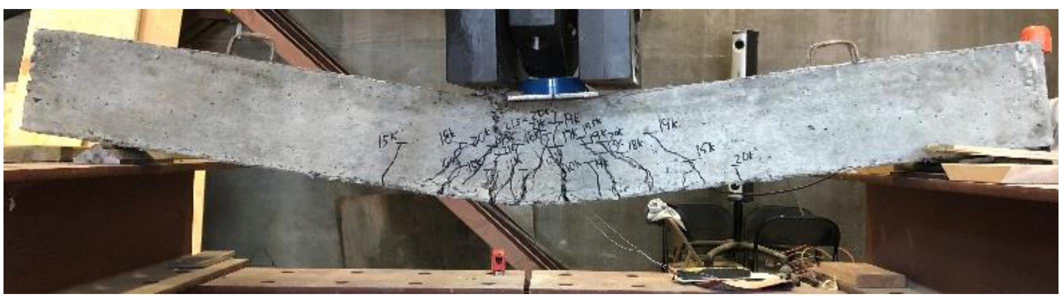

G) ST0.75-TC20 (ρ = 1.17%)

H) ST1.0-TC20 (ρ = 1.17%)

Figure 6-12. Failure Modes of Static Beam Test Specimens.

Figure 6-12 presents the cracking profiles of each specimen. Observations were made with each beam during and after testing. These observations are summarized below.

A) Control (ρ = 0.78%)

Flexural cracks began to develop at around 4 kips (17.8 kN). Originating from the base of the mid-span, these cracks propagated towards the source of the load, in some cases at approximately 45-degree angles. Cracking was also observed further from the mid-span at 9 kips (40 kN), however these cracks were more vertical and did not seem to form towards the source of the load at mid-span. Failure was observed at approximately 13 kips, initially with the yielding of the tension steel, followed by a formation of shear cracks at mid-span.

B) ST0.0-TC20 (ρ = 0.78%)

Prominent signs of flexural cracking were observed at approximately 6 kips (26.7 kN). Similar to the Control beam, cracks originated from the mid-span and spread towards the source of the load. As the deflection continued to increase, ST0.0-TC20 showed significantly more ductility than the Control. The beam appeared to deform more smoothly, resembling prominent material characteristics of rubber. Ultimately, the beam failed because of compressive failure, crushing at the contact surface of the beam at mid-span. It was not surprising to observe compressive failure based on the reduction of compressive strength that tire chips produce, especially without any fiber reinforcement.

C) ST0.75-TC20 (ρ = 0.196%)

As the beam with the smallest reinforcement ratio, it was expected that ST0.75-TC20 (0.196%) would exhibit the least load capacity than the rest of the beams. Crack propagation began at 3 kips (13.4 kN) from the center base of the beam to the top. Unlike the rest of the beams, only two prominent cracks that were worth noting. The tension steel was comprised of two #2 bars and began to yield at a much quicker rate, causing the concrete to crack quicker and prevent the steel fibers from redistributing the load at their full potential. As a result, the beam experienced bending primarily at the center crack, which can be seen in Figure 6-12. However, due to the low load capacity of the beam, the tension steel never fully yielded, resulting in fracture. Being exposed to a prolonged load of such magnitude, the tension steel continued to bend, which caused to beam to experience a significant deflection of 7.9 in (25.4 mm). Ultimately, the beam failed as a result of compression failure at the load bearing point. The significant deflection of the beam produced substantial compressive stresses on contact surface of the beam.

D) ST1.0-TC20 (ρ = 0.78%)

Crack development did not occur until approximately 13 kips, the same load in which the Control beam experienced ultimate failure. Although the compressive strength of ST1.0-TC20 (0.78%) was the lower than that of ST0.0-TC20, it did not experience the same compressive failure. The steel fibers were able to redistributed the load and bridge together the cracks that otherwise could have led to crushing at the contact surface. However, the tension steel did not fully yield, resulting in premature fracture. It is concluded that fiber reinforced beams can significantly increase flexural and shear capacity and thus, exhibit a failure mode unlike with conventional concrete beams.

E) ST0.5-TC20 (ρ = 0.78%)

Initial signs of cracking appeared at 7 kips (31.1 kN). ST0.5-TC20 (0.78%) exhibited a 1.5% increase in static energy dissipation compared to ST1.0-TC20 (0.78%), even though it had a slightly lower load capacity. Although the static energy dissipation between 0.5% and 1.0% steel volume fractions appear to be almost identical, it should be noted that at 1.0% ST1.0-TC20

(0.78%) did not experience any significant initial cracking until 13 kips, almost twice the capacity at 0.5%.

F) ST0.75-TC20 (ρ = 0.78%)

Similar to ST0.5-TC20 (0.78%), ST0.75-TC20 (0.78%) experienced initial cracking at 7 kips (31.1 kN). Vertical cracks developed similar to that of the 0.5% and 1.0% volume fractions at ρ = 0.78%. The beam failed almost identically to the other two and produced a load-deflection curve that is bounded by ST1.0-TC20 (0.78%) and ST0.5-TC20 (0.78%), as seen in Figure 6-10. Compared to the control, ST0.75-TC20 (0.78%) produced a 1.6% increase in static energy dissipation compared to the Control, the smallest gain of the ρ = 0.78% mixtures. However, all three ρ = 0.78% mixtures were within 2.6% of one another, which is overall an insignificant difference in toughness.

G) ST0.75-TC20 (ρ = 01.17%)

Due to undergoing a larger load over a longer period of time, more cracks were observed at 1.17% reinforcement ratio compared to 0.78%. Early signs of cracking began to appear on ST0.75-TC20 (1.17%) at approximately 10 kips (44.48 kN). When compared to 0.5% (initial cracking at 7 kips) and 1.0% (initial cracking at 13 kips) steel volume fractions, the load in which each beam experienced initial crack propagation demonstrates a linear correlation with steel volume fraction. In the case of static energy dissipation, ST0.75-TC20 (1.17%) produced a 1.2% increase compared to the Control.

H) ST1.0-TC20 (ρ = 1.17%)

Similar to ST1.0-TC20 (0.78%), initial cracking developed at approximately 12 kips. The beam reacted very similarly to ST0.75-TC20 (1.17%) in that the steel fibers effectively redistributed the load. This was apparent when the load would seemingly peak only to continue increasing after a period of time. In the case of total static energy dissipation, ST1.0-TC20 (1.17%) demonstrated a 1.2% decrease in toughness when compared to ST0.75-TC20 (1.17%). It was ultimately concluded from these specimens that while the reinforcement ratio increases load capacity and maximum deflection, steel fiber volume fraction increases initial cracking response and load distribution.

6.2.3 Summary of Static Test Results

The eight rubberized FRC beams tested demonstrated consistent results. Testing was limited to these eight beams as it became very clear how each beam would perform relative to one another. It is important to note that increasing steel volume fraction resulted in a slight increase in load capacity, but a slight decrease in deflection, resulting in similar net static energy dissipation. As a result, the effects of 0.5%, 0.75%, and 1.0% steel fiber volume fraction were inconsequential to toughness for these mixtures. However, when steel fibers are provided, the flexural and shear capacities of the beams increase. Therefore, for FRC beams, it is necessary to increase the number of flexural reinforcing bars in order to see the full potential of the fibers without experiencing premature failure. In this case, adding an extra 50% of tensile steel reinforcement resulted in an increase in toughness by a factor of two because the steel fibers were allowed to dissipate energy at a greater capacity.

7. PART III – EXPERIMENTAL DESIGN AND RESULTS: PERFORMANCE EVALUATION OF IMPACT BEAM TESTING

7.1 Impact Load Testing – Design

7.1.1 Mixture Design

The results from the drop-hammer impact tests from Part I and the static load tests from Part II led to the mixture design matrix found in Table 6.7. From the drop-hammer impact tests, it was determined that only steel fiber volume fractions of 0.75% and 1.0% produced significant impact resilience, the former of which yielding a 3525% increase in performance. Although the conclusions drawn from the static load tests led to an optimized 0.5% steel fiber volume fraction mixture, the drop-hammer impact test suggested this fiber content was insufficient at redistributing impact loads. Furthermore, it was concluded that the reinforcement ratios of 1.17% and 0.78% are reasonable for specimens with and without fiber reinforcement, respectively. The full mixture design matrix can be seen in Appendix A.1.

Table 7.1 – Impact Beam Specimens Mixture Proportions by Volume

Designation	w/cm	Cement Content, lb/yd^3 (kg/m^3)	% Steel Fiber (Volume Fraction)	% Tire Chip (Volume Fraction of C.A)	% Coarse Aggregate (Volume Fraction)	% Fine Aggregate (Volume Fraction)
Control	0.42	611 (362)	0	0	100	100
ST0.0-TC20	0.42	611 (362)	0	20	80	100
ST0.75-TC20	0.42	611 (362)	0.75	20	80	100
ST1.0-TC20	0.42	611 (362)	1.0	20	80	100
ST1.0-TC0	0.42	611 (362)	1.0	0	100	100
ST0.75-TC0	0.42	611 (362)	0.75	0	100	100

7.1.2 Impact Test Setup

The impact beam testing setting up can be seen in Figure 7-1. These beams were designed in the same manner as the static beams in Chapter 6 (see Figures 6-1, 6-2, and 6-3).

Figure 7-1. Anterior View of Impact Beam Setup.

A roller was used to allow for rotational movement at the supports; however, the uplift force was restricted by using two ½ in. thick sheets of insulation in between the beam and 2 in. x 6 in. (60 mm x 152.4 mm) planks of lumber on the top surface. These wooden planks were restrained by 1 in. (25.4 mm) threaded rods and secured by bolts. The threaded rods were also secured to the steel frame, which was imbedded into the concrete strong floor to transfer the reaction forces.

Figure 7-2. Side View of Impact Beam Setup.

The beam was placed in the center point a 20 ft vertical sleeve that would be used to guide a 400 lb steel drop-weight, ensuring a direct impact on the beam at the center of the contact surface. The cross sectional area of the vertical sleeve is 1ft x 1ft.

Figure 7-3. Elevation View of 20ft Vertical Sleeve Used to Guide Drop-Weight.

7.1.3 Impact Testing Procedure

Prior to testing, the drop weight was attached to a release mechanism that can be activated by pulling a lever. Although the release mechanism never experienced involuntary releasing of the drop weight, a steel safety chain was also attached to the drop weight as a preventative measure. The drop weight was oriented at the centroid of the vertical sleeve cross section using a crane and held in that position until prior testing. The drop-weight consisted of multiple components of smaller weights that can altered according to the desired weight. A schematic of the drop weight is seen in Figure 7-5.

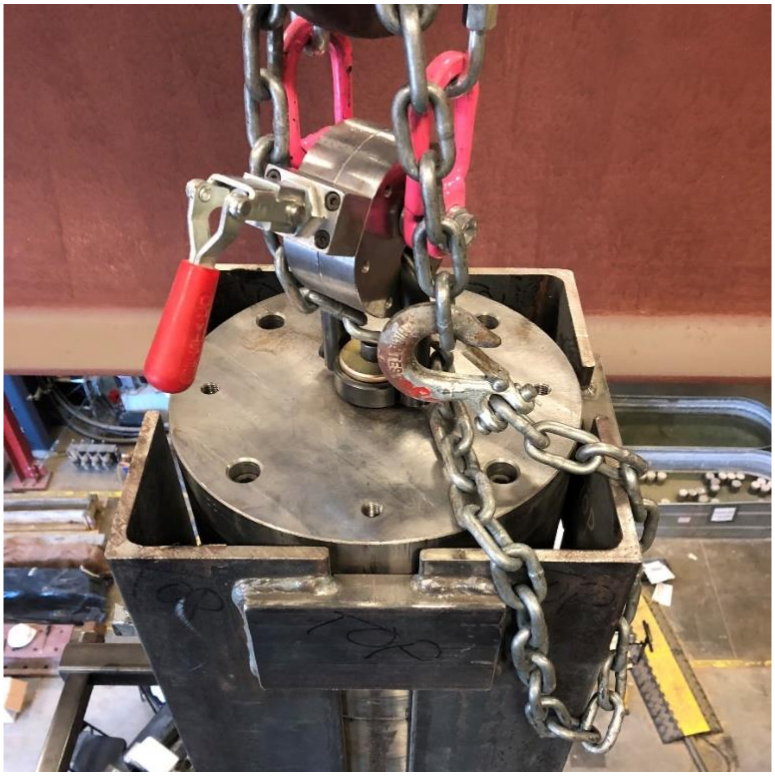

Figure 7-4. Drop-Weight Set Up and Orientation.

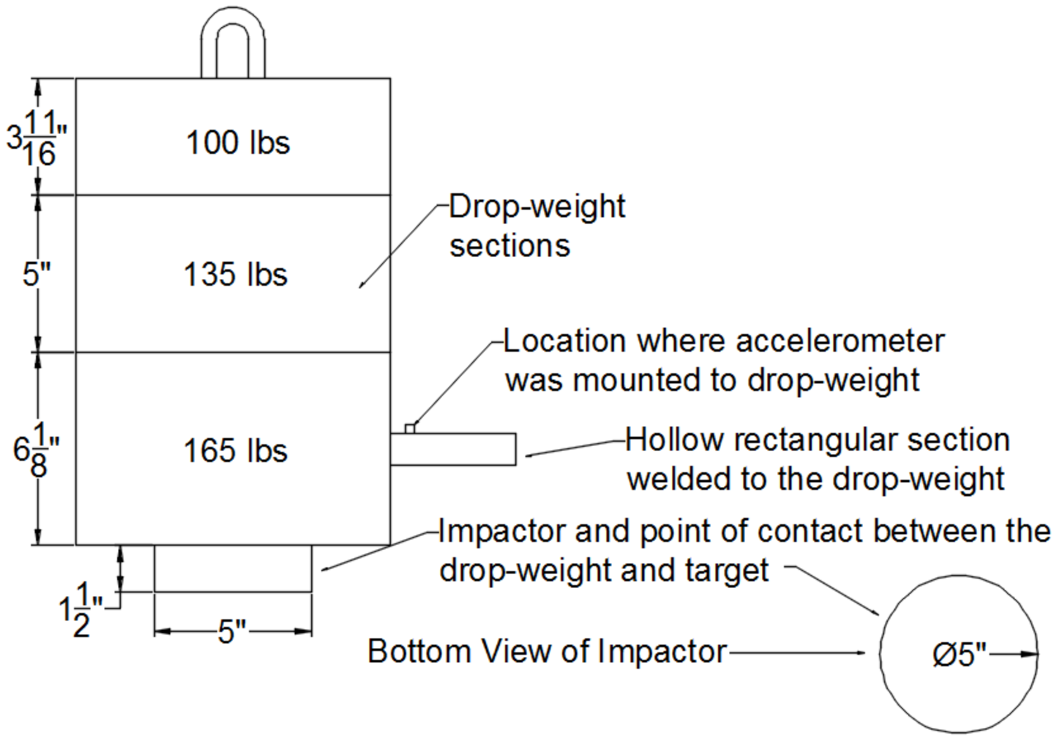

Figure 7-5. Schematic of Drop-Weight and Accelerometer Placement Location.

An accelerometer was attached to the drop-weight arm (See Figure 7-5), to capture vibrations experienced by the drop weight that would subsequently be converted into impact force. The accelerometer, which possesses a measurement range of ± 5000g pk (± 160,870 ft/s^2 or 49000 m/s^2), was set to a sampling rate of 20,000 Hz. The accelerometer was used as a supplement to a load cell in an effort to ensure the peak impact force was accurately recorded.

The load cell was placed underneath the pinned support and two ½ in. steel plates. The load was distributed through these plates and a 7 in. diameter bearing plate to the center of the load cell contact surface. A sampling rate of 10,000 Hz was deemed reasonable for the load cell data acquisition because it balanced the limitations of the load cell with the need to capture the peak impact load. Unlike the accelerometer, the load cell captures the reactionary force of the beam itself, theoretically leading to potentially more valid data.

Figure 7-6. Load Cell Top (Left) and Side (Right) View Used for Impact Testing.

Deflection at the mid-span of the beam was also taken into account. The same NDI Optotrak Certus HD motion capture camera previously used for static testing was also used for impact testing purposes. Similar to static load tests, two markers were glued at the center of the beam in the same orientation as was the case in static beam testing. The motion capture camera was set to record at 400 Hz per marker to fully measure the displacement-time history.

7.1.4 Steel Reinforcement Ratio

Results from static testing shed light on the effects of varying steel reinforcement ratios in conjunction with steel fibers. In the case of specimens consisting ρ values of 0.78% and 1.17%, nearly all specimens, barring ST0.0-TC20, failed in tension steel fracture/yielding. The specimens not containing steel fibers (i.e. Control and ST0.0-TC20) either failed in the compressive zone or was nearing compressive zone failure. On the contrary, specimens consisting of steel fibers resisted compressive zone failure as a result of the ability of the fibers to redistribute load and bridge large cracks. Thus, a ρ value of 0.78% proved to limit the maximum potential of the fibers themselves. This became evident in the load-deflection results for specimens with ρ values of 1.17% when it was noticed that these specimens exhibited twice the toughness than that of their $\rho = 0.78\%$ counterparts. Had the Control and ST0.0-TC20 mixtures been designed and tested with ρ values of 1.17%, these specimens would have experienced total compressive failure long before the tension steel yielded or fractured as result of low ductility and compressive strength, respectively. Ultimately, it was decided that for impact beam specimens, the Control and ST0.0-TC20 would be designed with ρ values of 0.78% and all other specimens that contained steel fibers would be designed with ρ values of 1.17%. The ductile behavior of these varying reinforcement ratios will be correlated by relative changes in deflection.

7.1.5 Fresh Concrete Properties

To continue consistent quality control measures, fresh concrete properties were tested and reported. A summary of the fresh concrete properties for the impact beam specimens can be seen in Table 7.2.

Table 7.2 – Fresh Concrete Properties of Impact Beam Specimens

Mixture Description	Slump, in (mm)	Temperature, F° (C°)	Unit Weight, lb/ft³ (kg/m³)	Air Content, %
Control (ρ=1.17%)	4.50	59.4	143.4	6.1
ST0.0-TC20 (ρ=1.17%)	3.0	57.9	136	5.2
ST0.75-TC20 (ρ=1.17%)	2.0	79.2	142	4.5
ST1.0-TC20 (ρ=1.17%)	2.0	79.4	144.2	4.2
ST0.75-TC0 (ρ=1.17%)	2.5	81.3	149.6	4.0
ST1.0-TC20 (ρ=1.17%)	3.0	81.5	150.4	3.6

7.1.5.1 Slump

Mixtures were tested for slump prior to steel fiber inclusion to remain consistent with specimens tested in Chapters 5 and 6. Results for slump ranged from 2 to 4.5 in. and can be seen in Figure 7-7. Similar to the static beams batched in Chapter 6, mixtures were dosed with 5 and 6 fl. oz/cwt of HRWRA and VMA, respectively. Reported slump values for impact beam specimens all met GDOT Class A requirements for slump.

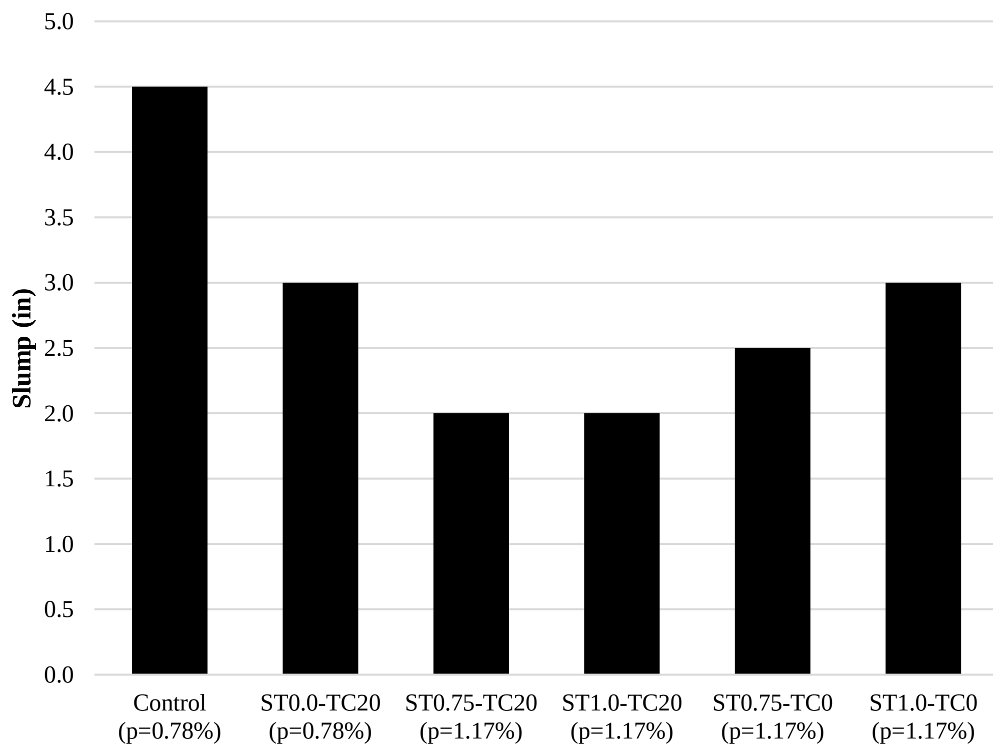

Figure 7-7. Slump Results for Impact Beam Specimens.

7.1.5.2 Unit Weight

Measured unit weight values were all consistent and in line with expectation from unit weight results previously obtained in Part-I and static test mixtures. As predicted, mixtures containing tire chips were lighter than their equivalent pairs that used 100% natural coarse aggregate. Similarly, unit weight increased as a result of increasing steel fiber volume fraction. Unit weights ranging from 136 to 150.4 lb/ft³ are presented in Figure 7-8.

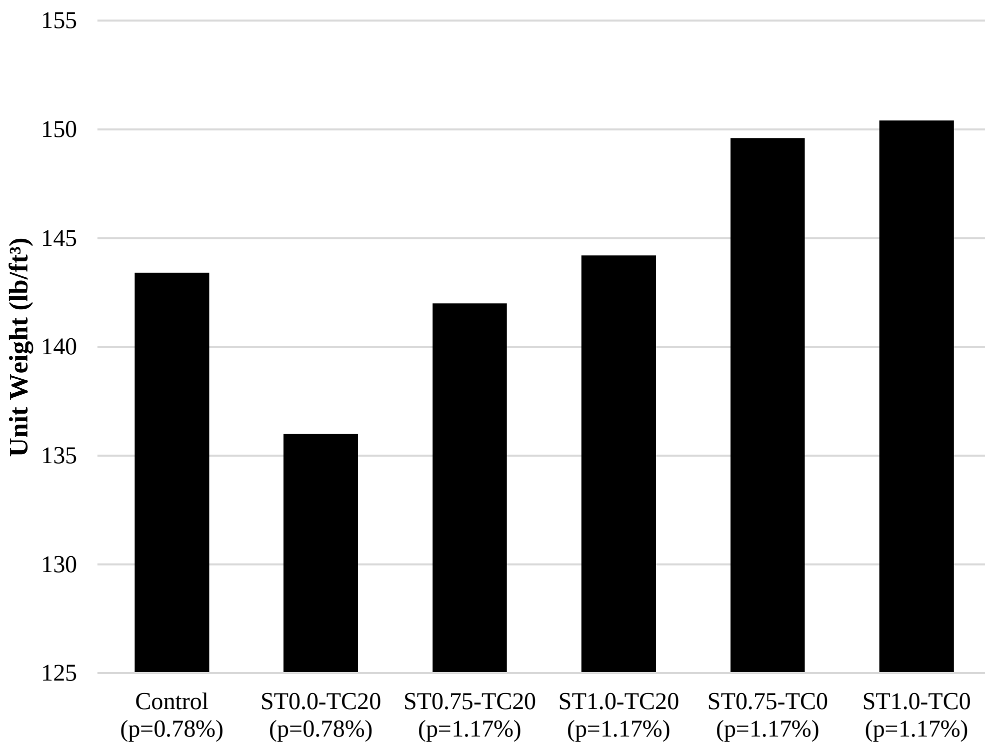

Figure 7-8. Unit Weight Results for Impact Beam Specimens.

7.1.5.3 Air Content

From Figure 7-9, it is shown that recorded air contents ranged from 3.6 to 6.1%. Interestingly, air content appears to decrease with an increase in quantity of cementitious composites. Even without fibers, ST0.0-TC20 possessed a lower air content than the Control. It was seen that increasing steel fiber volume fraction decreases air content, which was observed by a 0.3 and 0.4% decrease in air content when comparing 0.75 to 1.0% steel fiber content with tire chip inclusion and without, respectively. This trend was also experienced in Section 6.2.3 with the static beam mixtures. This result could be due to crowding of steel fibers filling voids within the concrete matrix, causing it to be more densely packed.

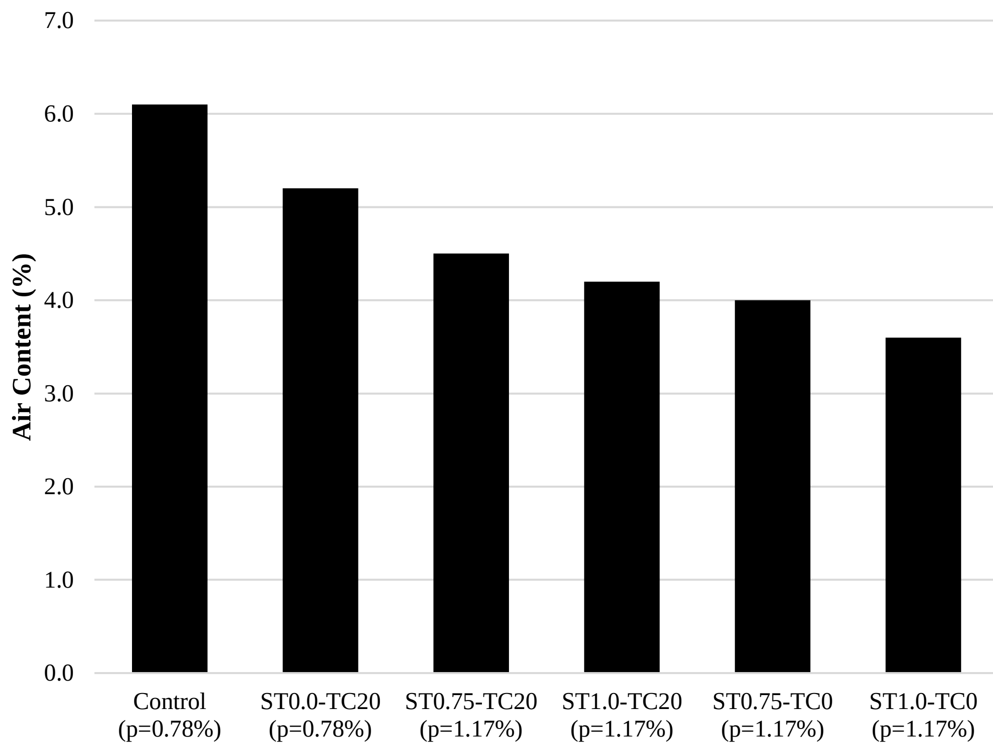

Figure 7-9. Air Content Results for Impact Beam Specimens.

7.1.5.4 Placement Temperature

Recorded placement temperatures for the impact beam specimens ranged from 57.9 to 81.5 F˚. The Control and ST0.0-TC20 mixtures were both batched in ideal temperatures, whereas the other mixtures were batched at a higher, yet still acceptable temperature. There appeared to be no evidence of decreased performance with mixtures that were batched a higher temperatures.

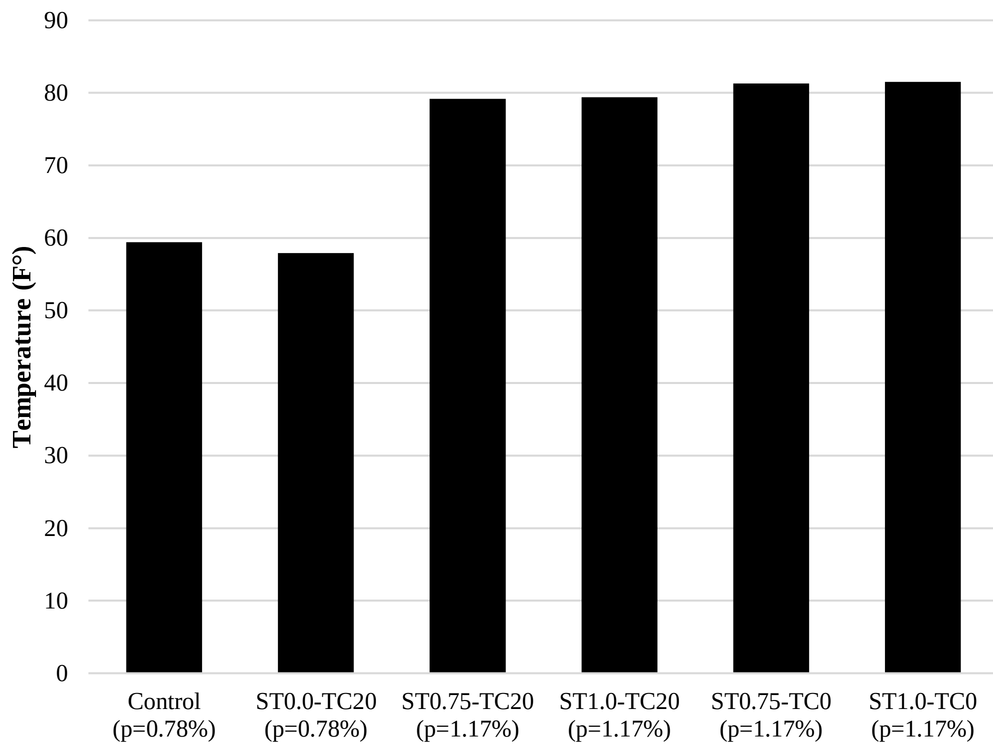

Figure 7-10. Placement Temperature Results for Impact Beam Specimens.

7.1.6 Hardened Concrete Properties

Compressive strengths for all impact beam specimens ranged from 3406 psi (ST0.0-TC20) to 7601 psi (ST0.75-TC0). Relative to the mixtures consisting of 100% volume fraction of coarse aggregate, the compressive strengths of mixtures that included tire chips decreased by 46, 48, and 37% for ST0.0-TC20, ST0.75-TC20, and ST1.0-TC20, respectively. All mixtures exceeded the minimum requirement of 3,000 psi for GDOT Class A Concrete and, with the exception of ST0.0-TC20, exceeded the minimum 3,500 psi for GDOT Class AA Concrete. These compressive strengths are observed in Table 7.3 and Figure 7-11.

Table 7.3 – Average 28-Day Compressive Strength of Impact Beam Cylinders.

Mixture Description	Compressive Strength, psi (MPa)
Control (ρ = 0.78%)	6325 (43.6)
ST0.0-TC20 (ρ = 0.78%)	3406 (23.5)
ST0.75-TC20 (ρ = 1.17%)	3926 (27.1)
ST1.0-TC20 (ρ = 1.17%)	4598 (31.7)
ST0.75-TC0 (ρ = 1.17%)	7601 (52.4)
ST1.0-TC0 (ρ = 1.17%)	7329 (50.5)

As observed in results from static beam testing, mixtures that produced lower compressive strengths were more susceptible to crushing failure at the contact surface, especially if no fiber reinforcement was present in the concrete matrix. As will be further analyzed in Sections 7.2 and 7.3, steel fibers and tire chips had the ability to keep beams intact in the compressive failure zone at the contact surface.

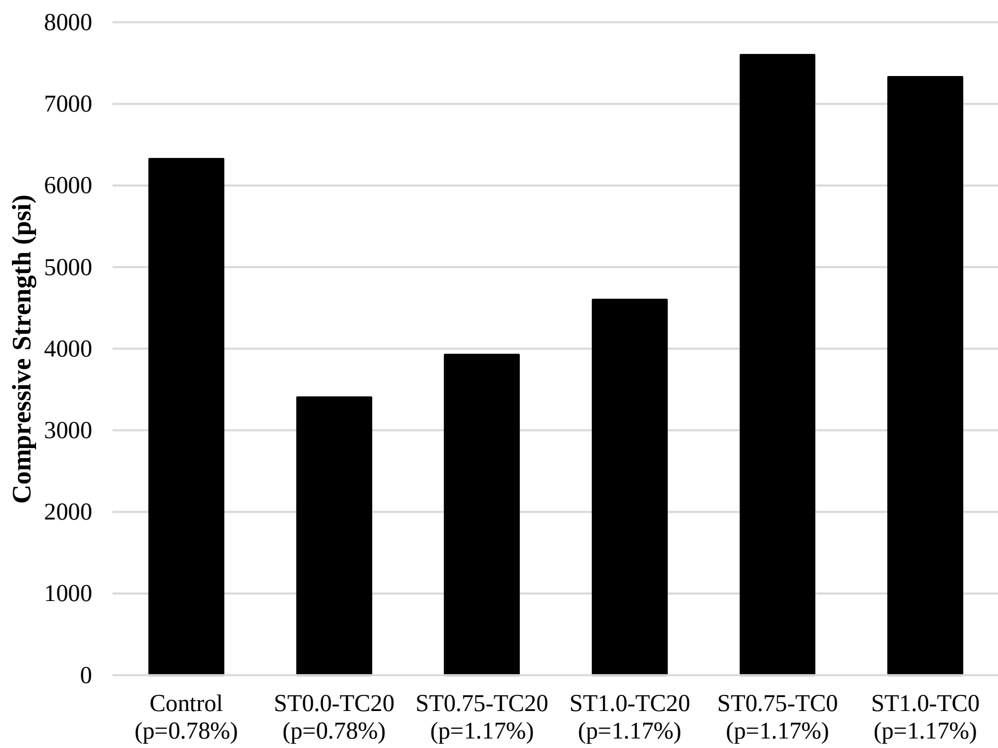

Figure 7-11. Average 28-Day Compressive Strength Results for Impact Beam Specimens.

7.2 Impact Load Testing – Experimental Results

7.2.1 Mid-Span Displacement

To observe ductility due to impact loading, the deflection at mid-span was compared between specimens. The motion capture camera used was set to record data at a rate of 400 points per second, which was sufficient in capturing the displacement behavior history from the initial point of impact until the point of rest. The displacement histories are visually represented in Figure 7-12. Although the final displacement is an indicator of ductility, the overall displacement-time history provides a clearer picture of the increase in the energy dissipated at and immediately after impact. The initial peak, which occur between approximately 20 and 30 milliseconds for all beams tested, is the initial displacement upon impact. Subsequent decreases and increases of displacement were the result of the beams rebounding from impact and then experiencing residual impact forces until the drop weight reached equilibrium.

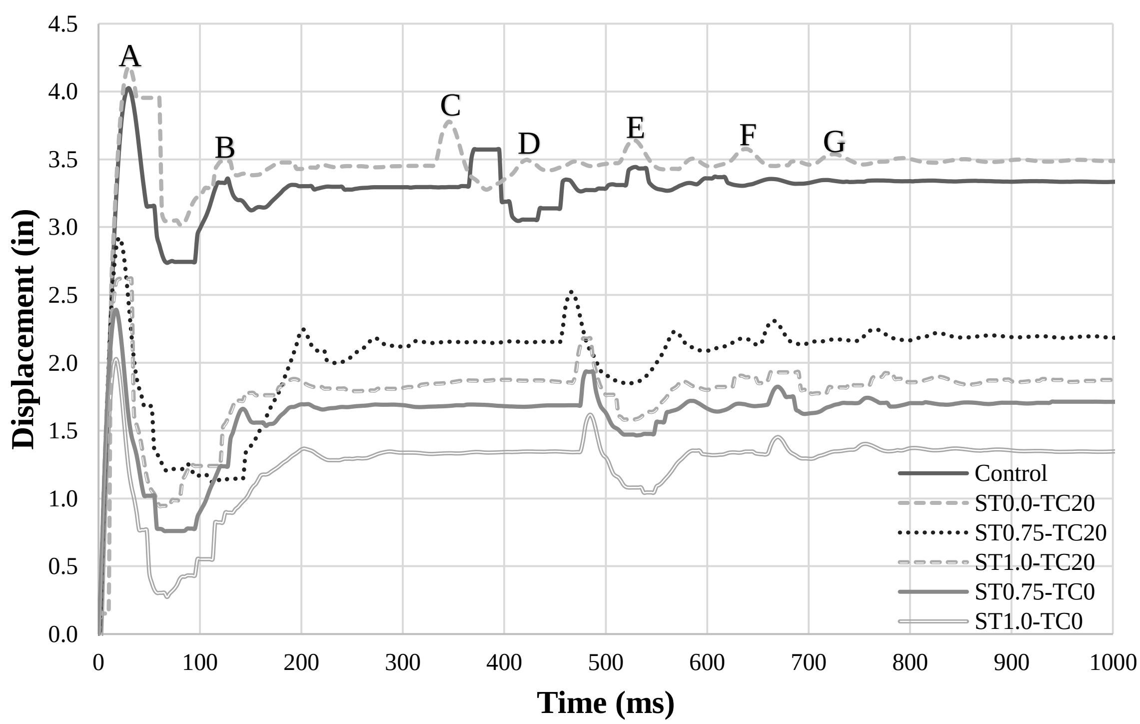

Figure 7-12. Displacement-Time History of Impact Beam Specimens.

The appropriate letters ("A" through "G") denote the locations of the corresponding displacements, which are represented as numerical values in Table 7.4. Only the lettering for ST0.0-TC20 was included in this figure as example. Similarly, subsequent figures representing displacement-time histories will only show lettering for one specimen as reference to prevent from overcrowding of letters within the figure. The figures that include the lettering for each individual specimen can be found in Appendix A.1.

Table 7.4 – Displacement Histories of Impact Beam Specimens.

	Displacement, in								**Duration**
Mixture Description	A	B	C	D	E	F	G	Final	Time, ms
Control (ρ = 0.78%)	4.02	3.36	3.57	3.34	3.43	3.37	-	3.34	780
ST0.0-TC20 (ρ = 0.78%)	4.18	3.48	3.78	3.51	3.64	3.57	3.54	3.51	998
ST0.75-TC0 (ρ = 1.17%)	2.39	1.64	1.933	1.717	1.81	1.74	-	1.71	897.5
ST0.75-TC20 (ρ= 1.17%)	2.92	2.24	2.52	2.21	2.3	2.25	-	2.19	985
ST1.0-TC0 (ρ = 1.17%)	2.03	1.37	1.62	1.35	1.45	1.4	-	1.34	950
ST1.0-TC20 (ρ = 1.17%)	2.62	1.88	2.18	1.86	1.93	1.92	1.89	1.87	1020

The data extrapolated from Table 7.4 shows an increase in displacement at every point in mixtures that included tire chips relative to the corresponding mixtures that did not. The final displacements were taken when the beams reached equilibrium. The number of points were taken from point "A" to the final displacement and was converted to milliseconds. Because it would not be valid to directly compare displacements between mixtures with steel reinforcement ratios of 0.78 and 1.17%, the change in displacement at each point relative to the final displacement was determined per beam. These adjusted displacements can be seen in Table 7.5.

Table 7.5 – Change in Displacement Relative to Final Displacement

	Change in Displacement Relative to Final Displacement, in						
Mixture Description	A	B	C	D	E	F	G
Control (ρ=0.78%)	0.68	0.02	0.23	0.00	0.09	0.03	-
ST0.0-TC20 (ρ=0.78%)	0.67	-0.03	0.27	0.00	0.13	0.06	0.03
ST0.75-TC0 (ρ=1.17%)	0.68	-0.07	0.22	0.01	0.10	0.03	-
ST0.75-TC20 (ρ=1.17%)	0.73	0.05	0.33	0.02	0.11	0.06	0.03
ST1.0-TC0 (ρ=1.17%)	0.69	0.03	0.28	0.01	0.11	0.06	-
ST1.0-TC20 (ρ=1.17%)	0.75	0.01	0.31	-0.01	0.06	0.05	0.02

Instances in which relative displacements peak, specifically at points “A”, “C”, and “E”, correspond to the points in which the beam experienced first, second, and third impact (this is further observed in the analysis section). Barring a few exceptions, mixtures containing tire chips also consistently experienced greater relative displacements at peak points than mixtures with no tire chip inclusion.

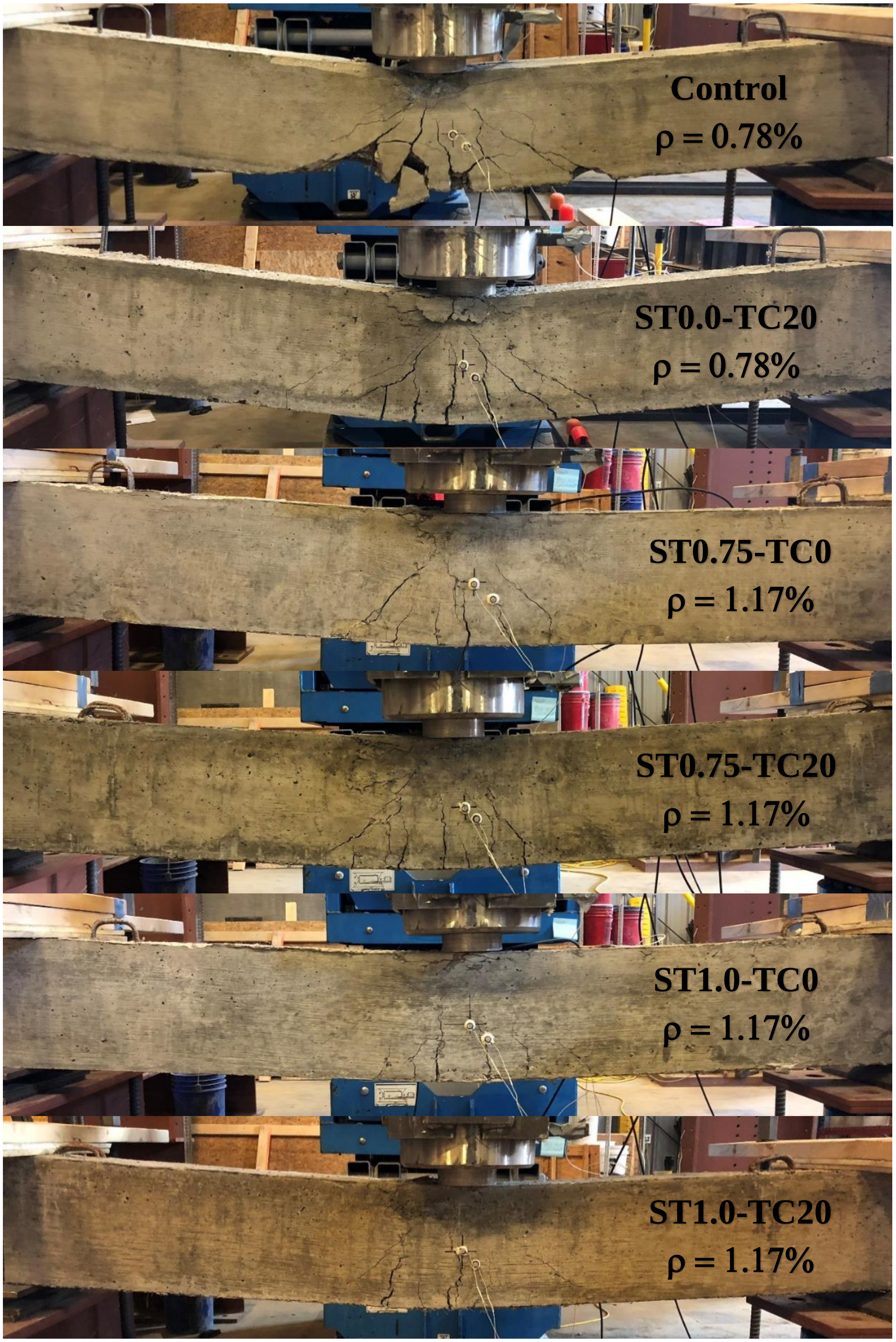

Figure 7-13. Anterior View of Fractured Impact Beam Specimens.

An anterior view of the fractured impact beams at full span are provided in Figure 7-13 to compare relative displacement. The difference in displacements between 0.78% and 1.17% steel reinforcement ratios in conjunction with steel fibers can clearly be seen by the above figure.

7.2.2 Failure Modes

There appears to be a clear difference in the degree of failure between specimens with varying steel fiber content and tire chip inclusion. The failure mode of each beam is reported in Table 7.6.

Table 7.6 – Failure Modes of Impact Beam Specimens.

Mixture Description	Failure Mode
Control (ρ = 0.78%)	Flexural/Crushing/Shear Failure
ST0.0-TC20 (ρ = 0.78%)	Flexural/Crushing/Shear Failure
ST0.75-TC0 (ρ = 1.17%)	Flexural/Crushing/Shear Failure
ST0.75-TC20 (ρ = 1.17%)	Flexural/Crushing/Shear Failure
ST1.0-TC0 (ρ = 1.17%)	No Failure; flexural cracks developed
ST1.0-TC20 (ρ = 1.17%)	No Failure; flexural cracks developed

To more closely examine the failure mechanisms between beams, enlarged photos of both the anterior face and contact surface of each beam have been provided in Figures 7-14 and 7-15, respectively.

A) Control (ρ = 0.78%)

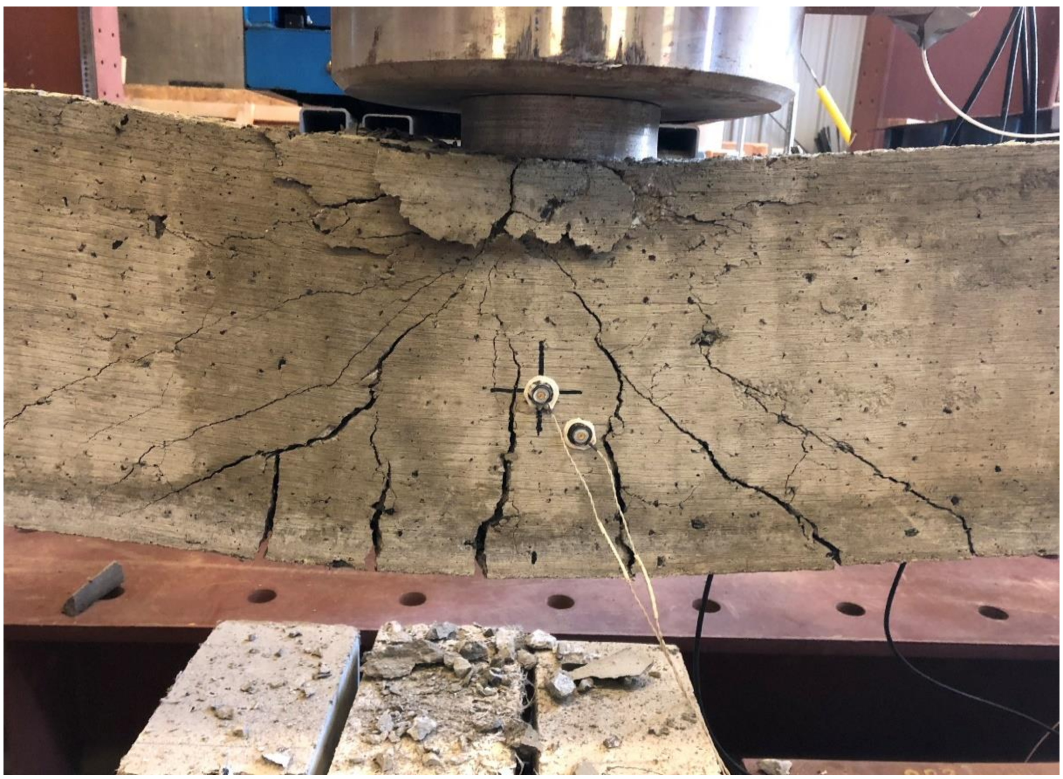

B) ST0.0-TC20 (ρ = 0.78%)

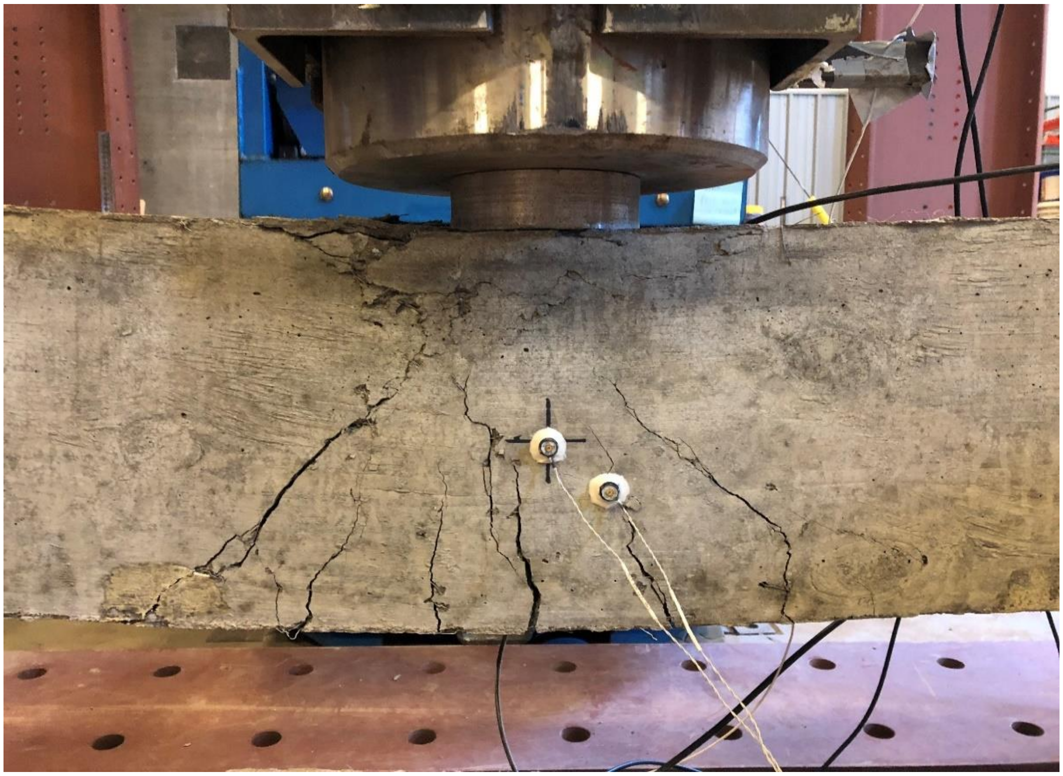

C) ST0.75-TC0 (ρ = 1.17%)

D) ST0.75-TC20 (ρ = 1.17%)

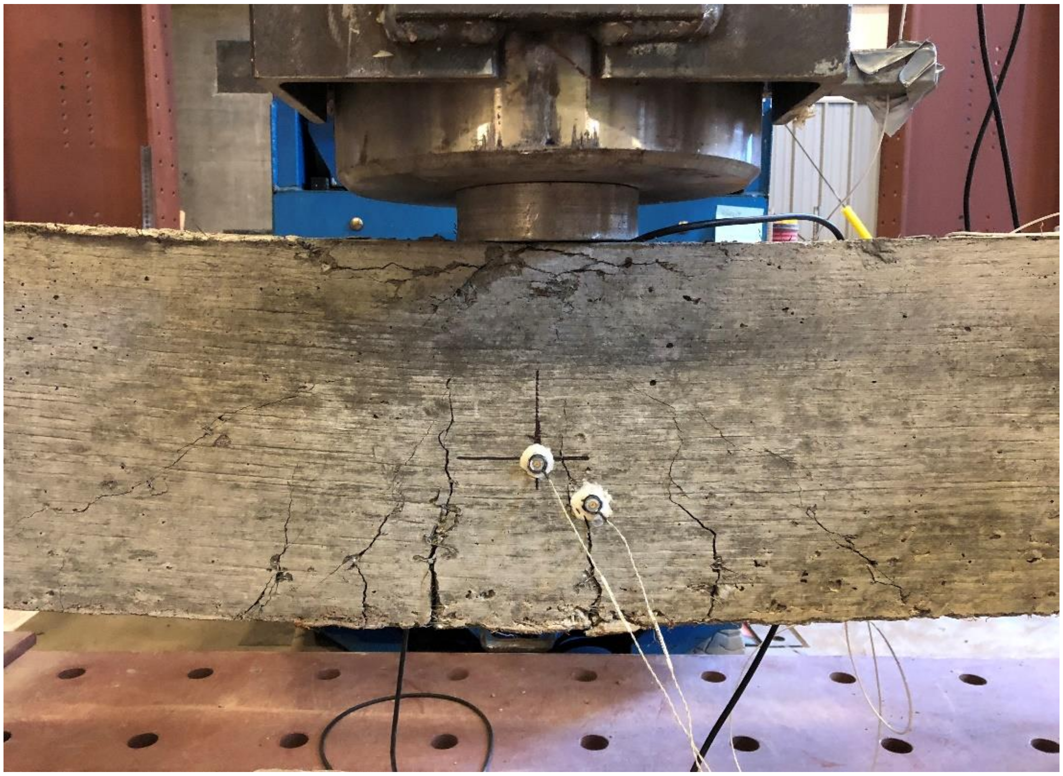

E) ST1.0-TC0 (ρ = 1.17%)

F) ST1.0-TC20 (ρ = 1.17%)

Figure 7-14. Enlarged Anterior View of Fractured Impact Beam Specimens.

A) Control (ρ=0.78%)

B) ST0.0-TC20 (ρ=0.78%)

E) ST0.75-TC0 (ρ=1.17%)

C) ST0.75-TC20 (ρ=1.17%)

F) ST1.0-TC0 (ρ=1.17%)

D) ST1.0-TC20 (ρ=1.17%)

Figure 7-15. Enlarged View of Contact Surface of Fractured Impact Beam Specimens.

7.2.2.1 Observation of Failure Modes

A) Control (ρ = 0.78%)

As expected, the Control beam experienced the greatest degree of failure. Local crushing failure at the contact surface produced significant section loss in the compressive zone. Clear signs of spalling and scabbing are observed at the contact surface and distal side of the beam, respectively. Due to the yielding of the tension steel, wide vertical flexural cracks developed from the distal side of the beam and propagated towards the point of impact. Large diagonal cracks also develop at approximately a 45˚ degree angle, signaling failure due to shear. Despite yielding of the tension steel reinforcement, there was no sign of rebar rupture.

B) ST0.0-TC20 (ρ = 0.78%)

The failure experienced by ST0.0-TC20 was very similar to the Control except for the significant section loss experienced by the latter. Spalling can be observed at the contact surface while scabbing was not present at the distal side. Although there appears to be no significant difference in crack width relative to the Control, the tire chips were able to keep the section intact, which is a property of tire chip that was observed in small scale drop-hammer impact testing in Chapter 5. The compressive and flexural failure zones were also very similar in size to the Control.

C) ST0.75-TC0 (ρ = 1.17%)

Localized compressive failure is observed at the contact surface due to crushing, but to a much lesser degree than the Control. Due to the inclusion of steel fibers, crack width is significantly reduced. Flexural cracks develop at the base and propagate approximately two-thirds the height of the beam, unlike the Control and ST0.0-TC20 which experienced crack propagation through full height of the beam. Distinct diagonal cracks are observed at approximately 45˚ that signify shear failure.

D) ST0.75-TC20 (ρ = 1.17%)

Compared to ST0.75-TC0, the number of cracks increased with tire chip inclusion. Spalling is observed at the contact surface and, based on the enlarged top view, appears to be more controlled than with ST0.75-TC0 despite a 48% decrease in compressive strength. The compressive failure zone at the contact surface is wider and does not penetrate as deep as ST0.75-TC0, perhaps suggesting a difference in how the impact energy was dissipated. Prominent diagonal cracks also seen developing at approximately 45˚.

E) ST1.0-TC0 (ρ = 1.17%)

Well distributed flexural cracks develop vertically with little to no angle. Minimal spalling relative to the other specimens is seen at the contact surface. The compressive failure zone is not as prominent in terms of depth and width relative to ST0.75-TC0 and ST0.75-TC20. Flexural crack width is also significantly reduced, additionally shortening the further the cracks were from the center of the beam. Very faint diagonal cracks are observed propagating at approximately 60˚ from the center of the beam, hinting at successful shear failure prevention.

F) ST1.0-TC20 (ρ = 1.17%)

Unlike the cracks developed in ST1.0-TC0, the flexural cracks on ST1.0-TC20 were not well distributed, being dictated by primarily two distinct cracks. Spalling was also more prominent than in ST1.0-TC0 which led to an increased compressive failure zone area. Diagonal cracks were slightly more visible than in ST1.0-TC0, but still underdeveloped relative to the other specimens. As a result, it was determined that this specimen was able to mitigate shear failure.

7.2.3 Reaction Forces

Aforementioned in Section 7.1, each beam was tested under simple-span conditions. To capture the peak impact load experienced by each beam, a load cell was placed directly underneath the pinned support. It was expected that these reaction forces would vary based on the ability of each specimen to effectively dissipate the dynamic energy produced at the point of impact. Table 7.7 compares the reaction forces experienced by each beam. Because the beam was supported at two points, the peak impact force was taken as twice the peak reaction force.

Table 7.7 – Peak Reaction Forces Derived from Load Cell.

Mixture Description	Peak Reaction Force, kips (KN)	Compressive Strength, psi (MPa)
Control (ρ=0.78%)	6.0 (26.7)	6325 (43.6)
ST0.0-TC20 (ρ=0.78%)	7.7 (34.3)	3406 (23.5)
ST0.75-TC0 (ρ=1.17%)	36.8 (163.7)	7601 (52.4)
ST0.75-TC20 (ρ=1.17%)	18.1 (80.5)	3926 (27.1)
ST1.0-TC0 (ρ=1.17%)	191.5 (851.8)	7329 (50.5)
ST1.0-TC20 (ρ= 1.17%)	155.5 (691.7)	4598 (31.7)

Figure 7-16 shows the reaction force history detected by the load cell. Peak reaction forces ranged from 6 kips to 191.5 kips. It is important to note that compressive forces were detected as negative values by the load cell and thus the negative peak force was used. The plots depicting reaction force history appeared to vary substantially between the Control and mixtures containing steel fibers. The load cell was able to register meaningful values with increasing fiber volume fraction and decreased with tire chip inclusion. Although the reaction force data for a majority of these mixtures do not represent the true load experienced by each beam, there do appear to exist consistent trends that are further explained in Section 7.3

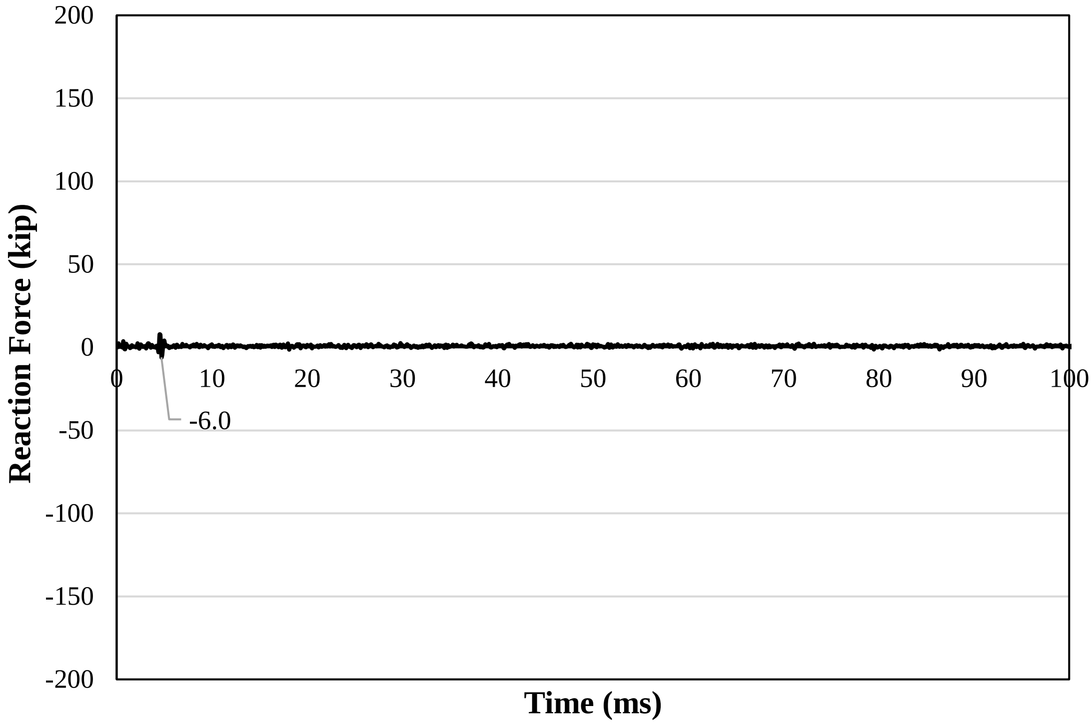

A) Control (ρ=0.78%)

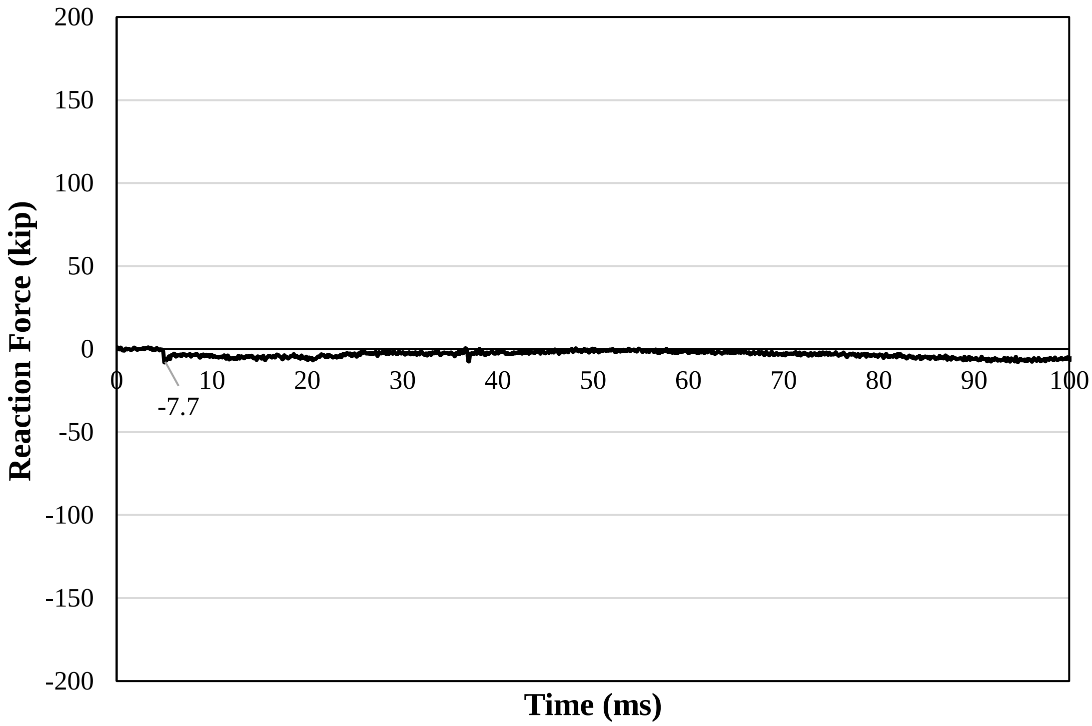

B) ST0.0-TC20 (ρ=0.78%)

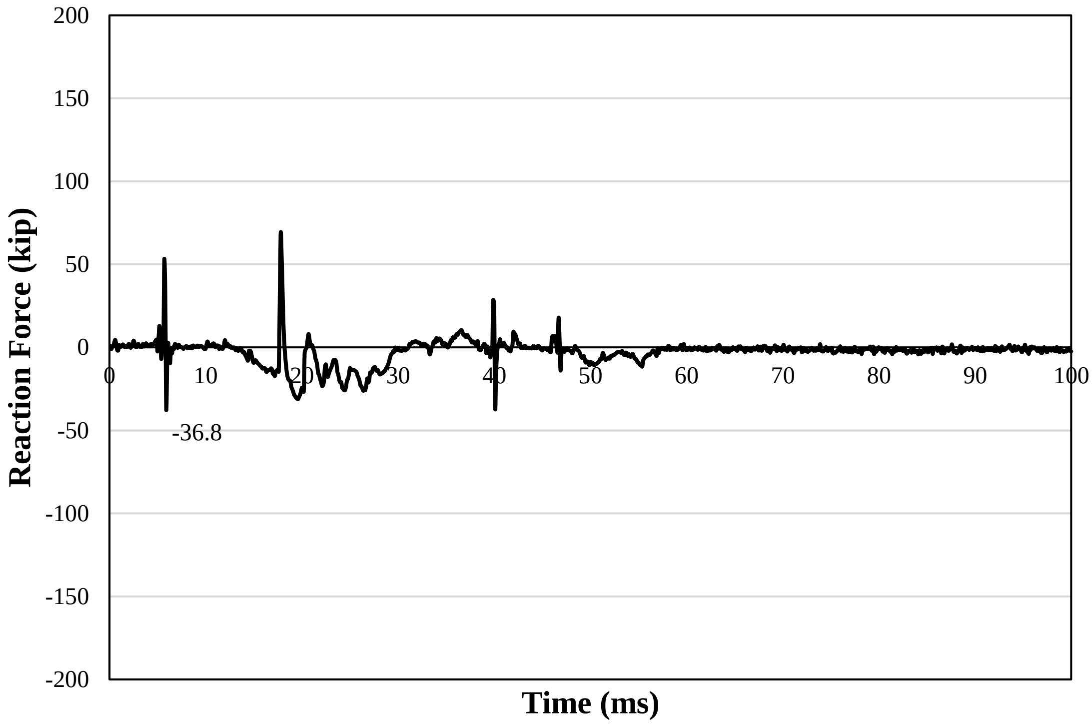

C) ST0.75-TC0 (ρ=1.17%)

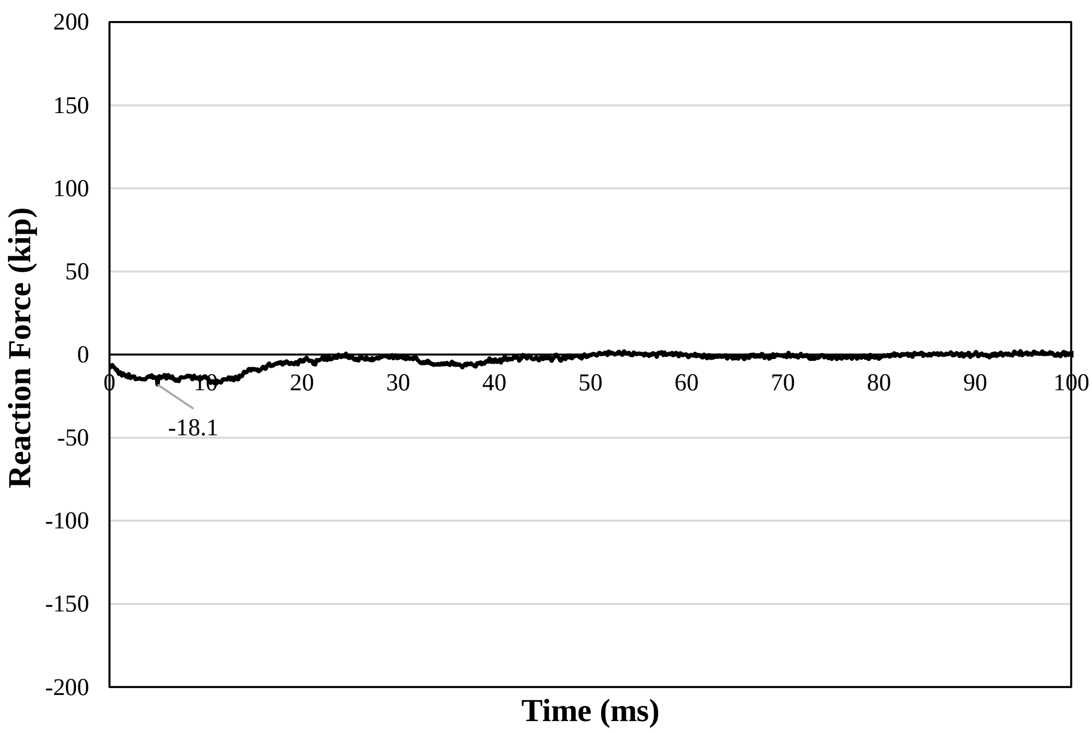

D) ST0.75-TC20 (ρ=1.17%)

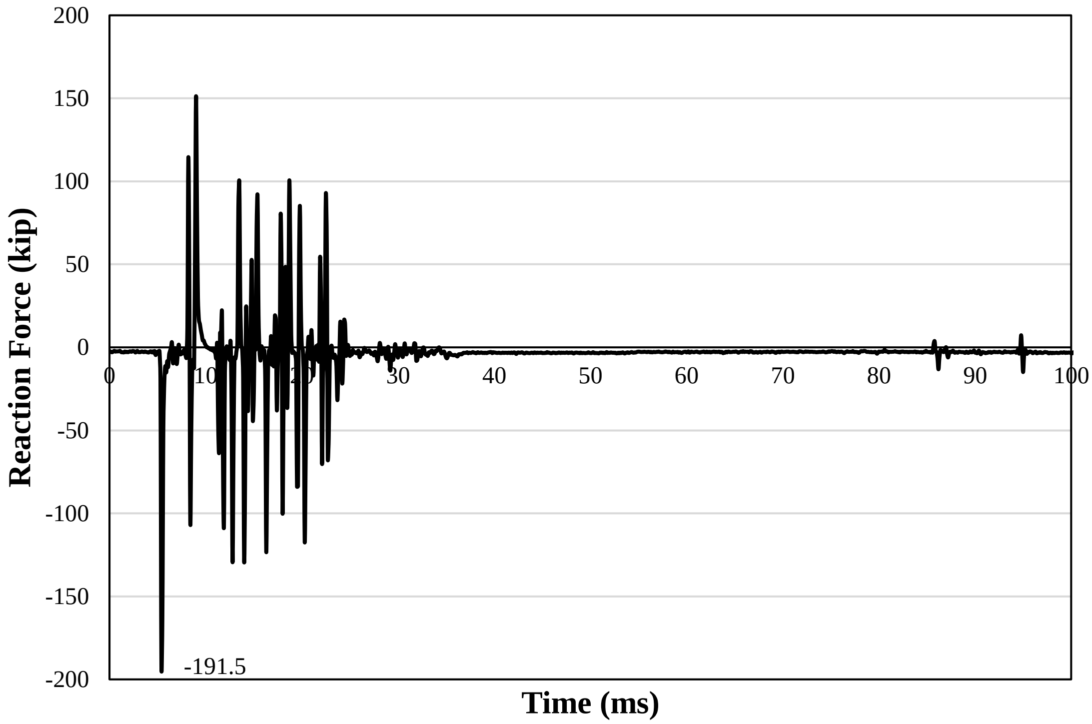

E) ST1.0-TC0 (ρ=1.17%)

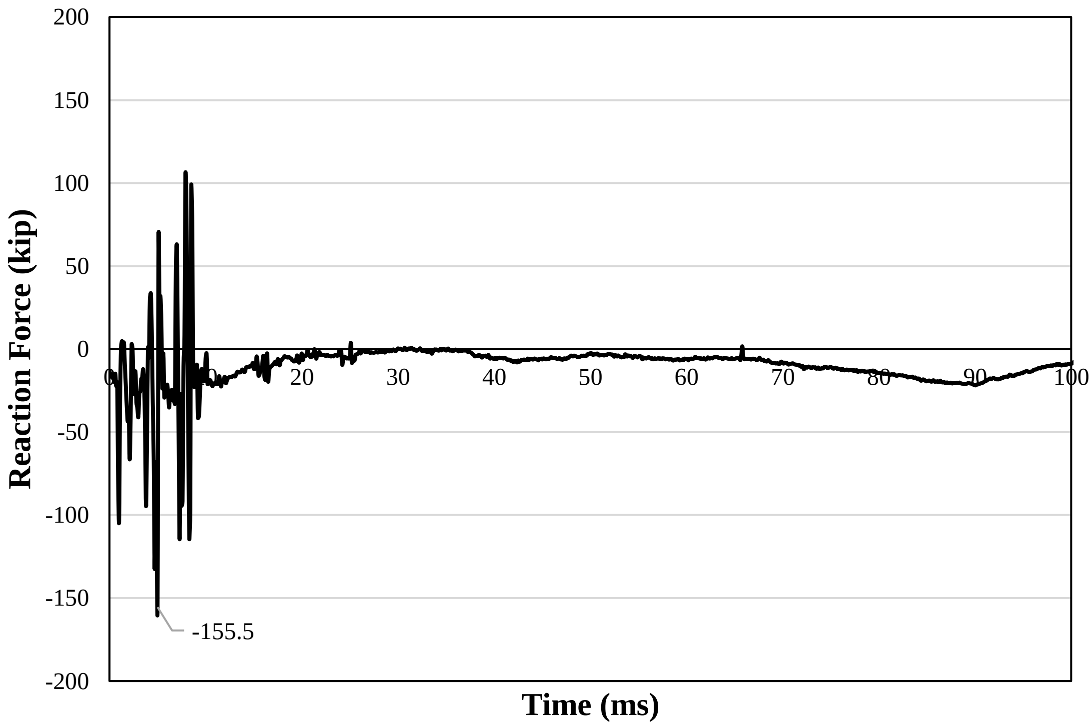

F) ST1.0-TC20 (ρ=1.17%)

Figure 7-16. Load Cell derived Reaction Forces for Impact Beam Specimens.

7.2.4 Accelerometer Data

As a supplement to the load cell data, an accelerometer was used to measure the acceleration of the drop-weight to estimate the peak impact force experienced at contact.

Table 7.8 – Peak Impact Forces Derived from Accelerometer

Mixture Description	Peak Force, kips (KN)	Compressive Strength, psi (MPa)
Control (ρ=0.78%)	471 (2095)	6325 (43.6)
ST0.0-TC20 (ρ=0.78%)	305 (1357)	3406 (23.5)
ST0.75-TC0 (ρ=1.17%)	359 (1597)	7601 (52.4)
ST0.75-TC20 (ρ=1.17%)	356 (1584)	3926 (27.1)
ST1.0-TC0 (ρ=1.17%)	438 (1948)	7329 (50.5)
ST1.0-TC20 (ρ=1.17%)	365 (1623)	4598 (31.7)

The peak impact forces derived the accelerometer range from 305 kips to 471 kips, which coincide with the ST0.0-TC20 and Control specimens, respectively. Although there was significant noise from the data, the peak impact forces that were measured followed the same trend as with the load cell. The impact force history based from the accelerometer data can be seen in Figure 7-17.

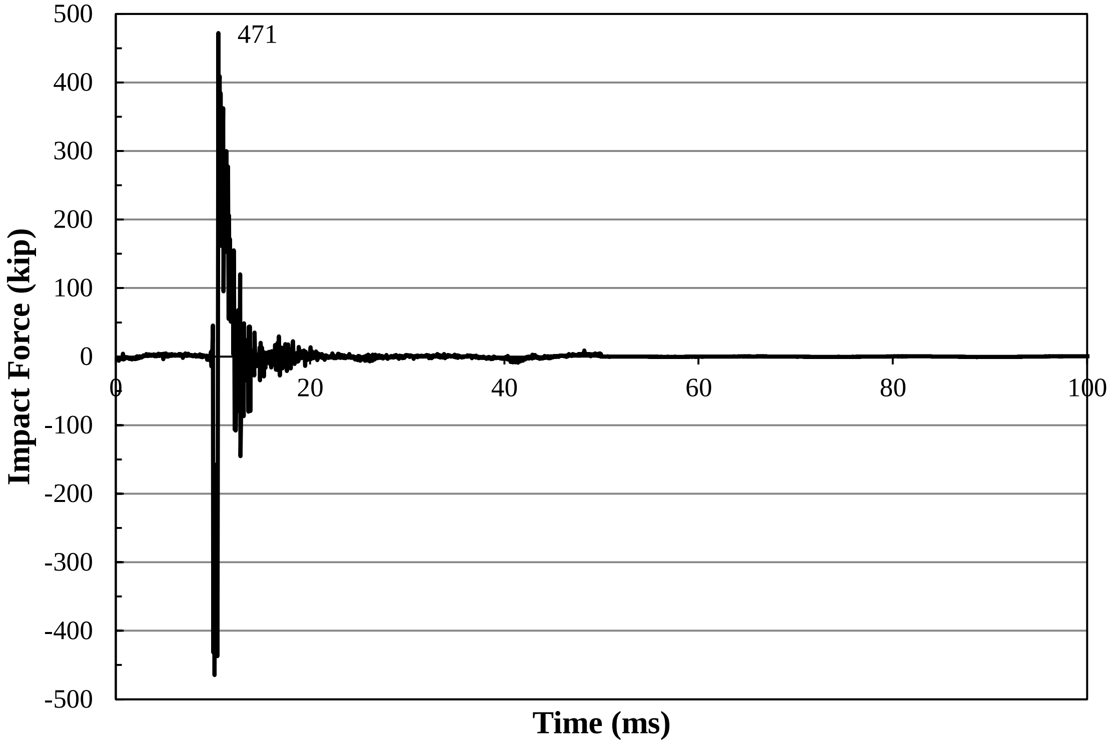

A) Control (ρ=0.78%)

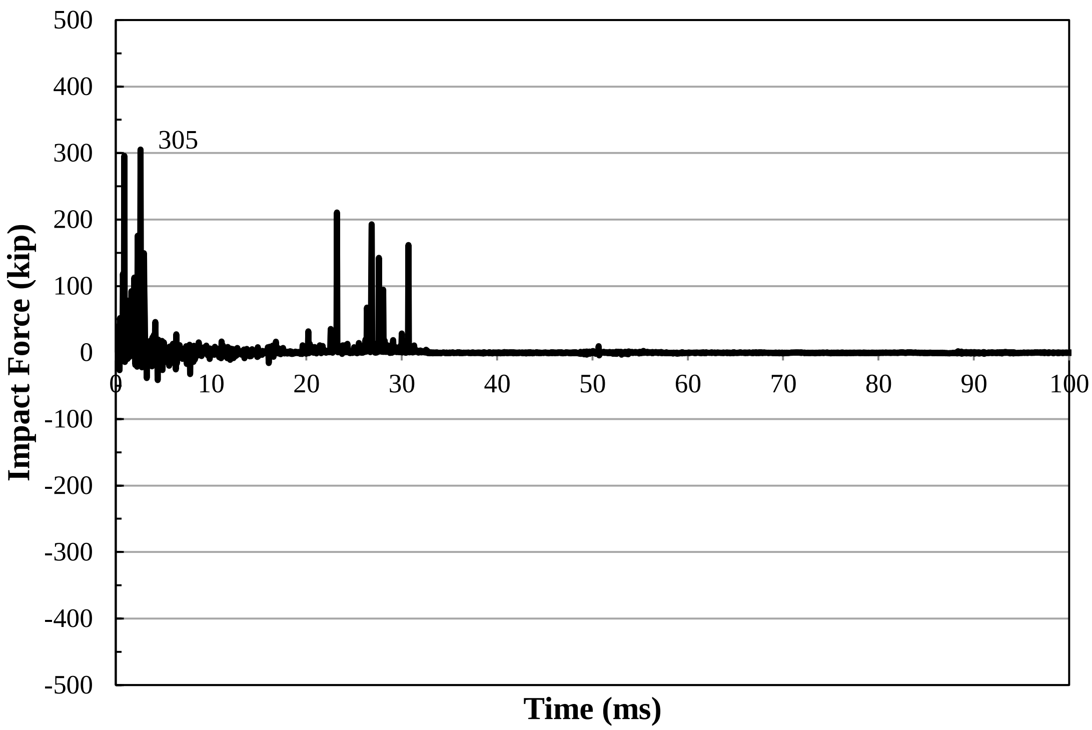

B) ST0.0-TC20 (ρ=0.78%)

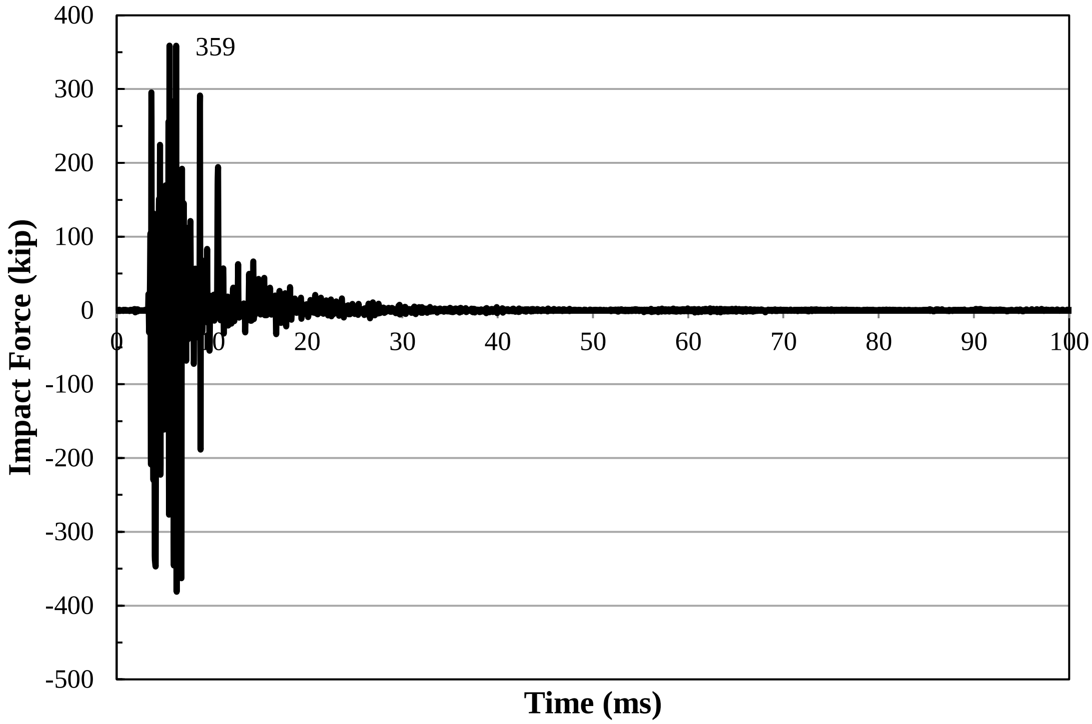

C) ST0.75-TC0 (ρ=1.17%)

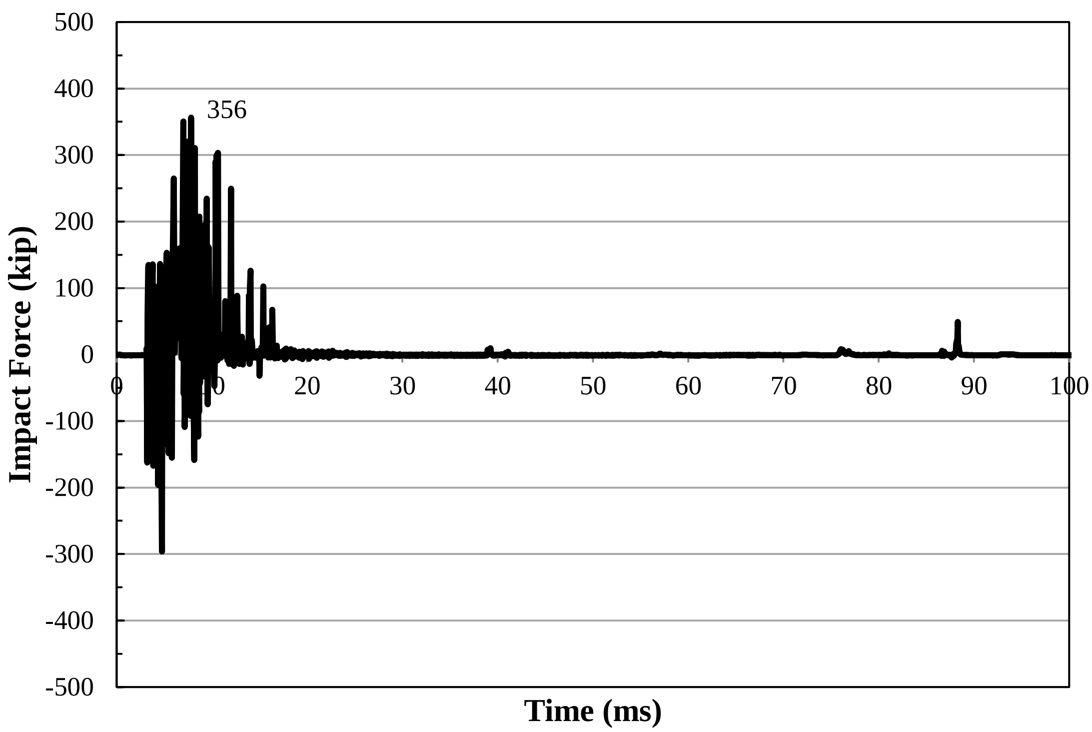

D) ST0.75-TC20 (ρ=1.17%)

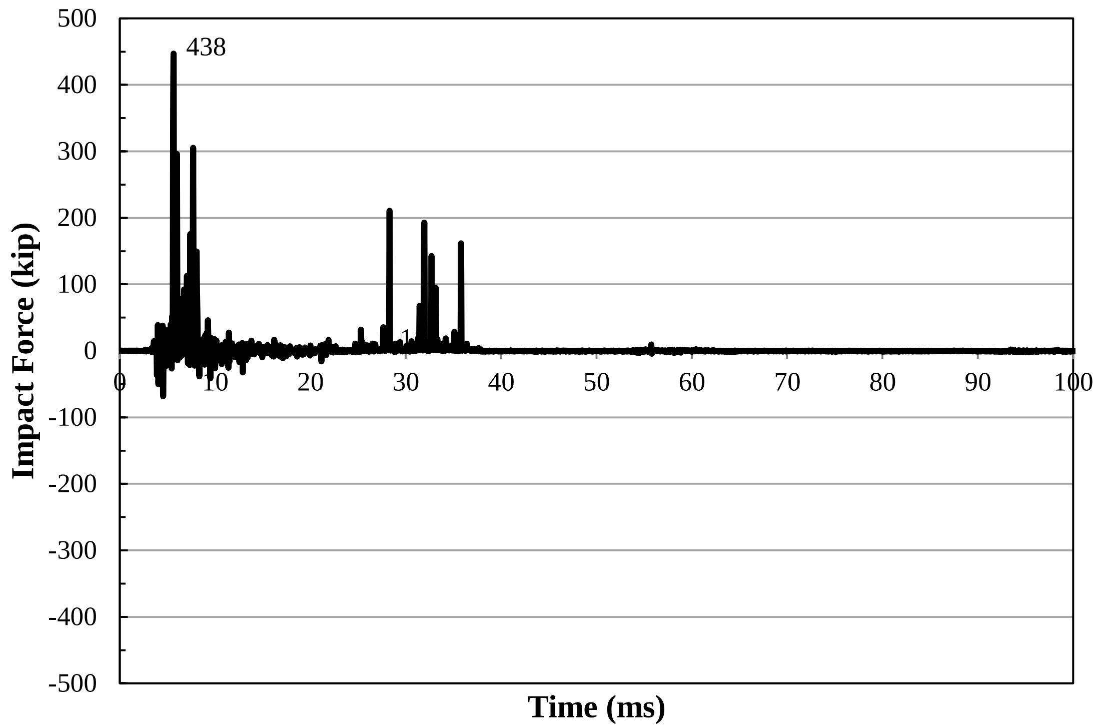

E) ST1.0-TC0 (ρ=1.17%)

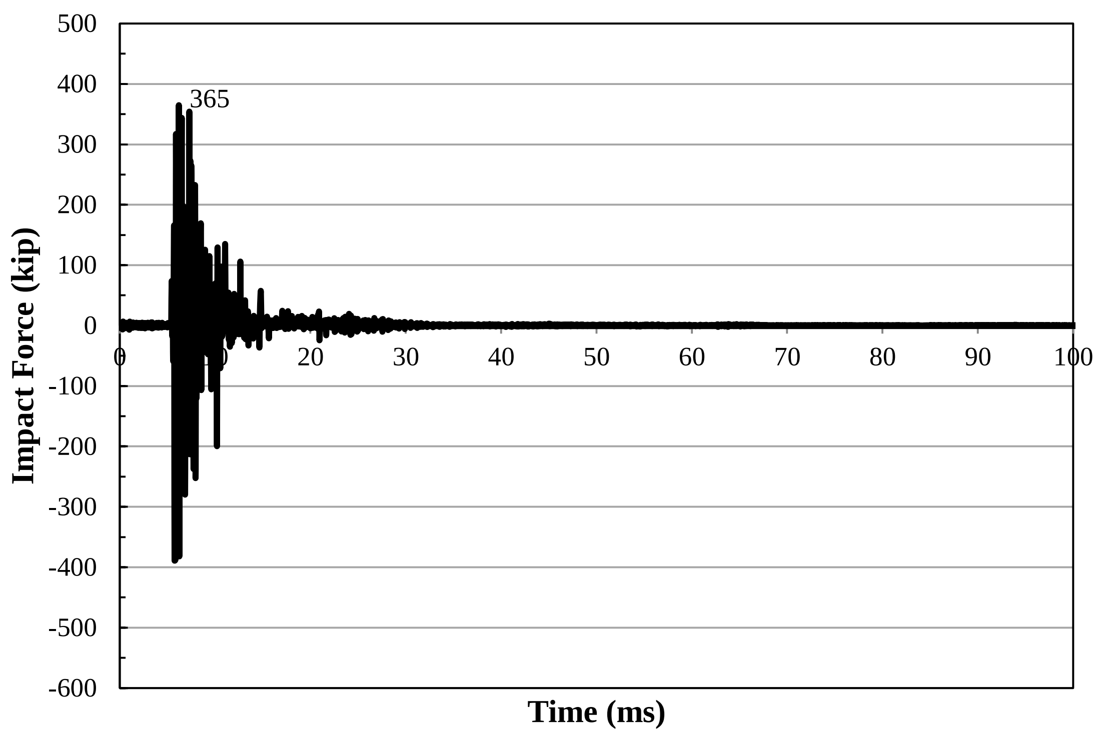

F) ST1.0-TC20 (ρ=1.17%)

Figure 7-17. Accelerometer Data for Impact Beam Specimens.

7.3 Impact Load Testing – Analysis of Results

7.3.1 Predicted Impact Forces and Displacements

From the literature review in Section 2.5, Eq. (7) was used to calculate the predicted impact force experienced by the RC beams. As a reference, the predicted impact force to be experienced by the Control beam was 368 kips, which was slightly lower than the recorded 471 kips from the accelerometer data. Theoretically, Eq. (7) assumes perfectly elastic beam conditions, but in reality, concrete is a quasi-brittle material (Afroughsabet et al. 2015). Because the stiffness of a beam reduces as it cracks, the correction factor, γ, proved necessary to quantify the predicted impact forces (Tang et al., 2005). However, it should be noted that the inclusion of fiber reinforcement and tire chips significantly alters the impact force response of the RC beams as seen from the impact test results, and therefore these predicted calculations may be slightly skewed. Sample calculations for predicted impact forces can be seen in Appendix A.3.

Mid-span displacement was also calculated using Eq. (11) from literature. Derived from a flexural wave theory (Graff, 1975), Tang et al. (2005) developed this equation to predict the mid-span displacement of a beam subjected to impact loads. Eq. (11) incorporates the previously predicted impact force, thus all of the predicted displacement values are also assuming perfectly elastic beam conditions. The predicted mid-span displacement for the Control was found to be 2.84 in. Compared to the measured 3.34 in., the predicted displacement is a slight underestimation. This was to be expected because the predicted force was also an underestimation. Furthermore, it is important to note that Eq. (11) does not take into consideration the tensile steel reinforcement ratio of the beam. Consequently, the predicted displacement values for mixtures with $\rho = 1.17\%$ are significant overestimations. For selected mixtures, the predicted mid-span displacements and impact forces can be seen in Table 7.9 for comparison. Sample calculations for predicting displacement are shown Appendix B.

Table 7.9 – Predicted Mid-Span Displacement and Impact Force

Mixture Description	Predicted Mid-Span Displacement, In. (mm)	Predicted Impact Force, kips (kN)
Control (ρ=0.78%)	2.84 (71.1)	368 (1637)
ST0.0-TC20 (ρ=0.78%)	3.57 (90.7)	339 (1508)
ST0.75-TC20 (ρ=1.17%)	3.49 (88.6)	376 (1673)
ST1.0-TC20 (ρ=1.17%)	3.31 (84.1)	384 (1708)

7.3.2 Summary of Measured Impact Forces and Reactions

The impact forces calculated from the accelerometer measurements and reaction forces were compared, and the results were discussed in conjunction with impact types and local/global failure modes available in literature. In Table 7.10, the comparison between the peak impact forces measured by the load cell and accelerometer is shown.

Table 7.10 – Comparison of Peak Impact Forces

Mixture Description	Peak Impact Force from Load Cell, kips (kN)	Peak Impact Force determined from Accelerometer, kips (kN)
Control (ρ=0.78%)	12.0 (53)	471 (2095)
ST0.0-TC20 (ρ=0.78%)	15.4 (69)	305 (1357)
ST0.75-TC0 (ρ=1.17%)	73.6 (327)	359 (1597)
ST0.75-TC20 (ρ=1.17%)	36.2 (161)	356 (1584)
ST1.0-TC0 (ρ=1.17%)	383 (1704)	438 (1948)
ST1.0-TC20 (ρ=1.17%)	311 (1383)	365 (1623)

It is clear that the load cell was unable to register the peak impact forces for all the specimens below 1.0% steel fiber volume fraction. At 1.0%, the results derived from the load cell and accelerometer data are very similar, with the accelerometer registering a 17.4% and 14.4% greater peak impact force without tire chips and with tire chips, respectively. Relatively speaking, both forms of measurement captured similar impact force responses as a result of tire chip inclusion. However, at least at 1.0% steel fiber volume fraction, the load cell data can be taken with greater confidence, because it is a direct measure of the beam response, whereas the accelerometer data correlates to the impact response of the drop-weight. Ultimately, the accelerometer data provides a close approximation to the actual impact force for all beams tested. Even though the load cell data is not reliable with the mixtures below 1.0% steel fiber volume fraction, it does show a consistent trend and explains how these beams distributed the impact forces to the supports.

To better understand the potential reasons for why the load cell was unable to capture the true peak impact forces for the majority of mixtures, the failure modes of each beam must be analyzed. Table 7.11 summarizes the failure modes previously shown in Section 7.2.2.

Table 7.11 – Impact Types and Failure Modes

Mixture Description	Soft/Hard impact	Local/Global Failure Modes
Control (ρ=0.78%)	Hard	Local – scabbing
ST0.0-TC20 (ρ=0.78%)	Hard	Local – spalling
ST0.75-TC0 (ρ=1.17%)	Soft	Local – cone cracking
ST0.75-TC20 (ρ=1.17%)	Soft	Local – cone cracking
ST1.0-TC0 (ρ=1.17%)	Soft	Global –overall target response
ST1.0-TC20 (ρ=1.17%)	Soft	Global –overall target response

According to Jiang et al. (2014), there exists two categories of structural impact: soft missile impact (impulsive loading, impulse driven) and hard missile impact (impactive loading, energy driven). A soft impact is defined when the target remains undamaged while the projectile is crushed, whereas a hard impact involves the projectile penetrating the target (Kœchlin et al. 2009). As previously stated in the literature review in Section 2.5, there are two distinct types of structural failure modes (Li et al., 2005). In summary, Li et al. (2005) describes local failure by the following impact effects (See Figure 2-9): (1) the projectile penetrates the target to a certain depth; (2) cone cracking (development of cracks in a cone-like pattern); (3) ejection of target material from contact surface (spalling); (4) ejection of target material from distal surface of impact (scabbing); and (5) complete penetration through the target material (perforation). Excessive local damage can be mitigated by taking into account a combination of wall thickness, percentage of reinforcement, and material strength (Jiang et al., 2014). For the purpose of this study, a global target response was desired. Global failure response is defined as the global bending, shear, and membrane responses throughout the target (Li et al., 2005).

The peak impact force is generally higher than expected. This is due to the 20,000 Hz sampling rate and noise. However, there appears to be a consistent trend between the measurements. The ‘hard impact’ type (Control and ST0-TC20) resulted in relatively higher impact forces. The following sub-sections further discuss possible reasons as to why load cell was unable to adequately register valid peak forces.

7.3.2.1 Failure modes

As shown in Section 7.2.2, both the Control and ST0.0-TC20 experienced significant failure and section loss. Considering how significant the section loss in both the compressive and flexural zones was in the Control especially, a significant amount of the impact force was spent through contact surface fracture and strain energy resulting in scabbing. It appears that the fractures prevented the Control specimen from effectively distributing the impact force to the support where the load cell was located. Despite the tire chip’s ability to keep the beam intact from spalling on the contact surface and scabbing, the size of the compressive and flexural zone failure between the two beams was very similar. Coupled with fracture energy loss, similar explanation as the Control is provided with ST0.0-TC20.

7.3.2.2 Diagonal Shear Cracks

There is a positive correlation within the load cell data relating shear cracks and load registry. In this case, the Control and ST0.0-TC20 exhibited the widest and most distinct shear cracks compared to the rest of the specimens. The width of shear cracks decreased with increasing steel fiber volume fraction, with the beams consisting of 1.0% steel registering legitimate peak reaction forces.

7.3.2.3 Rebounding Effects

As aforementioned in the discussion of mid-span displacement, the beams were allowed minimal vertical movement to allow rotation, which ultimately caused the beams to bounce slightly immediately after impact. During this short period (~ < 5ms) in which the beams were suspended in the air, the beam might have not been in full contact with the supports, resulting in the load cell missing the initial peak. The forces registered could be rebounding forces experienced when the beam came back down. However, this role may be insignificant, since stiffer beams, which also experienced a similar rebounding movement, had a better registered reaction force.

7.3.2.4 Sampling Rate

The load cell was set to measure points at 10,000 Hz, whereas the accelerometer was set to 20,000 Hz. It is possible that because the accelerometer recorded twice as many points as the load cell, it was able to capture the true peak impact force. There was no benefit to increasing the sampling rate of the load cell to match the accelerometer because of the limitations of the load cell itself.

As a result, only the load data derived from the accelerometer will be discussed for these selected mixtures. As previously seen in Table 7.8, peak impact loads determined the accelerometer data for the Control and ST0.0-TC20 are 471 kips (2095 kN) and 305 kips (1357 kN), respectively. Tire chip inclusion resulted in a 35.2% reduction to impact load. This impact load reduction is consistent with the proven force dampening properties of tire chips. It is important to note the failure modes when comparing these loads, especially in the compressive zone. Although the compressive strength of the Control (6235 psi) was significantly greater than that of ST0.0-TC20 (3406 psi), the compressive zone areas were very similar in size and shape with the only significant difference being the retention of section by ST0.0-TC20. As the beam with less stiffness, ST0.0-TC20 experienced a much lower impact load, but as previously mentioned only exhibited a 4.8% increase in displacement compared to the Control. Due to the significant section loss experienced by the Control, its moment of inertia effectively decreased, which led to increased deflection.

7.3.3 Effect of Tire Chip Inclusion versus Control

Based on the results presented in Section 7.2, when comparing the Control to ST0.0-TC20, a 20% tire chip inclusion had positive effects on mid-span displacement and peak impact force. This is consistent with the results from Chapters 5 and 6, in which tire chips appeared to increase impact resilience and ductility.

7.3.3.1 Effect of Tire Chip Inclusion on Mid-Span Deflection

As shown in Table 7.12, ST0.0-TC20 experienced an increase of 4.5% final mid-span deflection compared to the Control. The reduction in stiffness caused by tire chip replacement of coarse aggregate resulted in an increase in ductility. This increase in deflection is supported by the static test results from Section 6.3.1, in which ST0.0-TC20 experienced a more prominent 37% increase in mid-span deflection relative to the Control.

Table 7.12 – Comparison of Displacement History between Control and ST0.0-TC20

	Displacement, in								**Duration**
Mixture Description	A	B	C	D	E	F	G	Final	Time, ms
Control (ρ=0.78%)	4.02	3.36	3.57	3.34	3.43	3.37	-	3.34	780
ST0.0-TC20 (ρ=0.78%)	4.18	3.48	3.78	3.51	3.64	3.57	3.54	3.51	998

Another outcome to note is the change in duration of the displacement history with tire chip inclusion. The duration of the beam response between the Control and ST0.0-TC20 was 780 and 998 ms, respectively. This 28% increase in impact duration indicates that ST0.0-TC20 dissipated the initial kinetic energy over a longer duration of time through rebounding rather than resulting in fractures (i.e., converting the kinetic energy to surface and strain energy).

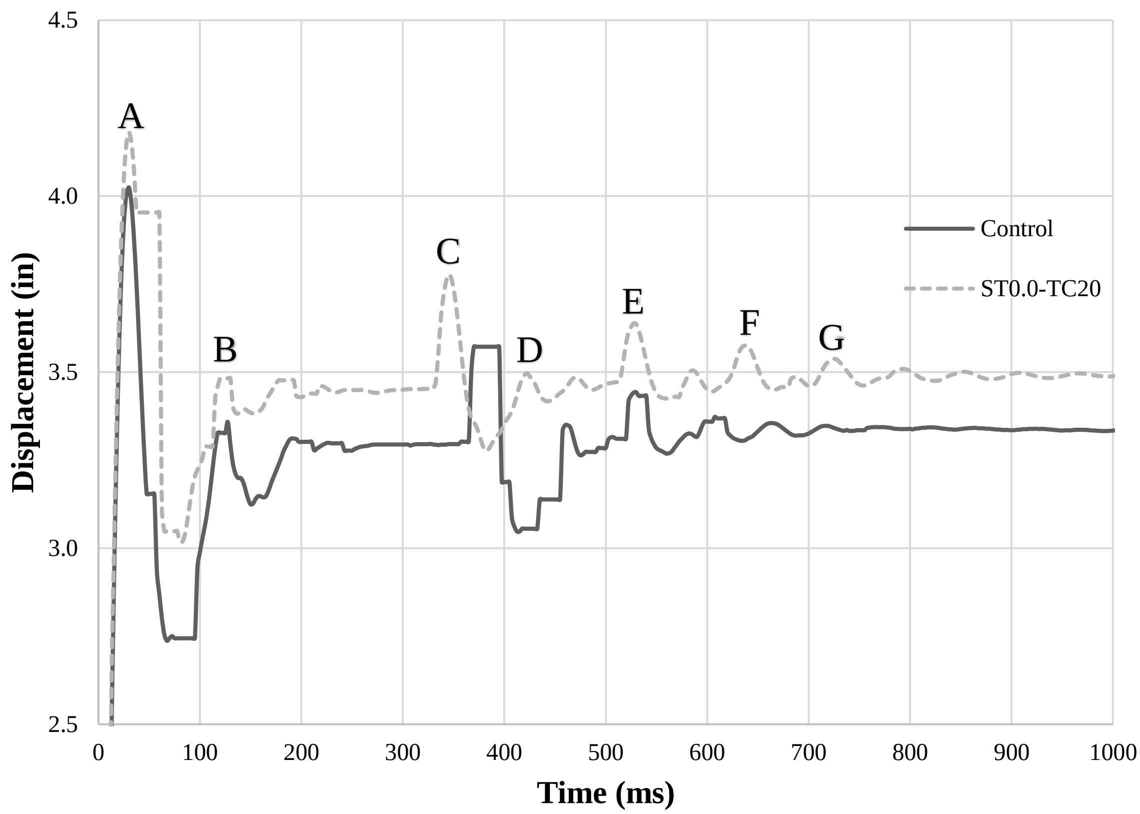

Figure 7-18. Effect of Tire Chip Inclusion on Displacement-Time History

Based on Figure 7-18, it is inferred that peak points A, C, E, F, G are the result of initial and subsequent impact forces from the rebounding drop weight, whereas points B and D are where the beams experience elastic deformation as they attempt to completely redistribute the kinetic energy from each impact. There are other points in the displacement history where similar effects to points B and D are seen, but they are less prominent and more difficult to compare with the

Control. As an example, only the lettering for ST0.0-TC20 are shown in Figure 7-18. Displacements at Point B experienced the greatest recovery not only due to a greater initial impact, but also because the beams experienced slight uplifting effects through the deformation of the 1 in. (25.4 mm) thick insulation on each end of the beam. However, this uplifting effect was controlled and consistent with every beam. This slight uplifting effect was implemented to allow the beams to rotate freely at the supports.

Taking into account the change in displacement relative to the final displacement at points C through G in Table 7.13, ST0.0-TC20 deflected either equal to or more than the Control. The negative value at point B for ST0.0-TC20 could suggest greater recovery potential over the entire displacement-time history; however, the total displacement change from Point A to final displacement for both beams suggests almost identical displacement recovery. ST0.0-TC20 recovered slightly more initial-displacement after impact from point A to B than the Control with a displacement recovery of 16.7% (0.70 in.) compared to 16.4% (0.66 in.), respectively.

Table 7.13 – Relative Change in Displacement between Control and ST0.0-TC20

	Change in Displacement Relative to Final Displacement, in						
Mixture Description	A	B	C	D	E	F	G
Control (ρ=0.78%)	0.68	0.02	0.23	0.00	0.09	0.03	-
ST0.0-TC20 (ρ=0.78%)	0.67	-0.03	0.27	0.00	0.13	0.06	0.03

Although further tests would need to be conducted to determine if tire chip inclusion has an effect on total strain recovery, due to the increase of testing time and increased strain recovery throughout various points of the displacement history, it is determined that tire chip inclusion more effectively dissipates dynamic energy than the Control based on mid-span displacement.

7.3.3.2 Effect of Tire Chip Inclusion on Impact Forces

Impact forces are difficult to compare between the results from the load cell and accelerometer for the selected mixtures because of the disparity between values. These values are presented in Table 7.14.

Table 7.14 – Comparison of Impact Forces between Control and ST0.0-TC20

Mixture Description	Impact Force due to Load Cell, kips (KN)	Impact Force due to Accelerometer, kips (KN)	Predicted Impact Force, kips (KN)	Compressive Strength, psi (MPa)
Control (ρ=0.78%)	12.0 (53)	471 (2095)	368 (1637)	6325 (43.6)
ST0.0-TC20 (ρ=0.78%)	15.4 (69)	305 (1357)	339 (1508)	3406 (23.5)

7.3.4 Effect of Tire Chip Inclusion in FRC Beams

After analyzing the relationship between tire chip inclusion and impact resilience in standard concrete, it is necessary to analyze this same relationship with FRC mixtures. As seen in results gathered from preliminary impact testing in Chapter 5, tire chips had a distinct ability to increase the number of drops needed to induce failure on a specimen. This effect was even more prominent in conjunction with fiber reinforcement.

7.3.4.1 Effect of Tire Chip Inclusion on FRC Beam Mid-Span Deflection

A) <u>ST0.75-TC0 vs ST0.75-TC20</u>

The comparison between displacements regarding ST0.75-TC0 and ST0.075-TC20 are presented in Table 7.15. At 0.75% steel fiber volume fraction, a 20% tire chip inclusion increased final displacement by 28%.

Table 7.15 – Comparison of Displacement History between V_{sf} = 0.75% Beams

	Displacement, in								Duration
Mixture Description	A	B	C	D	E	F	G	Final	Time, ms
Control (ρ=0.78%)	4.02	3.36	3.57	3.34	3.43	3.37	-	3.34	780
ST0.75-TC0 (ρ=1.17%)	2.39	1.64	1.93	1.717	1.81	1.74	-	1.71	898
ST0.75-TC20 (ρ=1.17%)	2.92	2.24	2.52	2.21	2.3	2.25	2.22	2.19	985

The duration of testing time also increased from 898 to 985 ms, resulting in a 9.8% increase. Although not as significant as the 28% increase in duration time between the Control and ST0.0-TC20, this reinforces the notion that tire chip inclusion results in more effective energy distribution through rebounding effects.

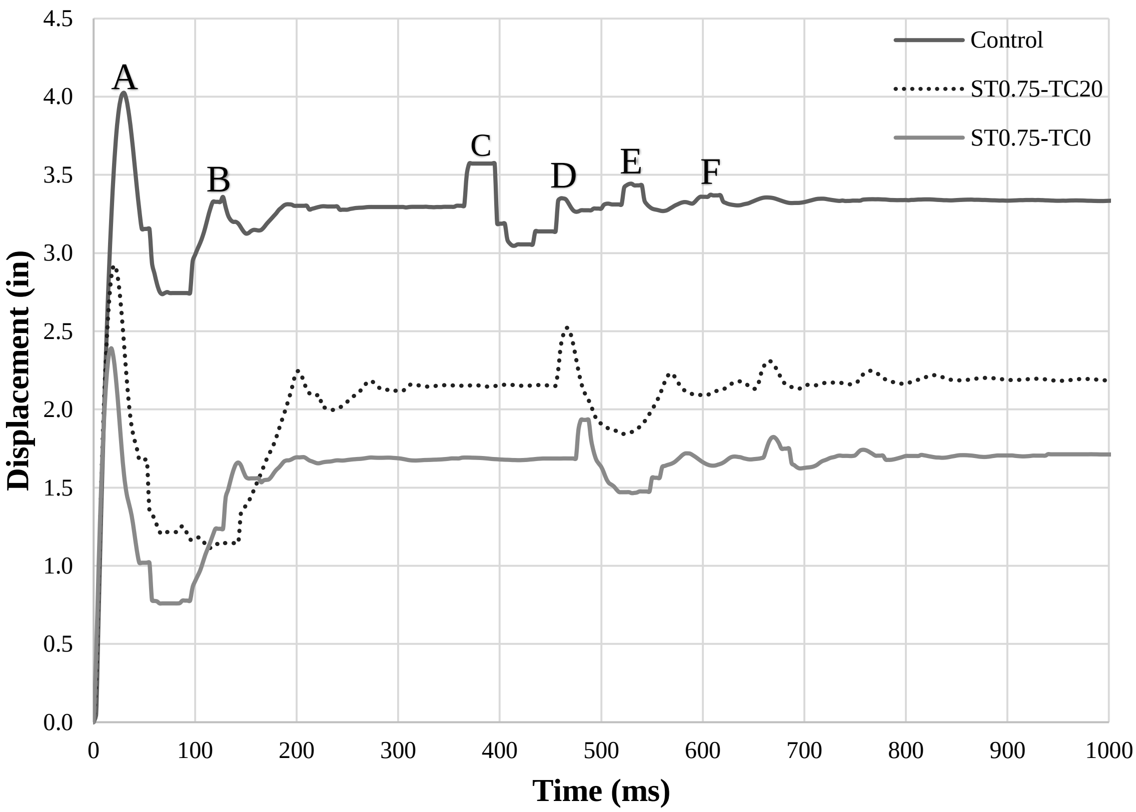

Figure 7-19. Effect of Tire Chip Inclusion on FRC Displacement History at V_{sf} = 0.75%.

From Figure 7-19, the duration of the impact response is more clearly seen. It is observed that there is a greater time disparity between points A and B for ST0.75-TC20 than ST0.75-TC0. Although it took slightly longer for ST0.75-TC20 to rebound and recover initial displacement, the recovery of initial displacement was less than that of ST0.75-TC0. From point A to B, ST0.75-TC0 recovered 31.4% (0.75 in.) initial displacement, whereas ST0.75-TC20 only recovered 23% (0.68 in.). This trend is opposite to that of the Control and ST0.0-TC20, however the difference between displacement recoveries between those two specimens were not as significant. This increase in relative displacement recovery could result from ST1.0-TC0 possessing a much higher modulus of elasticity than ST0.0-TC20 based on compressive strength.

From Table 7.16, it is clear that tire chip inclusion results in increased change in displacement relative to final displacement, especially at points A and C. The Control and ST0.75-TC0 beams appear to consistently perform relatively the same throughout the displacement history but ST0.75-TC20 is a clear outlier. This is expected due to increased ductility with tire chip inclusion.

Table 7.16 – Relative Change in Displacement between V_{sf} = 0.75% Beams

	Change in Displacement Relative to Final Displacement, in						
Mixture Description	A	B	C	D	E	F	G
Control (ρ=0.78%)	0.68	0.02	0.23	0.00	0.09	0.03	-
ST0.75-TC0 (ρ=1.17%)	0.68	-0.07	0.22	0.01	0.10	0.03	-
ST0.75-TC20 (ρ=1.17%)	0.73	0.05	0.33	0.02	0.11	0.06	0.03

B) <u>ST1.0-TC0 vs ST1.0-TC20</u>

Similar observations are made when comparing ST1.0-TC0 and ST1.0-TC20. Tire chip inclusion at 1% steel increase final displacement by 40%, much higher than the 4.5% and 28% increases with the Control and 0.75% steel, respectively.

Table 7.17 – Comparison of Displacement History between V_{sf} = 1.0% Beams

	Displacement, in								**Duration**
Mixture Description	A	B	C	D	E	F	G	Final	Time, ms
Control (ρ=0.78%)	4.02	3.36	3.57	3.34	3.43	3.37	-	3.34	780
ST1.0-TC0 (ρ=1.17%)	2.03	1.37	1.62	1.35	1.45	1.4	-	1.34	950
ST1.0-TC20 (ρ=1.17%)	2.62	1.88	2.18	1.86	1.93	1.92	1.89	1.87	1020

Tire chip inclusion also had an effect on the duration of the displacement history, increasing the testing time from 950 to 1020 ms relative to 1% without tire chip. This 7.4% increase in duration of displacement history is also a decrease relative to the 28% and 9.8% duration increase with the Control and 0.75% steel, respectively. It would seem that the effectiveness of tire chip inclusion decreases with increasing steel fiber volume fraction.

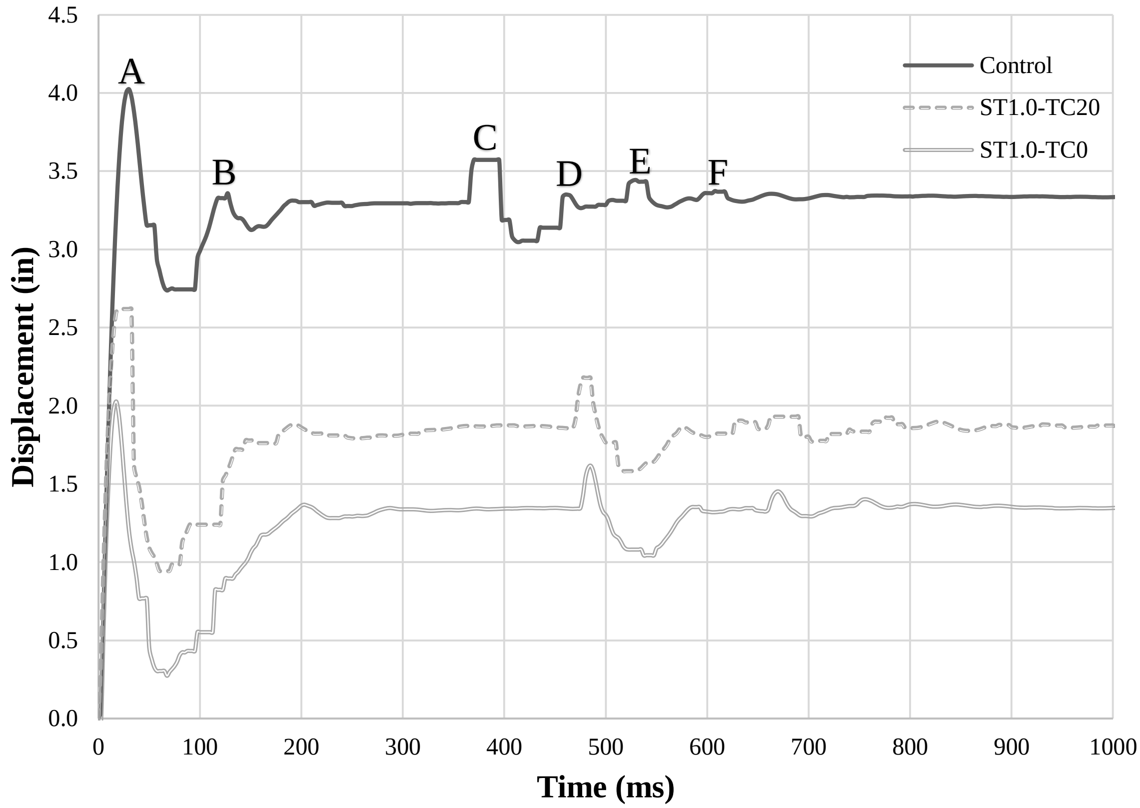

Figure 7-20. Effect of Tire Chip Inclusion on FRC Displacement History at V_{sf} = 1.0%.

The shape of the displacement-time history between ST1.0-TC0 and ST1.0-TC20 are almost identical, with the latter simply being shifted higher. Because overall displacement history duration appears to correlate with how energy is distributed within each beam, it is understandable for both of these selected histories to appear very similar. The testing time duration was very much closer in this case.

The total relative displacement recovery from point A to point B was also very similar. ST1.0-TC0 and ST1.0-TC20 recovered 33% (0.66 in.) and 28% (0.74 in.) of initial displacement, respectively. Not only does this support the increased strain recovery experienced by 0.75% steel with no tire chip inclusion, but the disparity between strain recoveries of the two 1% steel mixtures is also lesser than at 0.75%.

Table 7.18 – Relative Change in Displacement between V_{sf} = 1.0% Beams

	Change in Displacement Relative to Final Displacement, in						
Mixture Description	A	B	C	D	E	F	G
Control (ρ=0.78%)	0.68	0.02	0.23	0.00	0.09	0.03	-
ST1.0-TC0 (ρ=1.17%)	0.69	0.03	0.28	0.01	0.11	0.06	-
ST1.0-TC20 (ρ=1.17%)	0.75	0.01	0.31	-0.01	0.06	0.05	0.02

To further reinforce the idea that the energy dissipation potential of tire chip inclusion is nearly mitigated at 1.0% steel volume fraction, Table 7.18 compares relative displacement between both mixtures. Unlike with the Control and 0.75% steel, relative displacements between points at 1% steel seem to have little variance, with the exception of at point A. Even at point C, which was the point in which ST0.75-TC20 experienced a much greater change in displacement compared to ST0.75-TC0 (0.33 vs 0.22 in.), very little variance is observed between the two 1% steel specimens.

7.3.4.2 Effect of Tire Chip Inclusion on FRP Beam Impact Forces

A) <u>ST0.75-TC0 vs ST0.75-TC20</u>

Focusing on ST0.75-TC0 and ST0.75-TC20, similar issues were experienced with the load cell as with the Control and ST0.75-TC20, however not as prominently. From the Table 7.19, the recorded load cell results for ST0.75-TC0 and ST0.75-TC20 were 73.6 kips and 36.2 kips, respectively. Although the magnitude of the values themselves do not represent the peak forces, the relative values indicate a dampening of the force with tire chip inclusion.

Table 7.19 – Comparison of Impact Forces between V_{sf} = 0.75% Beams

Mixture Description	Impact Force due to Load Cell, kips (KN)	Impact Force due to Accelerometer, kips (KN)	Predicted Impact Force, kips (KN)	Compressive Strength, psi (MPa)
Control (ρ=0.78%)	12.0 (53)	471 (2095)	368 (1637)	6325 (43.6)
ST0.75-TC0 (ρ=1.17%)	73.6 (327)	359 (1597)	-	7601 (52.4)
ST0.75-TC20 (ρ=1.17%)	36.2 (161)	356 (1584)	367 (1673)	3926 (27.1)

The accelerometer data shows less of a difference in impact force, with ST0.75-TC0 and ST0.75-TC20 measuring at 359 kips and 356 kips, respectively. Referencing Figure 7-15, the failure modes between both beams were also very similar. Although there was a reduction in compressive strength with tire chip inclusion, the areas of the compressive zone were comparable, but distributed differently. Based on the accelerometer data, it is concluded that the drop-weight experienced almost the same force response due to similar failures at the contact surface.

B) <u>ST1.0-TC0 vs ST1.0-TC20</u>

As previously mentioned, the impact forces on mixtures at 1% steel volume fraction were the only beams that were reliably detected. Because these two beam possessed the greatest stiffness and did not experience section loss like the Control beam, the load was effectively able to distribute to the supports. As presented in Table 7.20, the peak impact forces, derived from the reaction forces, for ST1.0-TC0 and ST1.0-TC20 were 383 ksi and 311 ksi. For the selected mixtures, tire chip inclusion reduced the impact force by 18.8%.

Table 7.20 – Comparison of Impact Forces between V_{sf} = 1.0% Beams

Mixture Description	Impact Force due to Load Cell, kips (KN)	Impact Force due to Accelerometer, kips (KN)	Predicted Impact Force, kips (KN)	Compressive Strength, psi (MPa)
Control (ρ=0.78%)	12.0 (53)	471 (2095)	368 (1637)	6235 (43.6)
ST1.0-TC0 (ρ=1.17%)	383 (1704)	438 (1948)	-	7329 (50.5)
ST1.0-TC20 (ρ=1.17%)	311 (1383)	365 (1623)	384 (1708)	4598 (31.7)

The accelerometer data measured a slightly higher peak force with ST1.0-TC0 and ST1.0-TC20 at 438 kips and 365 kips, respectively. Despite measuring a higher force, the reduction of 16.7% of impact force is very consistent with the load cell data. The compressive zone between both beams did differ more so than with the beams with 0.75% steel volume fraction. In this case, there is only minimal crushing at the contact surface with ST1.0-TC0, whereas in ST1.0-TC20 there is more distinct crushing at a greater area. Compressive strength between the selected mixtures play a much greater role in this case. As previously mentioned with mid-span displacement, tire chip inclusion appears to have a more diminished effect with increasing steel fiber volume fraction, thus resulting in a greater difference in force distribution at the contact surface.

7.3.5 Effect of Steel Fiber Volume Fraction

Results from small scaled drop-hammer impact testing in Chapter 5 did show greater impact resilience with 0.75% steel volume fraction as opposed to 1.0%. This could have been the result of steel fibers overcrowding the concrete matrix at a small scale. In static testing performed in Chapter 6, increasing steel fiber volume fraction in mixtures containing tire chips appeared to increase strength capacity and reduce ductility, although very minimally. It was important to determine if the characteristics evaluated in Chapters 5 and 6 translated over to scaled impact testing.

7.3.5.1 Effect of Increasing Steel Fiber Volume Fraction on Mid-Span Deflection

A) <u>ST0.75-TC0 vs ST1.0-TC0</u>

Table 7.21 isolates steel volume fractions of 0.75% and 1.0% with no tire chip inclusion to understand the direct effects of increasing steel volume fraction. A decrease of 21.6% of final displacement was observed when steel volume fraction was increased from 0.75% to 1.0%. The fact that displacement decreased is of little surprise, however the degree of displacement reduction is interesting. The extra addition of steel fibers seemed to more effective at bridging cracks in the flexural zone as well as in the compressive. Cracks were noticeably thinner in specimens containing 1.0% steel fiber volume, which would result in decreased displacement.

Table 7.21 – Comparison of Displacement History with Increasing V_{sf} (Without Tire Chip)

	Displacement, in								Duration
Mixture Description	A	B	C	D	E	F	G	Final	Time, ms
Control (ρ=0.78%)	4.02	3.36	3.57	3.34	3.43	3.37	-	3.34	780
ST0.75-TC0 (ρ=1.17%)	2.39	1.64	1.933	1.717	1.81	1.74	-	1.71	898
ST1.0-TC0 (ρ=1.17%)	2.03	1.37	1.62	1.35	1.45	1.4	-	1.34	950

Compared to this significant change in displacement, the duration of displacement history did not seem be as affected. The time of duration increased from 898 to 950 ms by increasing steel volume fraction from 0.75% to 1.0%. At a 5.8% increase in testing duration, increasing steel fiber volume fraction does not seem to greatly increase energy dissipation capacity based on the displacement history alone.

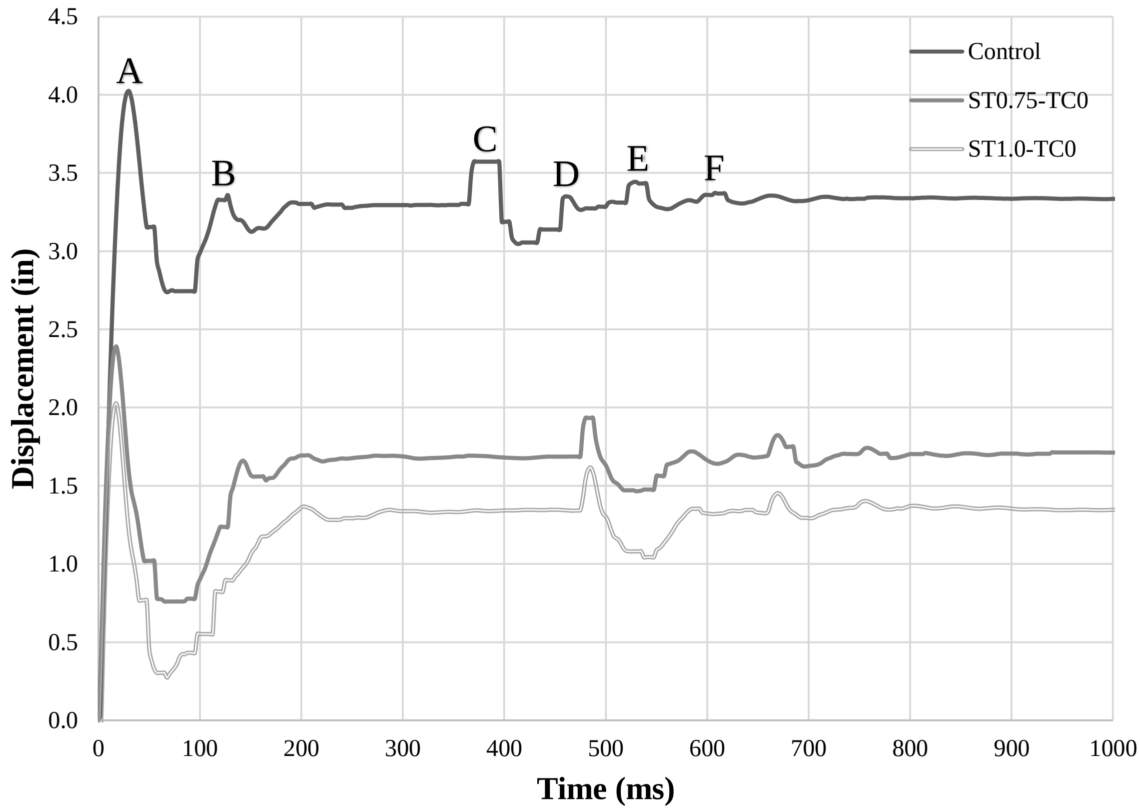

Figure 7-21. Effect of Increasing V_{sf} on Displacement History (Without Tire Chip).

The displacement histories between both mixtures, seen in Figure 7-21, follow an almost identical pattern. Increasing steel volume fraction appears to primarily decrease deflection at each point. This pattern was expected because although increasing volume of steel improves flexural strength capacity and stiffness, the typical failure behavior is practically the same. This can be visually observed from the failure modes in Section 7.2.2.

When comparing the change in relative displacement from point A to B, ST0.75-TC0 and ST1.0-TC0 experienced 31.4% (0.75 in.) and 32.5% (0.66 in.) initial displacement recovery, respectively.

Table 7.22 – Relative Change in Displacement with Increasing V_{sf} (Without Tire Chip)

	Change in Displacement Relative to Final Displacement, in						
Mixture Description	A	B	C	D	E	F	G
Control (ρ=0.78%)	0.68	0.02	0.23	0.00	0.09	0.03	-
ST0.75-TC0 (ρ=1.17%)	0.68	-0.07	0.22	0.01	0.10	0.03	-
ST1.0-TC0 (ρ=1.17%)	0.69	0.03	0.28	0.01	0.11	0.06	-

In terms of increasing the volume of steel from 0.75% to 1.0% in mixtures with no tire chip inclusion, there is little difference in behavior regarding mid-span displacement. Although the strength capacity increases, the displacement history pattern is relatively unchanged.

B) <u>ST0.75-TC20 vs ST1.0-TC20</u>

Next, the mid-span displacement response is investigated with increasing steel volume fraction in mixtures with tire chip inclusion. By increasing the volume of steel from 0.75% to 1.0%, the final mid-span displacement decreased by 14.6%. This displacement reduction is less than the 21.6% decrease from the same volumes of steel with no tire chip inclusion. This is most likely due to the inevitable reduction of concrete strength within the interfacial transition zone with tire chip inclusion. In terms of mid-span displacement, the benefits of increasing steel fiber volume fraction are less apparent in mixtures with tire chips because of their weak bonding with the cement paste resulting in increased susceptibility to cracking.

Table 7.23 – Comparison of Displacement History with Increasing V_{sf} (With Tire Chip)

	Displacement, in								Duration
Mixture Description	A	B	C	D	E	F	G	Final	Time, ms
Control (ρ=0.78%)	4.02	3.36	3.57	3.34	3.43	3.37	-	3.34	780
ST0.75-TC20 (ρ=1.17%)	2.92	2.24	2.52	2.21	2.3	2.25	2.22	2.19	985
ST1.0-TC20 (ρ=1.17%)	2.62	1.88	2.18	1.86	1.93	1.92	1.89	1.87	1020

As seen in Table 7.23, increasing the volume of steel from 0.75% to 1.0% only slightly increased testing duration from 985 to 1020 ms. Of every comparison made thus far, this 3.6% increase in displacement-time history is the least impactful.

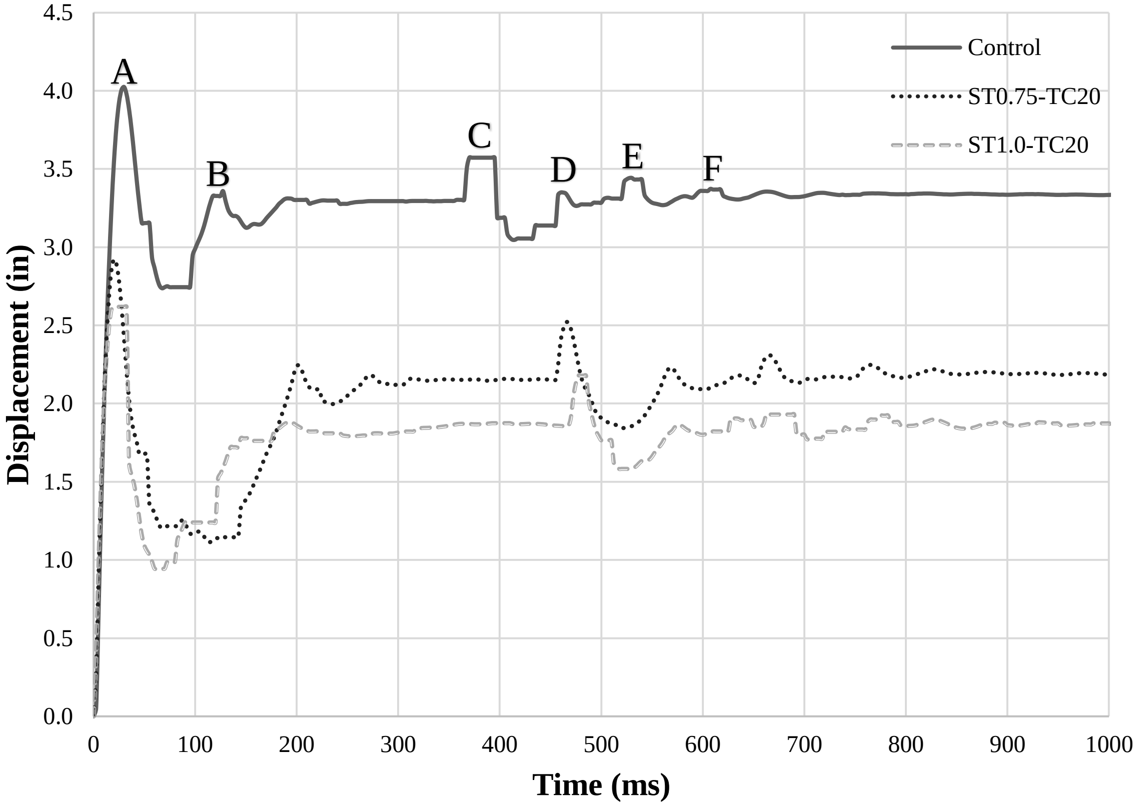

Figure 7-22. Effect of Increasing V_{sf} on Displacement History (With Tire Chip).

Although the displacement histories in Figure 7-22 differ at certain points, the patterns experienced throughout are very similar. It took ST0.75-TC20 longer to rebound and stabilize until the second impact at point C. This could signal a greater elastic response to the initial impact as a result of decreased stiffness between 0.75% and 1.0% volume of steel. Also, the second point of impact at point C arrives earlier for ST0.75-TC20 than ST1.0-TC20, suggesting a shorter rebound of the drop weight itself from the initial impact. As a result, 0.75% steel demonstrated a slight increase in energy absorption capacity.

When comparing displacement recovery from point A to B, the consistent trend of the stiffer beam exerting greater recovery was shown once again. ST0.75-TC20 and ST1.0-TC20 recovered 23.3% and 28.2%, respectively. This increase of 4.9% in recovery, is greater than the

1.1% recovery experienced with ST0.75-TC0 and ST1.0-TC0. In this regard, increasing steel volume fraction appears to have a greater effect on tire chip mixtures, whereas mid-span displacement results show otherwise. As previously mentioned, because ST0.75-TC20 took longer to rebound, more energy was absorbed which in turn reduced the amount of energy it could use to recover displacement.

From Table 7.24, although relative displacements at the point of initial and second impact are very similar, it can be seen that ST0.75-TC20 exhibited a more erratic response, which can be seen at point B and E compared to ST1.0-TC20. Again, this is because of the increase in stiffness with the 1.0% steel volume fraction allowing for the beam to stabilize much quicker.

Table 7.24 – Relative Change in Displacement with Increasing V_{sf} (With Tire Chip).

	Change in Displacement Relative to Final Displacement, in						
Mixture Description	A	B	C	D	E	F	G
Control (ρ=0.78%)	0.68	0.02	0.23	0.00	0.09	0.03	-
ST0.75-TC20 (ρ=1.17%)	0.73	0.05	0.33	0.02	0.11	0.06	0.03
ST1.0-TC20 (ρ=1.17%)	0.75	0.01	0.31	-0.01	0.06	0.05	0.02

Ultimately, the increase of steel volume fraction with tire chip inclusion had a lesser impact on final displacement and duration of displacement history compared to mixtures without tire chips. However, the effects of tire chips in conjunction with increasing the volume of steel was more prevalent with displacement recovery and resistance against deformation.

7.3.5.2 Effect of Increasing Steel Fiber Volume Fraction on Impact Forces

A) <u>ST0.75-TC0 vs ST1.0-TC0</u>

A valid conclusion could not made by directly comparing the load cell data to volume of steel. The peak impact force results are seen in Table 7.25.

Table 7.25 – Comparison of Impact Forces with Increasing V_{sf} (Without Tire Chip)

Mixture Description	Impact Force due to Load Cell, kips (KN)	Impact Force due to Accelerometer, kips (KN)	Predicted Impact Force, kips (KN)	Compressive Strength, psi (MPa)
Control (ρ=0.78%)	12.0 (53)	471 (2095)	368 (1637)	6325 (43.6)
ST0.75-TC0 (ρ=1.17%)	73.6 (327)	359 (1597)	-	7601 (52.4)
ST1.0-TC0 (ρ=1.17%)	383 (1704)	438 (1948)	384 (1708)	7329 (50.5)

The peak forces derived from accelerometer data show a much clearer relationship between the selected mixtures. The impact forces measured for ST0.75-TC0 and ST1.0-TC0 were 359 kips and 438 kips. By increasing steel volume fraction from 0.75% to 1.0%, a 22% increase of peak force was observed. Because the beam with 0.75% steel volume was more ductile than the beam with 1.0% steel volume, more energy was used for beam deformation.

When comparing the failure modes at the compressive zone between the selected mixtures, it was observed that ST0.75-TC0 experienced more crushing at the contact surface than ST1.0-TC0, despite the former possessing higher compressive strength. The crushing observed at the contact surface could be more related to higher quantity of steel fibers bridging more cracks in the compressive zone rather than the concrete strength itself.

Essentially, increasing the steel volume fraction from 0.75% to 1.0% in the selected mixtures without the presence of tire chips results in reduced ductility, but greater energy distribution without experiencing shear failure.

B) <u>ST0.75-TC20 vs ST1.0-TC20</u>

As was the case with ST0.75-TC0 and ST1.0-TC0, the load cell data cannot be directly compared for the selected mixtures. The impact force results are found in Table 7.26.

Table 7.26 – Comparison of Impact Forces with Increasing V_{sf} (With Tire Chip)

Mixture Description	Impact Force due to Load Cell, kips (KN)	Impact Force due to Accelerometer, kips (KN)	Predicted Impact Force, kips (KN)	Compressive Strength, psi (MPa)
Control (ρ=0.78%)	12.0 (53)	471 (2095)	368 (1637)	6325 (43.6)
ST0.75-TC20 (ρ=1.17%)	36.2 (161)	356 (1584)	376 (1673)	3926 (27.1)
ST1.0-TC20 (ρ=1.17%)	311 (1383)	365 (1623)	384 (1708)	4598 (31.7)

The accelerometer produced data that has been consistent with all of the mixtures observed. The peak impact forces measured for ST0.75-TC20 and ST1.0-TC20 were 356 kips and 365 kips, respectively. This 2.5% increase in peak impact force is much less significant than the 22% experienced with the 0.75% and 1.0% mixtures without tire chips. This parallels the relationship between varying steel volumes with and without tire chip inclusion and mid-span displacement. When paired with tire chips, increasing the volume of steel fibers had a lesser effect in both cases.

In the compressive zone, there was more crushing observed with ST0.75-TC20 than ST1.0-TC20. In this case, the mixture with 1.0% steel fiber volume had greater compressive strength, but as previously stated, the increase of steel fiber volume had a greater effect on mitigating crushing at the contact surface.

Similar to the 0.75% and 1.0% mixtures with no tire chip inclusion, these selected mixtures showed that increasing steel fiber volume reduces ductility but increases resistance to crushing and flexural failure. However, these properties are more prevalent in mixtures without tire chips.

Table 7.27 – Summary of Mid-Span Displacement Analysis

	Increase of Final Displacement, (%)	**Increase of Testing Time Duration, (%)**	**Increase of Initial Displacement Recovery, (%)**
Effect of Tire Chip Inclusion	4.5	28	0.3
Effect of Tire Chip in FRC (V_{sf} = 0.75%)	28	9.8	-8.4
Effect of Tire Chip in FRC (V_{sf} = 1.0%)	40	7.4	-5
Effect of Increasing V_f of Steel Fiber (A)*	21.6	5.8	1.1
Effect of Increasing V_f of Steel Fiber (B)*	14.6	3.6	4.9

*(A) refers to mixtures without tire chips and (B) refers to mixtures with tire chip inclusion

7.3.6 Summary of Impact Results

In summary, both tire chip and steel fiber inclusion produced an increase in energy dissipation capacity of the RC beams subjected to impact forces. Specifically, the primary effects the tire chips were increasing displacement and increasing the duration of testing time. These effects were the consequence of reduced stiffness of the RC beams from tire chip inclusion. On the other hand, the result of steel fiber inclusion was greater energy transfer to the supports and reduced crack width. Steel fiber inclusion, especially at 1.0% volume fraction, was crucial in achieving a global failure response. For this reason, it was determined that the optimal mixture designs under impact loading contained 1.0% steel fiber volume fraction with and without tire chips. However, although tire chip inclusion increased displacement, for the purpose of this study, it was ultimately determined that for this mixture design a 1.0% steel fiber volume fraction without tire chip inclusion was desired due to exhibiting a greater global failure response and thus engaging a greater area of the target member.

8. CONCLUSIONS AND RECOMMENDATIONS

This study investigated the performance of recycled tire chip aggregates in conjunction with fiber reinforcement in standard Portland cement concrete for the purpose of optimizing impact resilience. Based on the results from Part I, II, and III, the following conclusions were drawn:

8.1 Part I – Mixture Optimization

- At a 20% replacement of coarse aggregate by volume, tire chips significantly reduced mechanical properties such as compressive and flexural strength due to reduction in stiffness and greater susceptibility to failure in the cement interfacial transition zone from poor bonding relative to natural coarse aggregates.
- In rubberized mixtures containing fiber reinforcement, steel fibers proved to be the most effective in terms reversing the adverse effects tire chips have on mechanical properties as well as maintaining workability.
- PVA fibers at a 40/60 split with steel and PP fibers significantly reduced workability in rubberized concrete, which resulted in decreased mechanical properties and impact performance.
- Increasing steel fiber volume fraction in rubberized mixtures improves flexural strength, although it has inconsequential effects on compressive strength
- Drop-hammer impact resilience decreases as a result of overcrowding within the concrete matrix at a small scale. As a result, 0.75% steel volume fraction exhibited great impact resilience than 1.0%.

8.2 Part II – Scaled Static Test Results

The following conclusions are made from the static beam tests presented in Chapter 6.3:

- Rubberized mixtures without fiber reinforcement showed an increase in ductility compared to the control, however, were more susceptible to crushing failure at the contact surface.
- Steel fiber inclusion at 0.5%, 0.75%, and 1.0% volume fraction improved the flexural capacity of the FRC beams and decreased deflection compared to the control.
- Increasing steel fiber volume fraction did not appear to produce any noticeable benefit to improving energy dissipating capacity when the areas under the static load-deflection curves are compared.
- Because FRC beams improve flexural and shear capacity, it is desirable to increase the flexural steel reinforcement ratio by 50% to maximize the energy dissipation potential of the fiber reinforcement, ultimately increasing toughness.

8.3 Part III – Scaled Impact Test Results

The following conclusions are drawn from the drop-weight impact tests described in Chapter 7.3:

- In conventional RC beams without fiber reinforcement or tire chip inclusion, impact forces are dissipated through a local failure resulting in what is widely known as scabbing (ejection of target material on distal side), as well as spalling at the target contact surface. Therefore, the kinetic energy is dissipated through fractures of the beam on a local area rather than beam deformation.
- Steel fiber and tire chip inclusion significantly reduces impact forces as a result of increased ductility and more effective energy distribution at initial impact.

- Increasing steel fiber volume fraction from 0.75% to 1.0% slightly reduces deflection; however, it increases resistance to compressive, flexural, and shear failure to ultimately achieve an overall target response (global failure).
- Testing scale influences the effectiveness of increasing steel fiber volume fraction subjected to impact loads. From Part-I, it was shown that 0.75% steel volume produced significantly higher results from the drop-hammer impact test than 1.0%. However, at the larger scale in Part-III, the 1.0% steel volume proved superior in terms of impact resilience and failure response.
- The duration of the displacement-time history in conventional RC beams is increased through the inclusion of tire chips and steel fibers. Greater target rebounding effects are observed due to increased displacement recovery.
- The effectiveness of tire chip inclusion decreased with increasing steel fiber volume fraction. It was observed that more energy was dissipated through the steel fiber reinforced concrete mixture than with the tire chips at higher volumes of steel. This is attributed to increased compressive strength resulting in shear/flexural capacity increases.

8.4 Recommendations

It is recommended that the design of concrete mixtures and reinforcing details for a reinforced concrete structure should be accomplished to achieve a desired level of impact performance. In this study, the overall response of beams, dissipating the kinetic energy of a projectile by engaging the full span of its target structure, was desirable despite of reduced mid-span deflection. More specific recommendations pertinent to a future study investigating crash-worthiness of traffic safety barriers are listed below:

- Rubber particle and fiber inclusion in concrete mixtures shall be proportioned using the absolute volume method. Rubber tire chips shall be included as a volume fraction replacement of coarse aggregate, whereas fiber inclusion shall be taken as a volume fraction of the total pre-fiber batch volume.
- Fiber reinforcement should be included with rubberized mixtures subjected to strong impact forces. Although rubber particles have the ability to increase the energy dissipation capacity of concrete on their own, mechanical properties are negatively impacted, and fiber reinforcement aids in preventing failure by reducing crack propagation and crushing.
- Rubber tire chips should undergo either mechanical or chemical surface treatments prior to mixing, in order to improve the bond with the cement paste.
- Chemical admixtures should be used in rubberized concrete mixtures, especially with fiber inclusion. A properly dosed superplasticizer is very useful in improving workability, whereas a viscosity modifying agent is essential in suspending rubber particles within the concrete matrix and preventing rubber particles from floating to the top surface.
- Increasing the steel reinforcement ratio should be considered as an effective method of increasing concrete toughness, possibly without significantly increasing cost.
- Finally, it is strongly recommended that a desired failure mode and performance criteria for an impacting object (e.g., a vehicle) and its target (e.g., concrete barrier) be established to improve the design of cementitious composites and flexural/shear reinforcement details and thus meet the performance needs.

9. FUTURE WORK

Further investigation of multi-scale fiber reinforcement may be considered. Based on the mixture design used in this study, micro-scale fibers such as PVA significantly reduced workability. Due to the proven benefits of multi-scaled fiber reinforcement, it is desired to develop a mixture that optimizes the volume fraction of PVA fibers to preserve workability. Furthermore, based on the results from static beam testing, it was observed that increasing the reinforcement ratio significantly increased energy dissipation capacity. To decrease total cost, specimens of reduced sections utilizing this increased reinforcement ratio should be observed and optimized. Moreover, to improve the sustainability of rubberized mixtures designs, steel fibers extracted from tire belts can be utilized. The performance of these tire-derived steel fibers should be compared with steel fibers used in the industry to investigate potential cost and environmental benefits.

10. REFERENCES

Abrate, S., Impact on Composite Structures, Cambridge University Press, 1998, 301 pp.

ACI Committee 544. (2017). *Report on the Measurement of Fresh State Properties and Fiber Dispersion of Fiber-Reinforced Concrete* (ACI 544.2R-17). Retrieved from http://concrete.org

Aiello, M.A. & Leuzzi, F. (2010). Waste tyre rubberized concrete: Properties at fresh and hardened state. Waste Management, 1696-1704.

Afroughsabet V., Ozbakkaloglu T., (2015). Mechanical and durability properties of high-strength concrete containing steel and polypropylene fibers. Construction and Building Materials, 73-82

Ahmed, Shaikh Faiz Uddin, Mohamed Maalej, and P. Paramasivam. "Flexural responses of hybrid steel–polyethylene fiber reinforced cement composites containing high volume fly ash." Construction and Building Materials 21.5 (2007): 1088-1097.

Alhozaimy, A. M., P. Soroushian, and F. Mirza. "Mechanical properties of polypropylene fiber reinforced concrete and the effects of pozzolanic materials." Cement and Concrete Composites 18.2 (1996): 85-92.

Ali, N.A., Amos, A.D., Roberts, M., 1993. Use of ground rubber tires in portland cement concrete. In: Dhir, R.K. (Ed.), Proceedings of the International Conference on Concrete 2000, University of Dundee, Scotland, UK, pp. 379–390.

ASTM Standard C33, 2016e1, "Specification for Concrete Aggregates," ASTM International, West Conshohocken, PA, 2016, DOI: 10.1520/C0033_C0033M-16E01, www.astm.org.

ASTM Standard C39, 2017b, "Test Method for Compressive Strength of Cylindrical Concrete Specimens," ASTM International, West Conshohocken, PA, 2017, DOI: 10.1520/C0039_C0039M-17B, www.astm.org.

ASTM Standard C78, 2016, "Test Method for Flexural Strength of Concrete (Using Simple Beam with Three-Point Loading," ASTM International, West Conshohocken, PA, 2016, DOI: 10.1520/C0078_C0078M-16, www.astm.org.

ASTM Standard C136, 2014, "Test Method for Sieve Analysis of Fine and Coarse Aggregates," ASTM International, West Conshohocken, PA, 2015, DOI: 10.1520/C0136_C0136M-14, www.astm.org.

ASTM Standard C138, 2017a, "Test Method for Density (Unit Weight), Yield, and Air Content (Gravimetric) of Concrete," ASTM International, West Conshohocken, PA, 2017, DOI: 10.1520/C0138_C0138M-17A, www.astm.org.

ASTM Standard C143, 2015a, "Test Method for Slump of Hydraulic-Cement Concrete," ASTM International, West Conshohocken, PA, 2016, DOI: 10.1520/C0143_C0143M-15A, www.astm.org.

ASTM Standard C150, 2018, "Standard Specification for Portland Cement," ASTM International, West Conshohocken, PA, 2016, DOI: 10.1520/C0150_C0150M-18, www.astm.org.

ASTM Standard C192, 2016a, "Practice for Making and Curing Concrete Test Specimens in the Laboratory," ASTM International, West Conshohocken, PA, 2016, DOI: 10.1520/C0192_C0192M-16A, www.astm.org.

ASTM Standard C231, 2017a, "Test Method for Air Content of Freshly Mixed Concrete by the Pressure Method," ASTM International, West Conshohocken, PA, 2017, DOI: 10.1520/C0231_C0231M-17A, www.astm.org.

ASTM Standard C470, 2015, "Standard Specification for Molds for Forming Concrete Test Cylinders Vertically," ASTM International, West Conshohocken, PA, 2015, DOI: 10.1520/C0470_C0470M-15, www.astm.org.

ASTM Standard C494, 2017, "Specification for Chemical Admixtures for Concrete," ASTM International, West Conshohocken, PA, 2017, DOI: 10.1520/C0494_C00494M-17, www.astm.org.

ASTM Standard C511, 2013, "Specification for Mixing Rooms, Moist Cabinets, Moist Rooms, and Water Storage Tanks Used in the Testing of Hydraulic Cements and Concretes," ASTM International, West Conshohocken, PA, 2014, DOI: 10.1520/C0511-13, www.astm.org.

ASTM Standard C566, 2013, "Test Method for Total Evaporable Moisture Content of Aggregate by Drying," ASTM International, West Conshohocken, PA, 2013, DOI: 10.1520/C0566-13, www.astm.org.

ASTM Standard C1064, 2017, "Test Method for Temperature of Freshly Mixed Hydraulic-Cement Concrete," ASTM International, West Conshohocken, PA, 2017, DOI: 10.1520/C1064_C1064M-17, www.astm.org.

ASTM Standard D6270, 2008 (2012), "Practice for Use of Scrap Tires in Civil Engineering Applications," ASTM International, West Conshohocken, PA, 2012, DOI: 10.1520/D6270-08R12, www.astm.org.

Benazzouk, A., Queneudec, M., 2002. Durability of cement–rubber composites under freeze thaw cycles. In: Dhir, R.K. et al. (Ed.), Proceedings of the International Conference on Sustainable Concrete Construction, University of Dundee, Scotland, UK, pp. 356– 362.

Biel, T.D., Lee, H., 1996. Magnesium oxychloride cement concrete with recycled tire rubber. Transportation Research Record No. 1561, Transportation Research Board, Washington, DC, pp. 6–12.

Chorzepa, M. G., et al. (2017). "Impact Test: Multi-Scale Fiber-Reinforced Concrete Including Polypropylene and Steel Fibers." ACI Structural Journal 114(6).

Eldin, N.N., Senouci, A.B., 1993. Rubber-tire particles as concrete aggregates. Journal of Materials in Civil Engineering 5, 478–496.

Fattuhi, N.I., Clark, N.A., 1996. Cement-based materials containing tire rubber. Journal of Construction and Building Materials 10 (4), 229–236.

Fedroff, D., Ahmad, S., Savas, B.Z., 1996. Mechanical properties of concrete with ground waste tire rubber. Transportation Research Board, Report No. 1532, Transportation Research Board, Washington, DC, pp. 66–72.

Fujikake, K., Li, B., and Soeun, S. (2009). ”Impact Response of Reinforced Concrete Beam and Its Analytical Evaluation.” J. Struct. Eng., 135(8), 938–950.

Ganjian, E., et al. (2009). "Scrap-tyre-rubber replacement for aggregate and filler in concrete." Construction and Building Materials 23(5): 1828-1836.

Gesoğlu, M., et al. (2014). "Investigating properties of pervious concretes containing waste tire rubbers." Construction and Building Materials 63: 206-213.

Goulias, D.G., Ali, A.H., 1997. Non-destructive evaluation of rubber modified concrete. In: Proceedings of a Special Conference, ASCE, New York, pp. 111–120.

Güneyisi, E., et al. (2004). "Properties of rubberized concretes containing silica fume." Cement and Concrete Research 34(12): 2309-2317.

Guo Y., Zhang J., Chen G., Chen G, Xie Z., (2014) Fracture behaviors of a new steel fiber reinforced recycled aggregate concrete with crumb rubber, Constr. Build. Mater. 53 32–39.

Holmes N, Browne A, Montague C. Acoustic properties of concrete panels with crumb rubber as a fine aggregate replacement. Construction Building Materials 2014;73:195–204.

Ismail, M.K., Hassan, A.A. (2016) Performance of full-scale self-consolidating rubberized concrete beams in flexure, ACI Mater. J. 113 (1) 1–6.

Kardos, A., & Durham, S. (2015). Strength, durability, and environmental properties of concrete utilizing recycled tire particles for pavement applications. Construction and Building Materials, 832-845.

Khatib, Z., & Bayomy, F. (1999). Rubberized Portland Cement Concrete. ASCE Journal of Materials in Civil Engineering, 206-213

Khosla, N.P., Trogdon, J.T., 1990. Use of ground rubber in asphalt paving mixtures. Technical Report, Department of Civil Engineering, North Carolina State University, Raleigh.

Li Q.M., Reid S.R, Wen H.M., Telford A.R. (2005) Local impact effects of hard missiles on concrete targets, International Journal of Impact Engineering, 32 224–284.

Masud, M. (2015). Multi-scale impact resilient smart composites (MIRACs) for hazard mitigation. [electronic resource], 2015.

Naik, T.R, Singh, S.S., 1991. Utilization of discarded tires as construction materials for transportation facilities. Report No. CBU-1991-02, UWM Center for By-products Utilization. University of Wisconsin-Milwaukee, Milwaukee, 16 pp.

Noaman A. T., Bakar B.H. A., Akil H. Md., Alani A.H. (2017). Fracture characteristics of plain and steel fibre reinforced rubberized concrete. Construction and Building Materials, 414-423

Pacheco-Torgal F, Ding Yining, Jalali Said. Properties and durability of concrete containing polymeric wastes (tire rubber and polyethylene terephthalate bottles): an overview. Construction Building Materials 2012;30:714–24.

Pelisser, F., et al. (2011). "Concrete made with recycled tire rubber: Effect of alkaline activation and silica fume addition." Journal of Cleaner Production 19(6-7): 757-763.

Raghvan, D., Huynh, H., Ferraris, C.F., 1998. Workability, mechanical properties and chemical stability of a recycled rubber-filled cementitious composite. Journal of Materials Science 33 (7), 1745-1752.

Reda Taha, M., et al. (2008). Mechanical, Fracture, and Microstructural Investigations of Rubber Concrete.

Rostami, H., Lepore, J., Silverstraim, T., Zundi, I., 1993. Use of recycled rubber tires in concrete. In: Dhir, R.K. (Ed.), Proceedings of the International Conference on Concrete 2000, University of Dundee, Scotland, UK, pp. 391–399.

Saatci S., Vecchio J.V, (2009) “Effect of Shear Mechanisms on Impact Behavior of Reinforced Concrete Beams” ACI Structural Journal, 106 (1)), pp. 78–86

Şahin, Y. and F. Köksal (2011). "The influences of matrix and steel fibre tensile strengths on the fracture energy of high-strength concrete." Construction and Building Materials 25(4): 1801-1806.

Segre, N., & Joekes, I. (2000). Use of tire rubber particles as addition to cement paste. Cement and Concrete Research, 30, 1421-1425

Siddique, R., & Naik, T. R. (2004). Properties of concrete containing scrap-tire rubber – an overview. Waste Management, 563–569.

Stallings, K. A. and S. Durham (2017). Investigation of recycled tire chips for use in GDOT concrete used to construct barrier walls and other applications, Athens, Georgia : University of Georgia, 2017.

Su, H., et al. (2015). "Properties of concrete prepared with waste tyre rubber particles of uniform and varying sizes." Journal of Cleaner Production 91: 288-296.

Sukontasukkul, P. and K. Tiamlom (2012). "Expansion under water and drying shrinkage of rubberized concrete mixed with crumb rubber with different size." Construction and Building Materials 29: 520-526.

Tang, Taiping, and Hamid Saadatmanesh. "Analytical and experimental studies of fiber-reinforced polymer-strengthened concrete beams under impact loading." ACI structural journal 102.1 (2005).

Tantala, M.W., Lepore, J.A., Zandi, I., 1996. Quasi-elastic behavior of rubber included concrete. In: Ronald Mersky (Ed.), Proceedings of the 12th International Conference on Solid Waste Technology and Management, Philadelphia, PA.

Thomas, B. S., Gupta, R.C. (2015). A comprehensive review on the applications of waste tire rubber in cement concrete. Renewable and Sustainable Energy Reviews, 1323-1333.

Topçu, I.B., 1995. The properties of rubberized concrete. Cement and Concrete Research 25, 304–310.

Topcu, I.B., Avcular, N., 1997. Analysis of rubberized concrete as a composite material. Cement and Concrete Research 27 (8), 1135– 1139.

Toutanji, H.A., 1996. The use of rubber tire particles in concrete to replace mineral aggregates. Cement and Concrete Composites 18, 135–139.

Treacy, M. J.; Ebbesen, T. W.; and Gibson, J. M., “Exceptionally High Young’s Modulus Observed for Individual Carbon Nanotubes,” *Nature*, V. 381, 1996, pp. 678-680.

Yang, En-Hua, and Victor C. Li. "Tailoring engineered cementitious composites for impact resistance." Cement and Concrete Research 42.8 (2012): 1066-1071.

Zheng, L., Huo, X. S., and Yuan, Y. (2008). “Strength, modulus of elasticity, and brittleness index of rubberized concrete” Journal of Materials in Civil Engineering, 692-699

APPENDICIES

A.1 Mixture Designs with Total Batch Quantities

A.1.1 Design Matrix for Part I Mixtures

Mixture Description	w/c	*Cement	*Coarse Aggregate	*Fine Aggregate	*Tire Chips	*Steel Fiber	*PP Fiber	*PVA Fiber	**HRWRA	**VMA	**AEA
Control	0.42	611 (362)	1800 (816)	952 (432)	0	0	0	0	7 (456)	8 (522)	1.3 (81)
ST0.0-PV0.0-TC20	0.42	611 (362)	1440 (653)	952 (432)	152 (69)	0	0	0	8 (522)	8 (522)	1.3 (81)
ST1.0-PV0.0-TC0	0.42	611 (362)	1800 (816)	952 (432)	0	132 (78)	0	0	7 (456)	8 (522)	1.3 (81)
PP1.0-PV0.0-TC0	0.42	611 (362)	1800 (816)	952 (432)	0	0	16 (10)	0	15 (985)	8 (522)	1.3 (81)
ST0.5-PV0.5-TC0	0.42	611 (362)	1800 (816)	952 (432)	0	66 (39)	0	11(7)	9 (591)	8 (522)	1.3 (81)
PP0.6-PV0.4-TC0	0.42	611 (362)	1800 (816)	952 (432)	0	0	10 (6)	9 (5)	10 (657)	8 (522)	1.3 (81)
ST1.0-PV0.0-TC20	0.42	611(362)	1440 (653)	952 (432)	152 (69)	132 (78)	0	0	10 (657)	8 (522)	1.3 (81)
PP1.0-PV0.0-TC20	0.42	611 (362)	1440 (653)	952 (432)	152 (69)	0	16 (10)	0	10 (657)	8 (522)	1.3 (81)
ST0.6-PV0.4-TC20	0.42	611 (362)	1440 (653)	952 (432)	152 (69)	79 (47)	0	9 (5)	13 (854)	8 (522)	1.3 (81)
PP0.6-PV0.4-TC20	0.42	611 (362)	1440 (653)	952 (432)	152 (69)	0	10 (6)	9 (5)	15 (985)	8 (522)	1.3 (81)
ST0.5-PV0.0-TC20	0.42	611 (362)	1440 (653)	952 (432)	152 (69)	66 (39)	0	0	7 (456)	8 (522)	1.3 (81)
ST0.75-PV0.0-TC20	0.42	611 (362)	1440 (653)	952 (432)	152 (69)	99 (59)	0	0	8 (522)	8 (522)	1.3 (81)

*** lb/yd³ (kg/m³)**
**** fl. oz/cwt (mL/100kg)**

A.1.2 Design Matrix for Part II Mixtures

Mixture Description	w/c	*Cement	*Coarse Aggregate	*Fine Aggregate	*Tire Chips	*Steel Fiber	**HRWRA	**VMA	**AEA
Control (ρ=0.78%)	0.42	611 (362)	1800 (816)	952 (432)	0	0	5 (326)	5 (326)	1.3 (81)
ST0.0-TC20 (ρ=0.78%)	0.42	611 (362)	1440 (653)	952 (432)	152 (69)	0	5 (326)	5 (326)	1.3 (81)
ST0.75-TC20 (ρ=0.196%)	0.42	611 (362)	1440 (653)	952 (432)	152 (69)	99 (59)	5 (326)	6 (326)	1.3 (81)
ST1.0-TC20 (ρ=0.78%)	0.42	611 (362)	1440 (653)	952 (432)	152 (69)	132 (78)	5 (326)	5 (326)	1.3 (81)
ST0.5-TC20 (ρ=0.78%)	0.42	611 (362)	1440 (653)	952 (432)	152 (69)	66 (39)	5 (326)	6 (326)	1.3 (81)
ST0.75-TC20 (ρ=0.78%)	0.42	611 (362)	1440 (653)	952 (432)	152 (69)	99 (59)	5 (326)	6 (326)	1.3 (81)
ST0.75-TC20 (ρ=1.17%)	0.42	611 (362)	1440 (653)	952 (432)	152 (69)	99 (59)	5 (326)	6 (326)	1.3 (81)
ST1.0-TC20 (ρ=1.17%)	0.42	611 (362)	1440 (653)	952 (432)	152 (69)	132 (78)	5 (326)	6 (326)	1.3 (81)

*** lb/yd³ (kg/m³)**
**** fl. oz/cwt (mL/100kg)**

A.1.3 Design Matrix for Part III Mixtures

Mixture Description	w/c	*Cement	*Coarse Aggregate	*Fine Aggregate	*Tire Chips	*Steel Fiber	**HRWRA	**VMA	**AEA
Control (ρ=0.78%)	0.42	611 (362)	1800 (816)	952 (432)	0	0	5 (326)	5 (326)	1.3 (81)
ST0.0-TC20 (ρ=0.78%)	0.42	611 (362)	1440 (653)	952 (432)	152 (69)	0	5 (326)	5 (326)	1.3 (81)
ST0.75-TC0 (ρ=1.17%)	0.42	611 (362)	1800 (816)	952 (432)	0	99 (59)	5 (326)	5 (326)	1.3 (81)
ST0.75-TC20 (ρ=1.17%)	0.42	611 (362)	1440 (653)	952 (432)	152 (69)	99 (59)	5 (326)	5 (326)	1.3 (81)
ST1.0-TC0 (ρ=1.17%)	0.42	611 (362)	1800 (816)	952 (432)	0	132 (78)	5 (326)	6 (326)	1.3 (81)
ST1.0-TC20 (ρ=1.17%)	0.42	611 (362)	1440 (653)	952 (432)	152 (69)	132 (78)	5 (326)	6 (326)	1.3 (81)

*** lb/yd³ (kg/m³)**
**** fl. oz/cwt (mL/100kg)**

A.2 Displacement-Time Histories of Part III Mixtures

A.2.1 Control

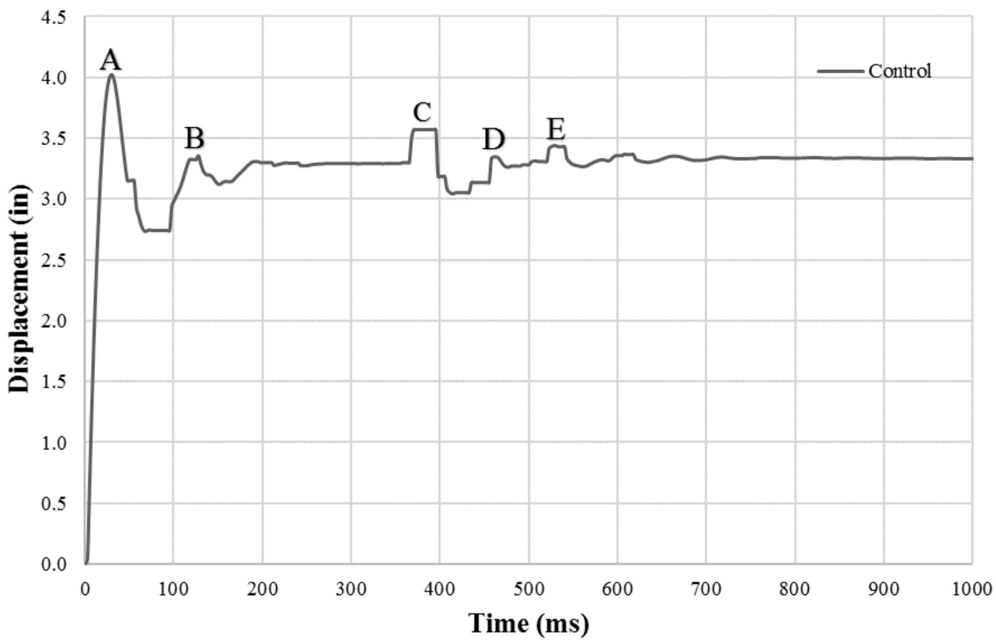

A.2.2 ST0.0-TC20

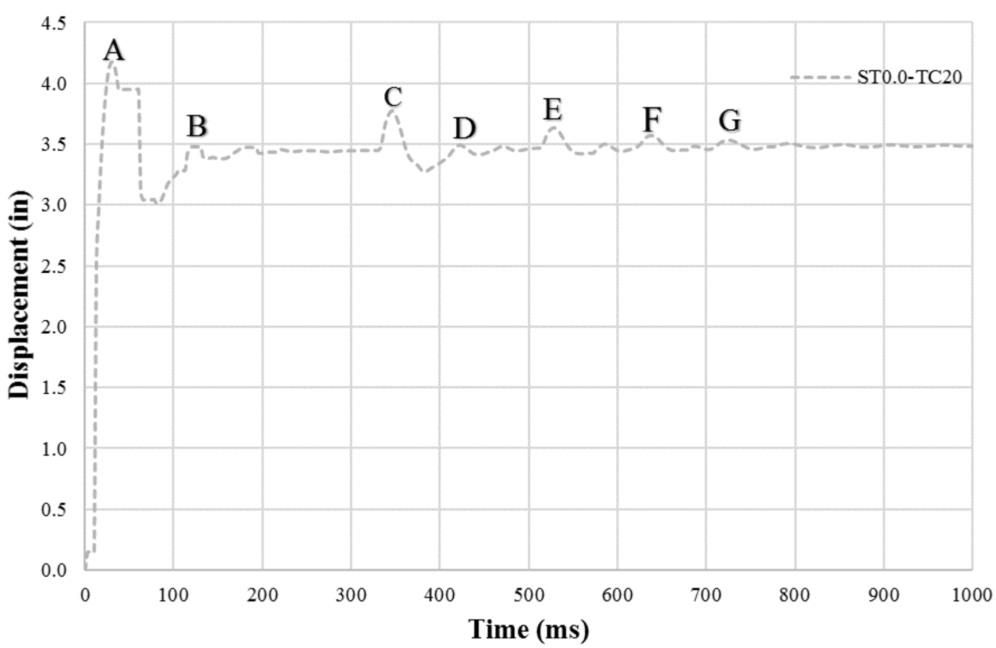

A.2.3 ST0.75-TC0

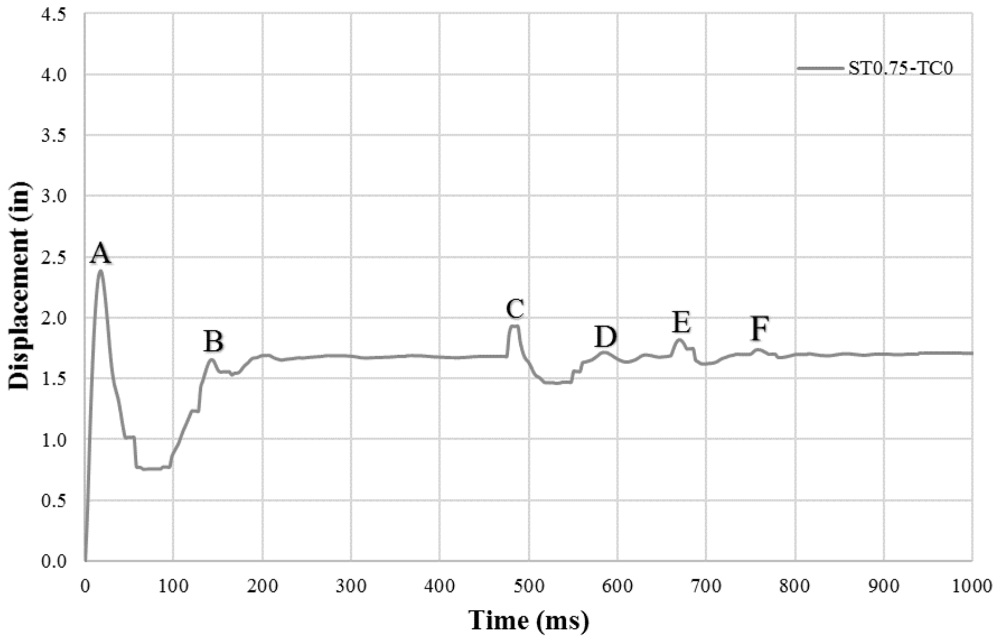

A.2.4 ST0.75-TC20

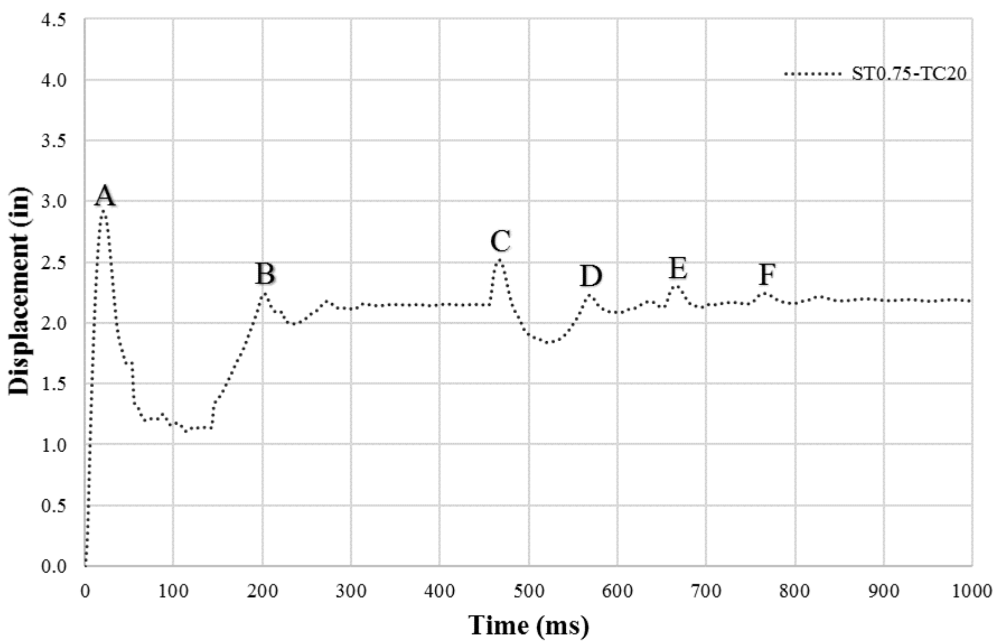

A.2.5 ST1.0-TC0

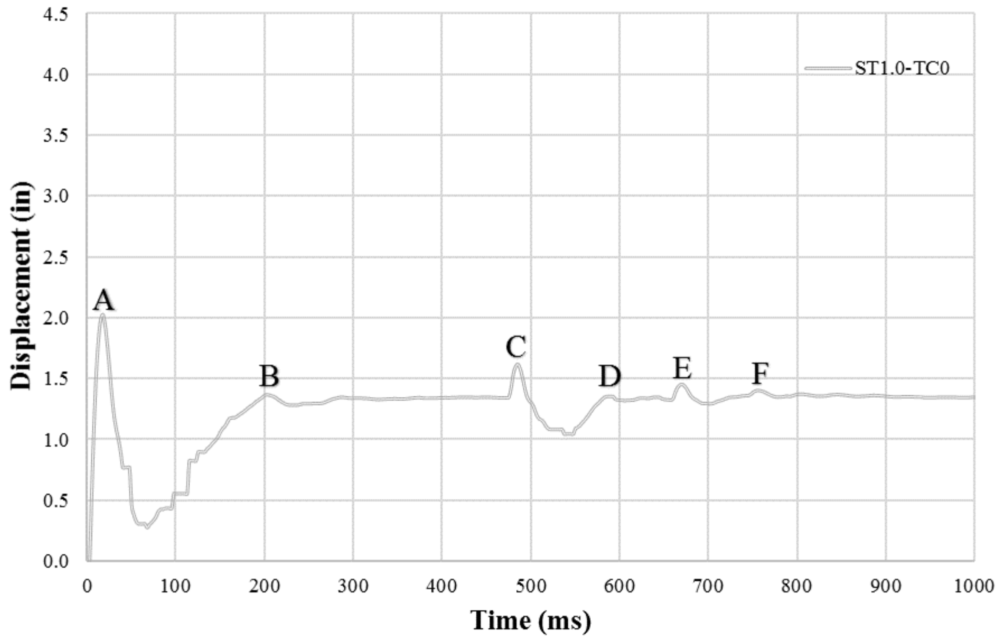

A.2.6 ST1.0-TC20

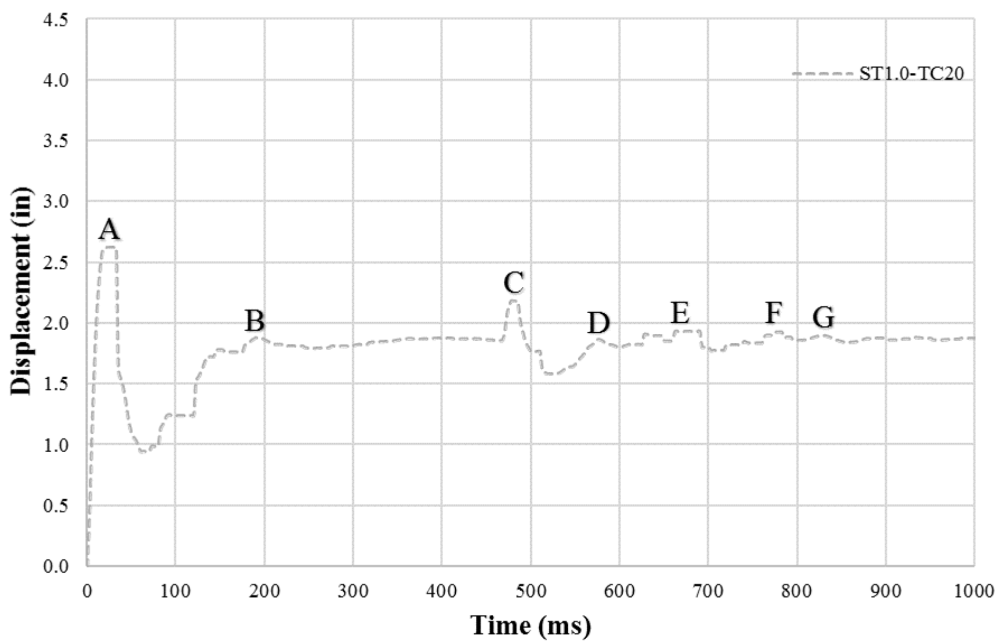

A.3 Predictive Impact Force and Displacement Sample Calculations

A.3.1 Calculating Predicted Impact Force

Derived from a spring-mass model (Tang et al. 2005), the predicted impact force can be calculated using the following equation,

$$F = K_{bs}y = V(K_{bs}m_1)^{\frac{1}{2}}sin\omega t \tag{6}$$

Taking into account reduced stiffness, Eq. (7) is modified as,

$$F = K_{bs}y = \frac{V(K_{bs}m_1)^{\frac{1}{2}}}{\gamma}sin\omega t \tag{7}$$

Inputs:

Velocity of the drop-weight, V = 10.96 m/s (35.89 ft/s)

Mass of drop-weight, m_1 = 181.4 kg (12.43 lb-m)

Linear Stiffness, K_{bs} = 6,682,644 N/m (38,159 lb/in)

Measured impact force from accelerometer data (Control beam), F = 2,095,112 N (471,000 lb)

Calculate average γ = 0.23

Calculation:

$\omega = \sqrt{\frac{K_{bs}}{m_1}} = \sqrt{\frac{6,682,644}{181.4}} = 191.9$

From Eq. (7), $F = K_{bs}y = \frac{10.96(6,682,664 \times 181.4)^{\frac{1}{2}}}{0.23}$ = 1,636,945 N (368,000 lb)

A.3.2 Calculating Predicted Displacement

Derived from flexural wave theory (Tang et al. 2005), the predicted displacement is calculated by the following equation,

$$y(x,t) = \frac{2P}{\rho A l} \sum_{n=1,3,5}^{\infty} \frac{(-1)^{\frac{n-1}{2}} sin\beta_n x_o sin\omega_n t}{\omega_n} \tag{11}$$

Inputs:

Area of beam, A = 73 in.

Span of beam, l = 60 in²

Density of beam, ρ = 0.083 lb/in³

Calculated force (Eq. (7)), P = 368,000 lb

Bending stiffness, EI = 2266601 lb-in²

n = 1,3,5,7,9

$\beta_n = \frac{n\pi}{l}$

$\beta_n x_o = \frac{n\pi}{2}$

$a = \frac{EI}{A\rho}$

$\omega_n = a{\beta_n}^2$

Calculation:

$a = \frac{EI}{A\rho}$ = 455218

n	β_n	$\beta_n x_o$	$sin\beta_n x_o$	ω_n	δ_i, in. (Eq. (11))
1	0.043036	1.570795	1	843.0883	2.401739
3	0.129107	4.712385	-1	7587.795	0.26686
5	0.215178	7.853975	1	21077.21	0.09607
7	0.301249	10.99557	-1	41311.33	0.049015
9	0.38732	14.13716	1	68290.15	0.029651

Total calculated, $\boldsymbol{\delta_c} = \sum \boldsymbol{\delta_i}$ = 2.84 in.

Measured deflection, $\boldsymbol{\delta}$ **=** 3.34 in.